KANSAS GEOLOGICAL SURVEY
OPEN-FILE REPORT 88-10

SHALLOW STRUCTURE IN SOUTHEAST KANSAS USING SHORT-PERIOD SURFACE-WAVE DISPERSION

by

Greg Hildebrand

Disclaimer

The Kansas Geological Survey does not guarantee this document to be free from errors or inaccuracies and disclaims any responsibility or liability for interpretations based on data used in the production of this document or decisions based thereon. This report is intended to make results of research available at the earliest possible date, but is not intended to constitute final or formal publications.

Kansas Geological Survey
1930 Constant Avenue
University of Kansas
Lawrence, KS 66047-3726

SHALLOW STRUCTURE IN SOUTHEAST KANSAS USING SHORT-PERIOD SURFACE-WAVE DISPERSION

by

Greg Hildebrand
B.A., San Francisco State University, 1984

Submitted to the Department of Geology and the faculty of the Graduate School of the University of Kansas in partial fulfillment of the requirements for the degree of Master of Science.

Professor in charge

Committee Members

For the Department

July 5, 1988
Date Thesis Accepted

ABSTRACT

During the operation of a temporary, thirteen station, three-component seismic array in southeast Kansas, mining explosions from five different azimuths around the array were recorded. Each of these recorded events exhibited a dispersed, short-period, fundamental-mode, Rayleigh-wave phase (Rg) and a dispersed, short-period, fundamental-mode, Love-wave phase. The recorded Rg phases lie in the period range of 0.6 to 3.1 seconds and the recorded Love-wave phases lie in the period range of 0.5 to 3.2 seconds.

The group-velocity dispersion of both phases was measured from the digital records of each of the events recorded at the center station of the array. The measured group-velocity dispersion curves were then jointly inverted for the shear-wave velocity structure of the shallow crust (roughly the upper 1 km) between the sources and the array.

Inversion of the group-velocity dispersion data reveals that the observed dispersion can be explained by a two-layer over a half-space velocity model. Layer 1 has an average shear-wave velocity of 1.9 km/s. this layer corresponds to Pennsylvanian rocks in the region. Layer 2 has a shear-wave velocity of 2.7 km/s and

corresponds to the Mississippian and Cambro-Ordovician carbonate rocks of the region. The half-space has a shear-wave velocity of 3.5 km/s and corresponds to the Precambrian basement complex. Differences in the observed dispersion along each of the paths appears to be due to differences in the thicknesses of the two layers that comprise the model.

AKNOWLEDGEMENTS

I would like to thank my committee members Ralph Knapp, Don Sprowl, and Pat Bickford for their advise and critical review of my thesis. I am especially grateful for the support and advise of Dave Harris of Lawrence Livermore National Laboratory. Dave provided me with access to the data, an office, a computer terminal, and the use of his brilliantly conceived seismic array processing program (XAP). Thanks also to Howard Patton, Phil Harbin, Don Rock, and George Randall of Lawrence Livermore Laboratory for their help during the research and preparation of this thesis. Special thanks to Don Steeples and Rick Miller for their support during my years at the KGS. Most important, thanks to my wife Corrie, for her support, love and understanding.

TABLE OF CONTENTS

LIST OF ILLUSTRATIONS

LIST OF TABLES

Table Page

INTRODUCTION

Contrasts in the physical properties of various layers of the earth affect the propagational velocities of seismic surface-waves. Observation of variations in surface-wave velocity as a function of wavelength are used to investigate the structure of the earth at various scales. The variation in velocity as a function of wavelength is known as dispersion. Generally, the longer the wavelengths being investigated, the greater is the depth in the earth from which inferences about velocity structure can be drawn. Dispersion of free oscillations of the earth (normal modes of vibration of the entire earth, generated by very large earthquakes) have been used to investigate properties of the earth's outer core (Oliver, 1962). Surface-waves generated by large earthquakes have been used to determine the structure of the total crust (Ewing and Press, 1959) and Rayleigh waves generated by small explosions have been used to investigate the structure of the upper 100 feet of the crust (Dobrin et al., 1951). Records of dispersed surface-waves permit conclusions about the average velocity structure along the path between a seismic energy source and a receiver.

Because there is usually a strong contrast in the physical properties between sedimentary rocks and underlying crystalline basement rocks, dispersed, short-period surface-waves (in the range of .2 to 5 seconds) that have propagated through sedimentary basins provide valuable information about the seismic velocity structure of such basins. Several investigations of shallow crustal structure using dispersed, short-period, fundamental-mode, Rayleigh waves (Rg) are listed in Table 1. In these studies, seismic velocity models of the upper 2-3 kilometers of the crust were obtained through inversion of the observed dispersion data. In many of these studies, mining explosions or other near surface explosions were utilized as sources of seismic energy. Explosions at or near the surface and earthquakes with shallow foci are efficient sources of Rg waves (Kafka and Reiter, 1987). In two of these studies, short-period Love waves were noted (Anderson and Dorman, 1973; Bath, 1975). In both cases, the Love waves were determined to have been of such poor quality that they were not used as a constraint in the inversion process.

The University of Kansas and Lawrence Livermore National Laboratory jointly deployed a seismic array in southeastern Kansas from July 1986 to March 1987. The

array was located in northeast Elk County (Figure 1) and was comprised of 13 three-component stations (Figures 2 and 3). The objectives of the deployment were to:

1) Observe the properties of seismic wave propagation from earthquakes and quarry explosions in a region similar to that of the USSR, where a similar array might be deployed if a nuclear test ban treaty is signed.

2) Optimize system parameters and data analysis techniques associated with the array, i.e., improve event detection and location.

3) Determine the velocity structure of the upper kilometer of the earth's crust using short-period, surface-wave dispersion.

The southeastern Kansas region was chosen as the site for this deployment because it is geologically similar to a region in the USSR where underground nuclear testing occurs.

The presence of dispersed, short-period Rayleigh and Love waves recorded at the array from mining explosions in southeast Kansas and northeast Oklahoma, indicate that a surficial, low-velocity layer, or

layers, on the order of one kilometer total thickness exists. This layer appears to correspond to the Paleozoic sedimentary section, which has been found to have a low velocity with respect to the underlying Precambrian granitic basement (Steeples and Miller, 1987). A total of five events displaying Rg wave trains with periods ranging from 0.6 to 3.1 seconds were recorded from five different locations (Figure 4). Upon rotation of the N-S and the E-W components to radial and transverse components, dispersed, short-period Love waves with periods ranging from 0.5 to 3.2 seconds became apparent.

Calculation of the group-velocity dispersion curves for both the Rg and Love-wave phases was facilitated by the multiple-filter analysis method. The seismic velocity structure between the source and the array was derived for each of the five recorded events. The Rg and Love-wave group-velocity dispersion curves were inverted by trial-and-error comparison with theoretical dispersion curves generated from various models of the upper crust.

TABLE 1.

Group velocity of Rg in various regions

	*Period (sec)	Group velocity (km/s)	Region
a	0.5 - 5.0	1.5 - 3.0	Illinois Basin-Ozark Uplift
b	0.4 - 2.0	1.7 - 3.0	Cincinnati Arch
c	0.6 - 2.8	2.2 - 3.0	India
d	0.2 - 1.5	1.2 - 3.1	Southern N.Y.
e	0.5 - 1.8	2.5 - 3.0	Sweden
f	0.5 - 2.0	2.0 - 3.3	Southern New England
g	0.4 - 1.6	2.4 - 3.3	Southeast Maine

*a = McEvilly and Stauder (1965), b = Herrmann (1969), c = Bhattacharya and Srivastava (1973), d = Anderson and Dorman (1973), e = Bath (1975), f = Kafka and Dollin (1985), g = Kafka and Reiter (1987).

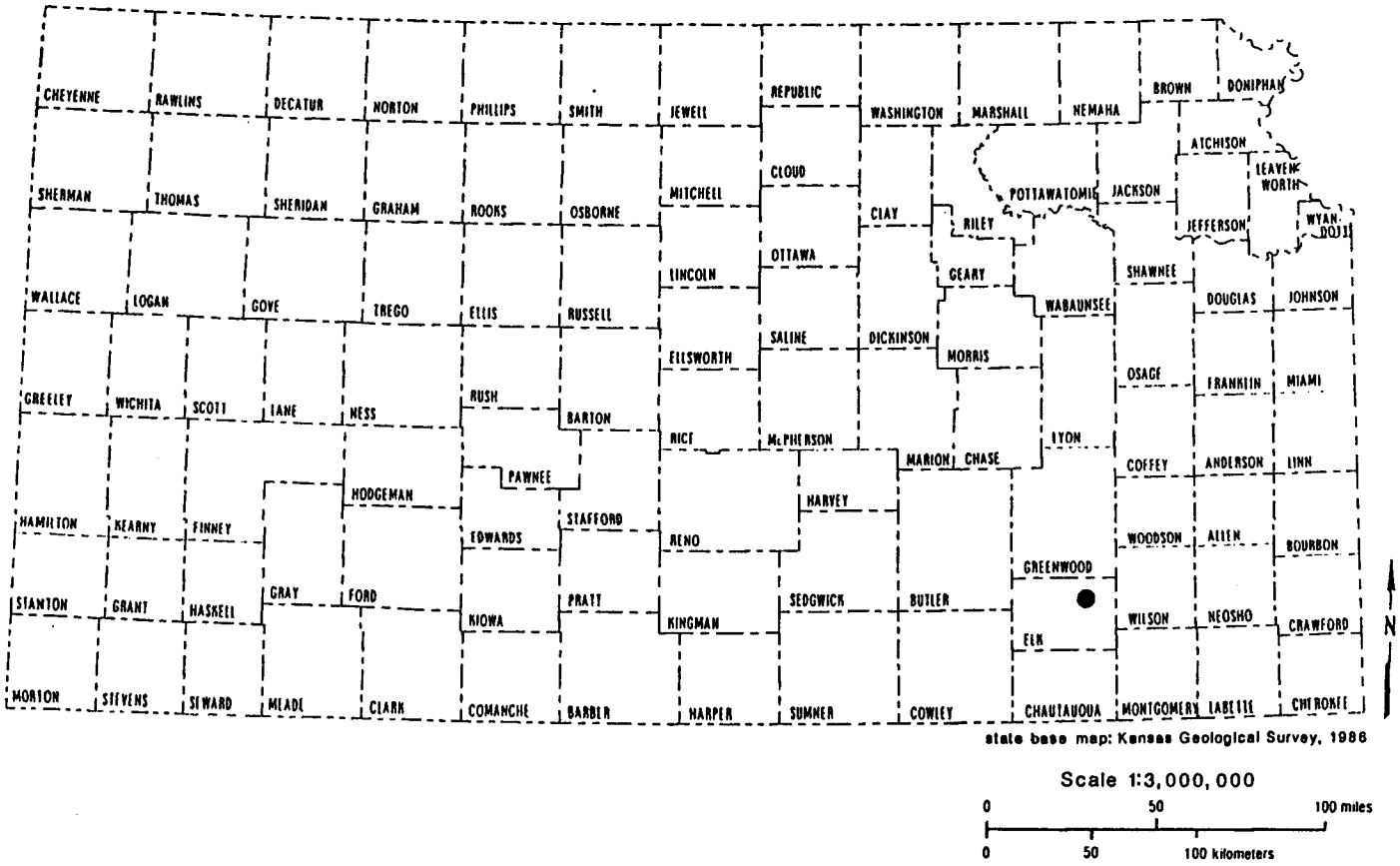

Figure 1. Location of the seismic array in Kansas.

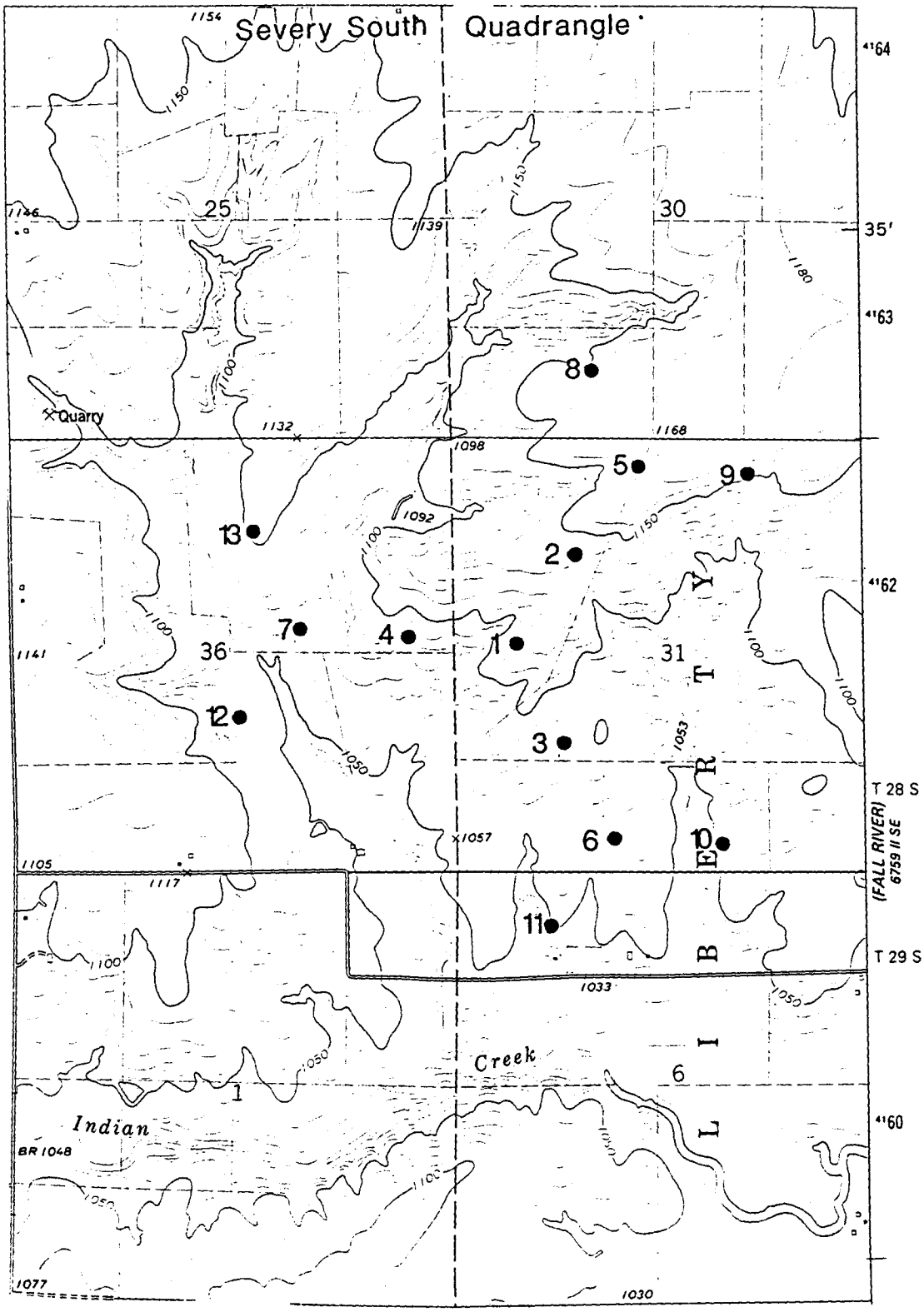

Figure 2. Locations of array stations superimposed on a map of surface topography.

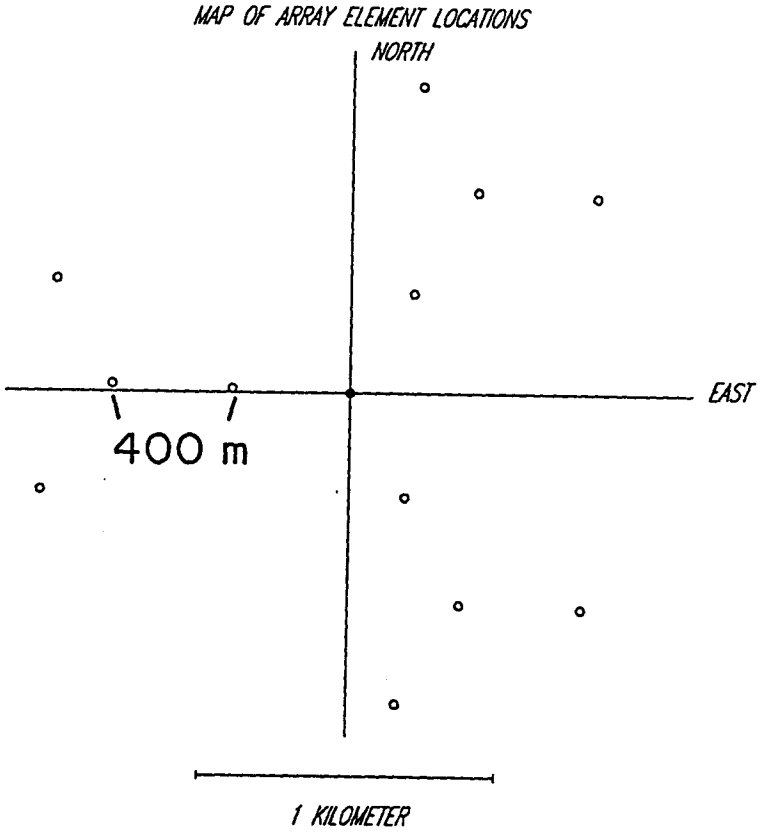

Figure 3. Geometry of the array.

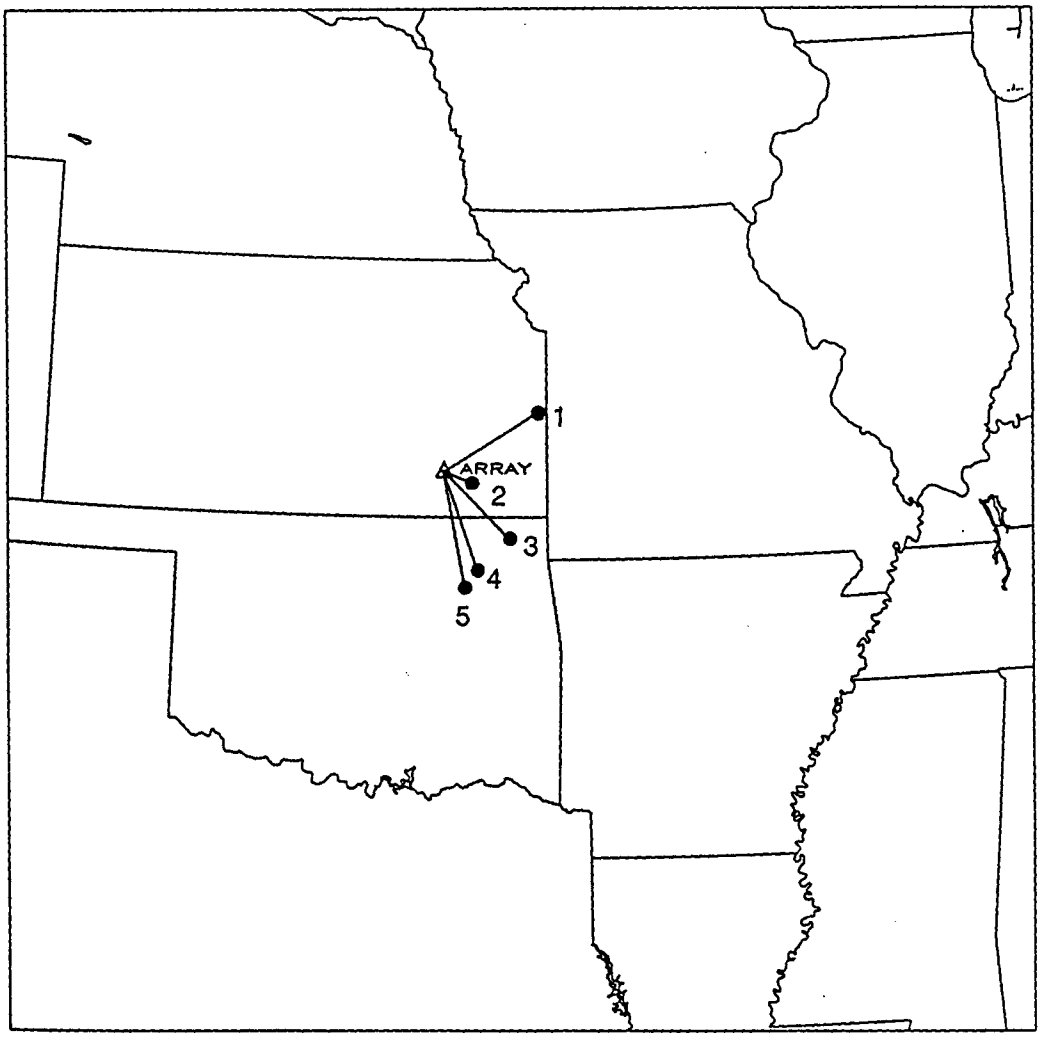

Figure 4. Locations of the mining explosions and the array.

GEOLOGICAL SETTING

The array was located in northeast Elk County, Kansas, situated atop Pennsylvanian limestones of the Shawnee Group. Subjacent strata are Paleozoic sedimentary rocks which extend to the Precambrian basement at 900 meters depth. The sedimentary section thickens to the south into the Cherokee basin, and thins to the east along the Bourbon arch (Figure 5). The sedimentary section throughout the region is composed of three major stratigraphic units of varying thickness (Figure 6). These three units are summarized:

1) Rocks of Pennsylvanian age, composed of marine limestones and shales alternating with nonmarine clastic deposits (Merriam, 1963). Rocks of Pennsylvanian age out crop at the surface over the entire region of this study. The Pennsylvanian rocks unconformably overlie rocks of Mississippian age.

2) Rocks of the Mississippian age, composed largely of limestones that overlie the thin Chattanooga Shale. The Chattanooga unconformably overlies Cambro-Ordovician rocks.

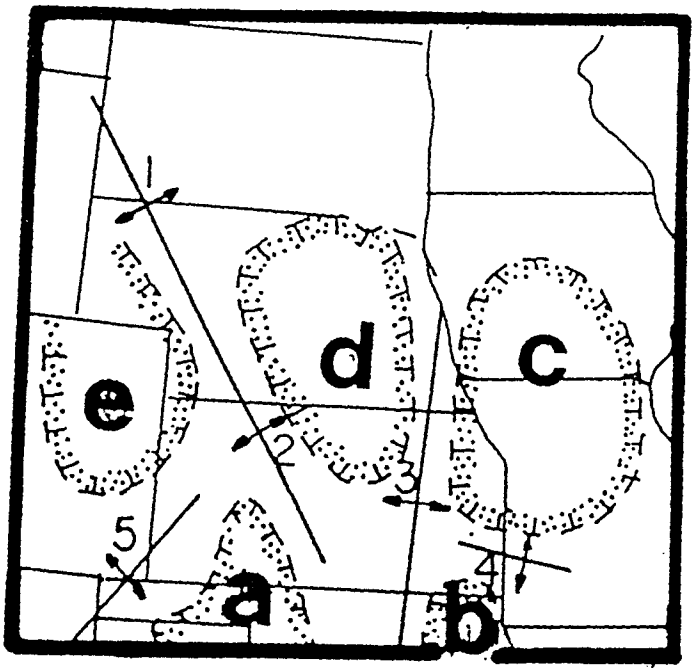

Figure 5. Locations of the array with respect to upper Paleozoic structural features in the Mid-continent. Uplifts: 1 Cambridge, 2 Central Kansas, 3 Nemaha, 4 Bourbon, 5 Los Animas; Basins: a Hugoton, b Cherokee, c Forest City, d Salina, e Denver. (modified from Steeples, 1982).

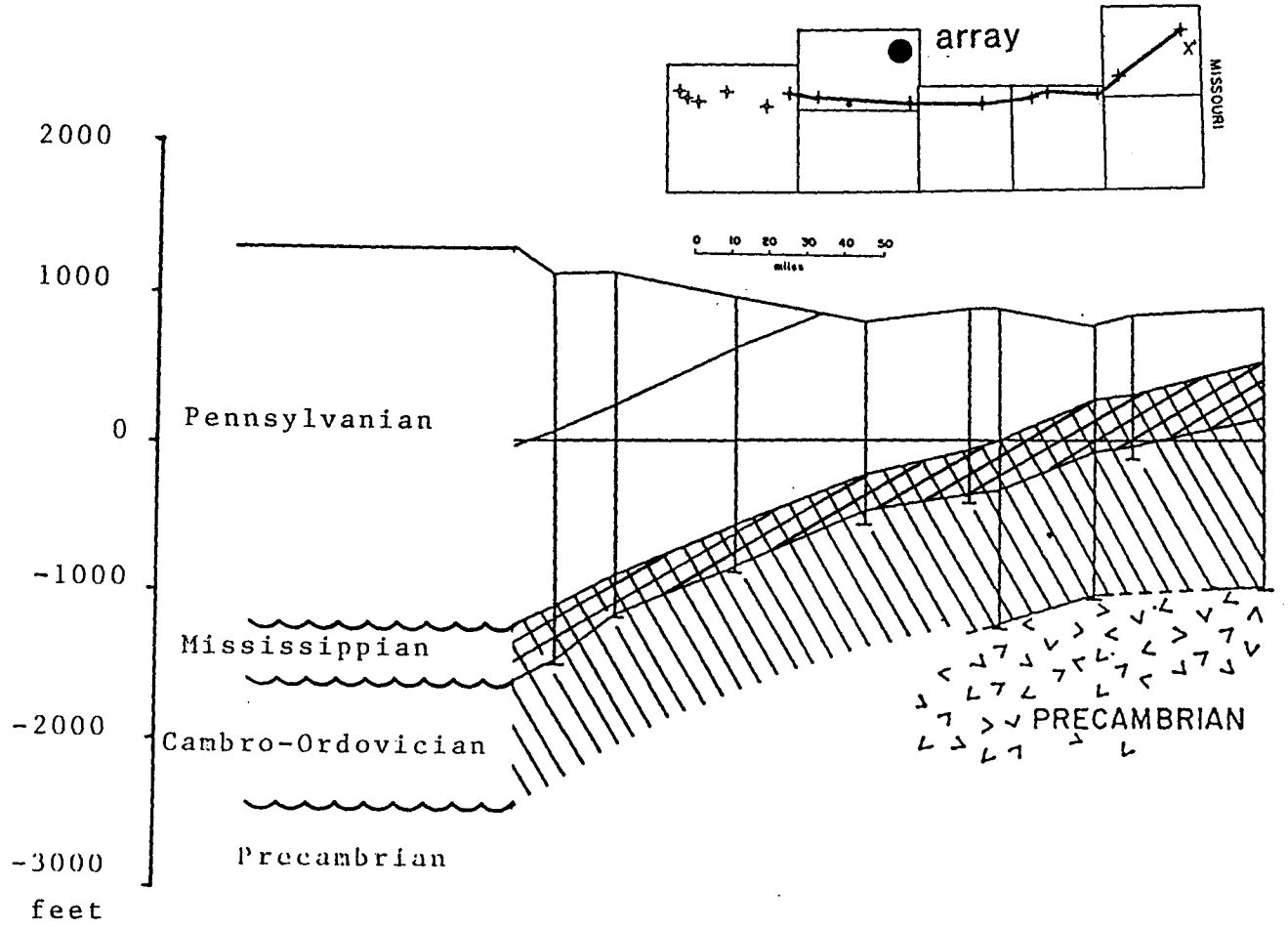

Figure 6. Cross section of the Paleozic sedimentary section to the south of the array. Note the three major stratigraphic units that comprise the section (modified from Merriam, 1963).

3) Rocks of Cambro-Ordovician age. This unit is named the Arbuckle Group and is composed of dolomites and limestones. The Arbuckle Group typically unconformably overlies the Precambrian basement rocks.

SURFACE-WAVE DISPERSION IN SIMPLE MODELS

Surface-waves are seismic waves that travel along the free surface on an elastic solid. The most commonly observed types of surface-waves are Rayleigh waves and Love waves. The particle motion of Rayleigh waves is elliptical and retrograde in the vertical plane defined by the vertical and radial directions. Love waves are observed only when there is a low-velocity layer overlying a medium in which the elastic waves have a higher velocity or when there is a systematic increase of velocity with depth. The particle motion for Love waves is in the transverse direction.

The simplest earth model is that of an infinitely deep, homogeneous half-space. Rayleigh waves traveling on the free surface of this half-space will propagate with a velocity of about 0.9 of the shear-wave velocity of the medium. For a model of this type, no dispersion

will be observed. Love waves will not propagate in this medium, because there is not an increase in velocity with depth.

A more complicated model is that of a finite layer of thickness (h) overlying an infinitely deep, homogeneous half-space with a contrast of physical properties (Figure 7). The physical properties of the media (compressional-wave velocity, shear-wave velocity and density) were chosen so that this model approximately represents a thin layer of sedimentary rocks (one kilometer of limestones and shales) overlying a granitic basement. For Rayleigh waves (as well as Love waves) the amplitude of particle motion decreases exponentially with depth according to the wavelength (Dobrin et al., 1951). As a result of this exponential decrease with depth, the motion for short wavelengths does not appreciably penetrate the basement (Figure 7), and the Rayleigh-wave phase velocities for the shorter wavelengths are about 0.9 of the shear-wave velocity of the upper layer. As the wavelengths increase, the particle motion penetrates to greater depths (Figure 7). The higher velocity at depth exerts an increasing influence on the Rayleigh waves as the wavelength increases, so the phase velocity increases as a function of wavelength. As the ratio of the wavelength to the

thickness of the upper layer goes toward infinity, the phase velocity approaches a value of about 0.9 of the shear-wave velocity of the lower medium. If the velocity structure increases with depth, then the longer period surface-waves travel at higher velocities than the shorter periods. Dispersion of this sort is said to be normal (Figure 8). If the velocity structure decreases with depth, shorter period components will travel at higher velocities than the longer period components and the dispersion is said to be reversed.

In dispersive media, a surface-wave train spreads out as it progresses away from the source. The phase velocity (C) is the velocity at which a pure frequency component propagates. When a spectrum of frequencies is produced by a source, their interference produces a pattern which is also propagated through the medium, and it is this pattern which is recognized as a signal (Garland, 1979). The propagational velocity of this interference pattern is defined as the group velocity (U). The relationship between the phase and group velocity is given by:

$$U = C - \lambda(dC/d\lambda), \qquad (1)$$

where λ is the wavelength. The lower part of Figure 7 shows a plot of the phase and group velocity of the fundamental-mode Rayleigh wave as a function of period, determined for the aforementioned sedimentary layer over granitic basement model.

Group-velocity dispersion can be determined from a single record of a dispersed wave-train. This is facilitated by dividing the arrival times of different periods into the distance between the source and the receiver:

$$U_n = x/t_n \tag{2}$$

where U_n is the group velocity determined for each of the n observed periods, x is the offset between the source and the receiver and t_n are the arrival times for the various observed periods. Phase velocity can be determined by measuring the change in phase ($\Delta\phi$) between two recording stations situated along a propagation path perpendicular to the source:

$$C_n = 2\pi\,(\Delta x)/T_n(\Delta\phi) \tag{3}$$

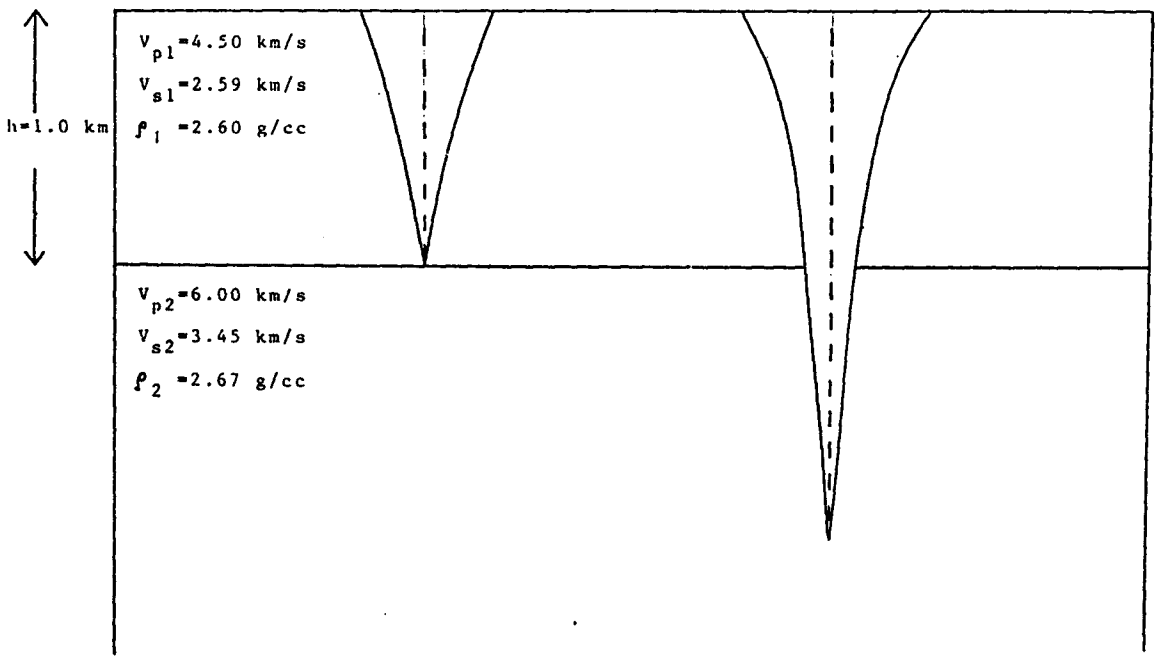

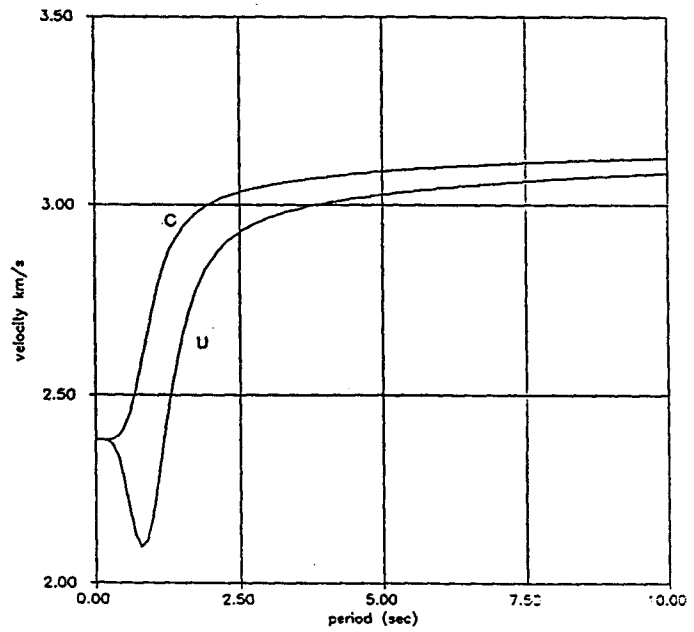

Figure 7. A layer over half-space velocity model, with the decay of the vertical particle motion of the fundamental-mode Rayleigh wave, for two different wavelengths. The longer of the two wavelengths is on the right. Also shown is a plot of the theoretical phase-velocity (C) and the group-velocity (U) dispersion curves, as calculated for the model.

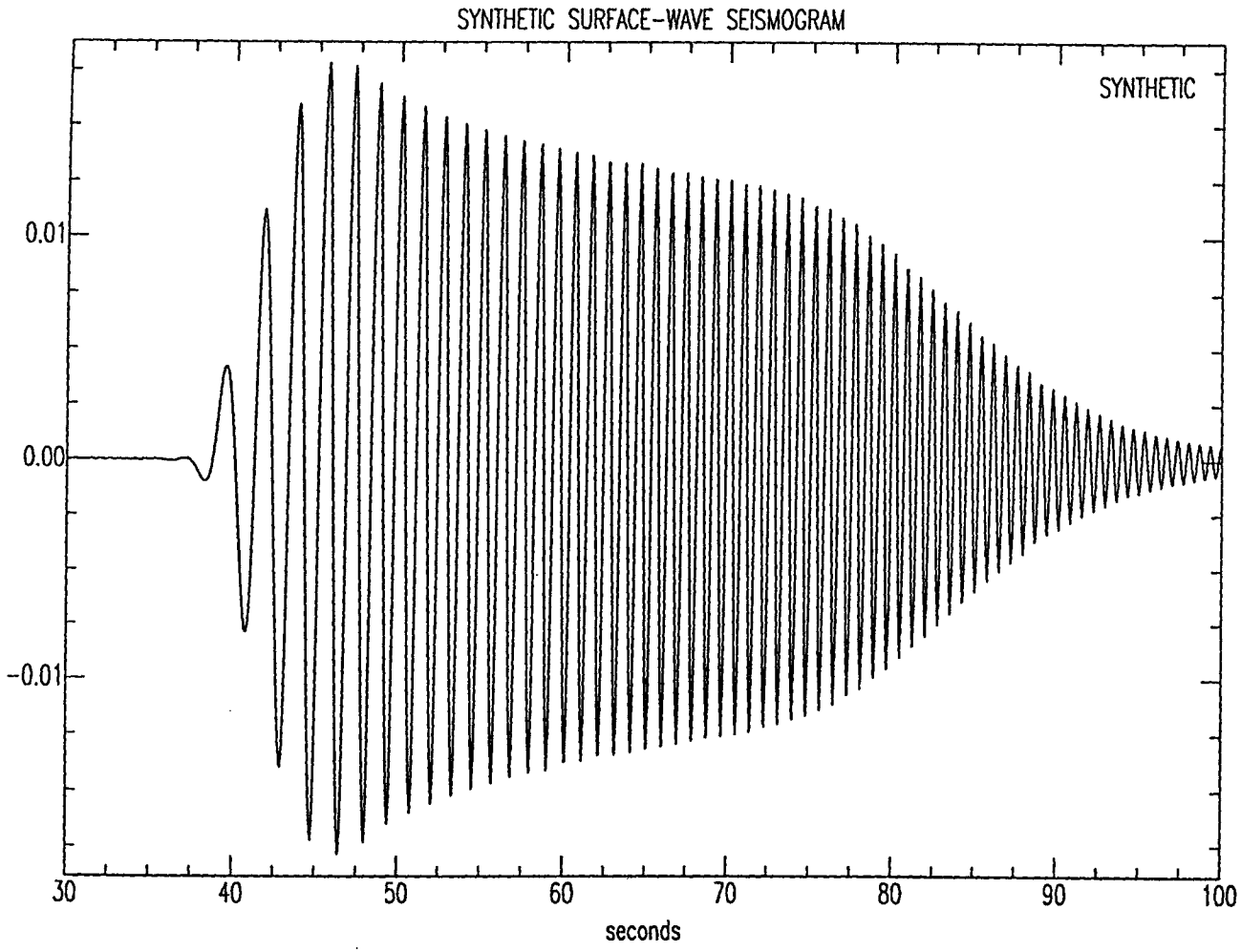

Figure 8. Normally dispersed surface-wave seismogram. Note that the the period decreases with time (the frequency increases).

A

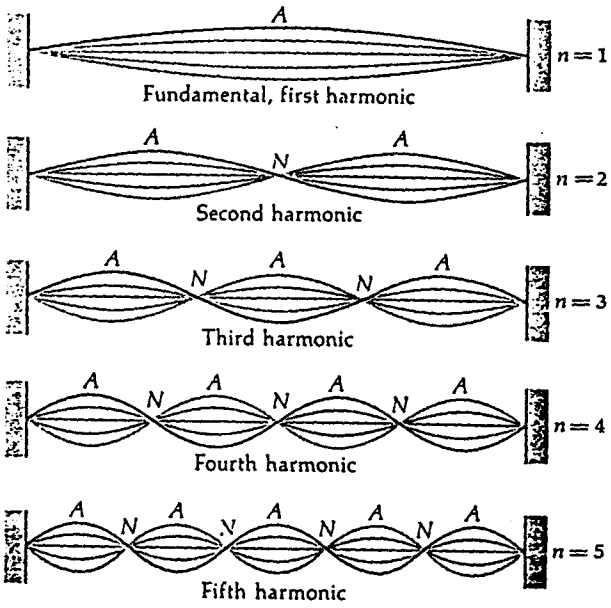

B

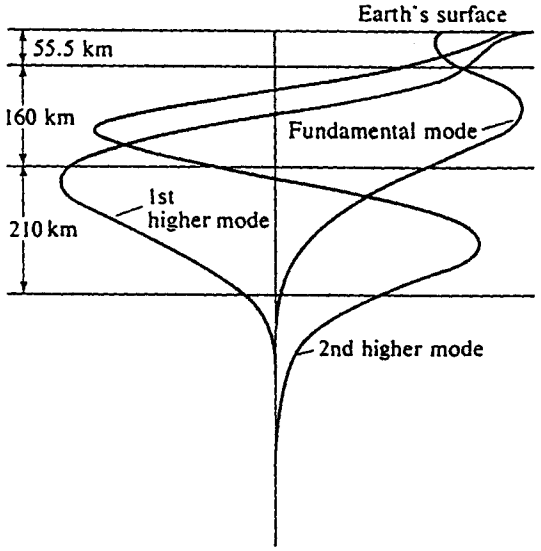

Figure 9. A: Standing waves on a string fixed at both ends. The points labeled A are antinodes, those labeled N are nodes (after Tipler, 1982); B: Displacement with depth for the first three modes of a Love wave for a period of 30 seconds (after Bolt, 1982).

where C_n is the phase velocity determined for each of the n periods (T_n) and Δx is the distance between the two recording stations.

A well known physical phenomenon is that a vibrating string, fixed at both ends is able to perform a fundamental vibration in which the wavelength is equal to twice the length of the string. In addition, the string can simultaneously perform a number of overtones (higher modes) with wavelengths equal to the length of the string, or fractions thereof (Figure 9). Similar conditions prevail for surface-waves in elastic media. Surface-waves with fundamental-mode displacement, as well as higher-mode surface-waves (1st higher, 2nd higher, etc..) are generated by a seismic source (Figure 9). Higher-mode surface-waves have shorter periods than do the fundamental-mode waves, but travel at higher velocities and also experience dispersion in layered media.

ARRAY INSTALLATION

The location of the array site was chosen for a variety of logistical and practical reasons, but the most important was the relatively low level of noise present in pre-deployment noise tests. With prior

knowledge of the array geometry (Figure 3), each station location was scouted and approximately located, so that a minimum number of stations were located near roads, fences, trees or other potential sources of unwanted seismic noise. The exact site for each station was then located using advanced surveying techniques.

Once exact locations were known, the soil overlying the limestone bedrock at each station was removed, exposing the bedrock surface. The thickness of the soil layer varied from a few inches for stations located on hills, to as much as fifteen feet for stations located in valleys. A layer of concrete was then laid over the bedrock surface to make a stable platform on which to place the seismometers. Great care was taken to follow the same procedure for each station so that the individual site responses would vary as little as possible across the array.

Instrumentation was identical for each of the thirteen stations. Each station contained three Teledyne Geotech S-13 seismometers. These seismometers have a one-Hertz natural frequency and were calibrated to detect ground acceleration. The seismometers were aligned in vertical, north-south and east-west directions. The output signal from each component was amplified and transmitted via FM radio to the central

recording site, located on the western edge of the array. At the recording site, the signal was digitized at a rate of 120 samples per second, multiplexed, and written onto a computer disk, and eventually written onto tape.

DATA ACQUISITION

The array began operation in late July, 1986, with the goal of recording as many local and regional earthquakes, teleseisms, and mining explosions as possible. Data were acquired during two separate recording phases, an automated-event-trigger phase and a forced-recording phase.

Data were recorded in the automated phase from the incipience of array operation until three days prior to the shutdown of the array. During this phase, digital data from the vertical components of stations 1, 5, 6, and 7 were continuously monitored by a computer. The computer determined if a seismic disturbance had occurred at each individual station. A disturbance was defined as an increase in ratio of the average amplitude over a small time-window with respect to the average amplitude over a longer time-window. If three of the four stations being monitored experienced a disturbance

within a pre-defined period of time (usually one second), then an event was determined to have occurred and seismic waves were assumed to be propagating across the array. When an event occurred, the recording system was triggered and the previous thirty seconds of data (continuously stored by the computer) and the following 120 seconds of data for all 39 channels were recorded and stored on disk as individual event files.

During this recording phase, numerous events were recorded, but only a small number of these exhibited an Rg phase. Apparently the energy yield of mining explosions in the region was so small that they fell below the threshold of detection; yet, lowering of the threshold within the acquisition software would have significantly increased the number of false triggers which would have filled the available memory space too quickly.

The lack of data recorded made the second recording phase necessary. During the last three days of the array deployment, the data acquisition system was set to continuously record on all 39 channels for the period between 9 AM and 3 PM, Central Standard Time. This particular time-window was chosen because many of the mines in the region set off explosions during these hours.

EVENT DETECTION

Events recorded during the first recording phase consisted of desired seismic events (earthquakes and mining explosions) as well as a large number of unwanted, false-triggered events. Most of the false triggers were due to wind, thunder claps, and ground roll generated by passing automobiles and trains. For each event recorded, the thirteen vertical traces were printed out and visually inspected (Figure 10). Earthquakes and mining explosions were catalogued, while the spurious events were discarded. During this recording period, events exhibiting an Rg phase were limited to chemical explosions from a coal mine located at a bearing of 58 degrees, 156 kilometers distant from the array (event 1, Figure 4).

Detection of events from data acquired during the forced-recording phase required utilization of the signal enhancement capabilities of the array. It was necessary to employ these capabilities so that any small events containing an Rg phase did not go undetected.

Because of the overwhelming amount of data recorded during the forced-recording phase, only the vertical components of each of the thirteen stations were used in the analysis. Large, unmanageable, continuous data

files were broken into smaller files, 105 to 120 seconds long. The analysis described below was then performed on the thirteen vertical traces that comprised these shortened files (Figure 11).

Using the knowledge of the array dimensions and geometry (Figure 3), vertical signals can be time shifted as if plane waves from some particular azimuth are propagating across the array with some particular apparent velocity. Both the azimuth and the apparent velocity must be specified in the shifts. After the signals are shifted, they are stacked. This process is known as beamforming and the sum of each stack is referred to as a beam. Beamforming will enhance events that arrive from similar azimuths and have apparent velocities similar to those chosen for the shifts. The assumption is that sources of noise are uncorrelated across the array and stacking numerous signals will statistically cancel the noise. Beamforming improves the signal-to-noise ratio of an event by a factor of approximately $N^{1/2}$ (where N is the number of array sensors).

Beams were calculated for twelve different azimuths (Figure 12), using an apparent velocity of 6.0 km/s. This velocity was chosen because it is the regional compressional-wave velocity in the upper crust (Steeples

and Miller, 1987). The output for the beam at each azimuth was printed out (Figure 13), along with an additional beam for teleseismic events. The teleseismic beam assumes an azimuth of zero and an apparent velocity approaching infinity (i.e. plane-waves traveling vertically upward).

Figure 13 shows a plot of the beams formed from the data shown in Figure 11. A comparison of the two figures shows that the signal-to-noise ratio is improved by beamforming, regardless of the azimuth chosen. Therefore, an event that may have been previously undetected, is now seen on all thirteen channels of the beamforming output. Inspection of the thirteen channel beamforming output can give some quantitative information about an event. Body and surface-wave phases present can be identified and the back-azimuth of the event can be estimated. The back-azimuth is estimated by finding the best stacking azimuth for the first arrival of the compressional wave. For the event in Figure 13, the phases present are P*, S* (P and S-wave phases refracted deep within the crust), and Rg. The traces at 150° and 180° have compressional-wave first arrivals with high signal-to-noise ratios relative to the other traces.

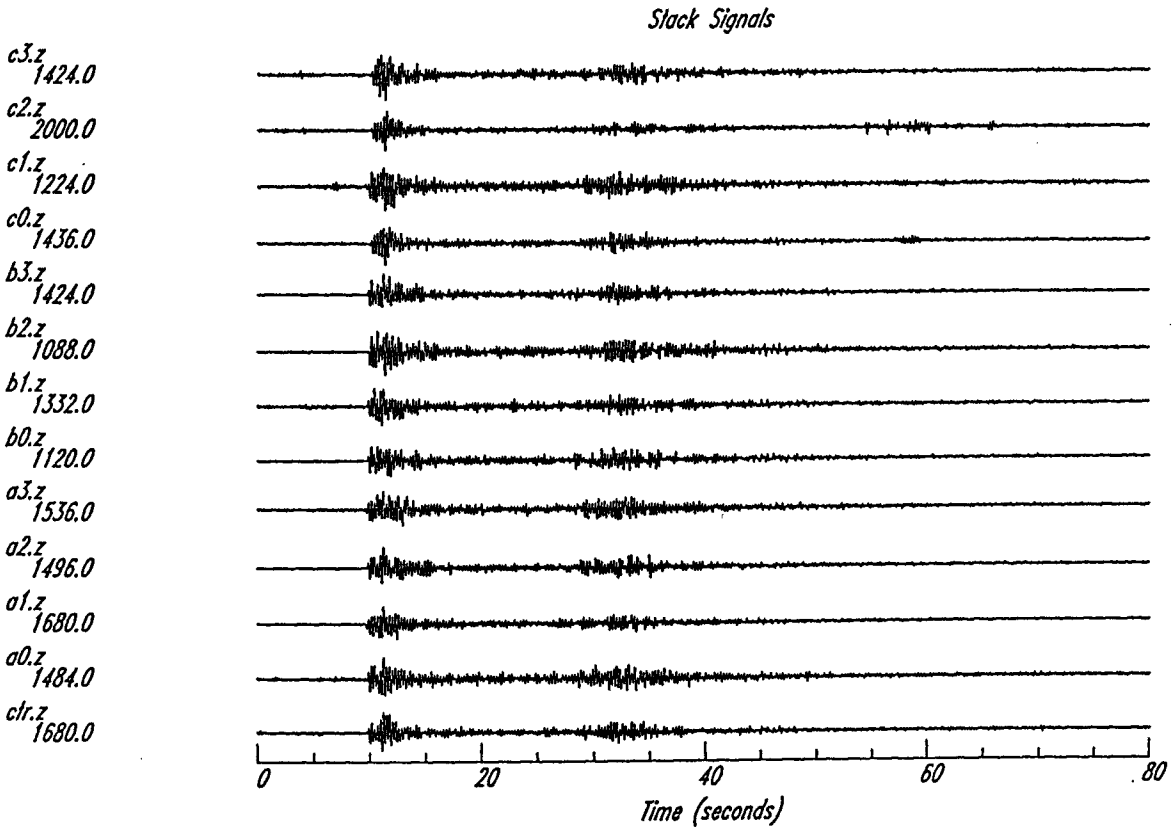

Figure 10. Print out of the thirteen vertical components of an event recorded during the event-trigger phase. The code before each trace represents the station name and the component, (z = vertical). The number shown is the maximum amplitude along the trace. The signals are normalized prior to plotting.

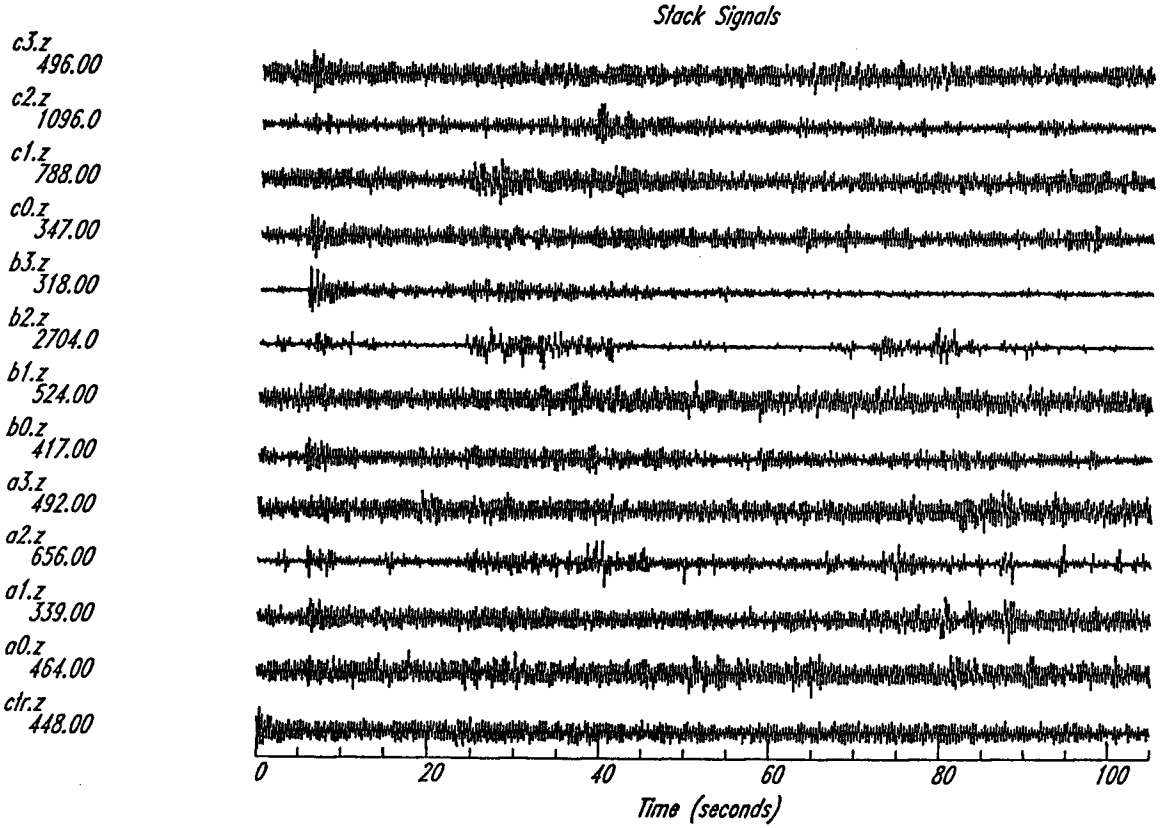

Figure 11. Thirteen vertical components for a 105 second block of data, recorded during the continuous recording phase. Note an event at about 6 seconds.

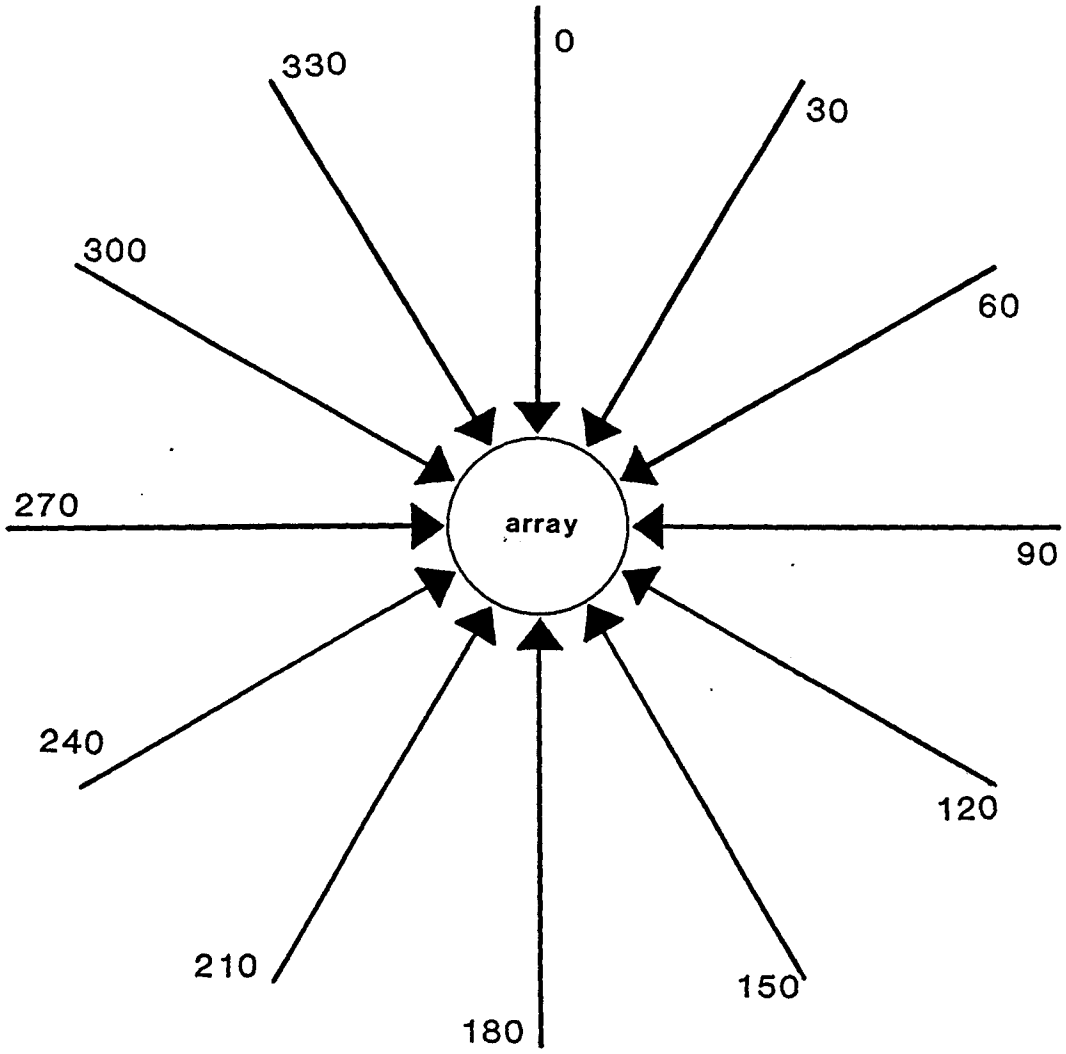

Figure 12. Bearings used in the beamforming process.

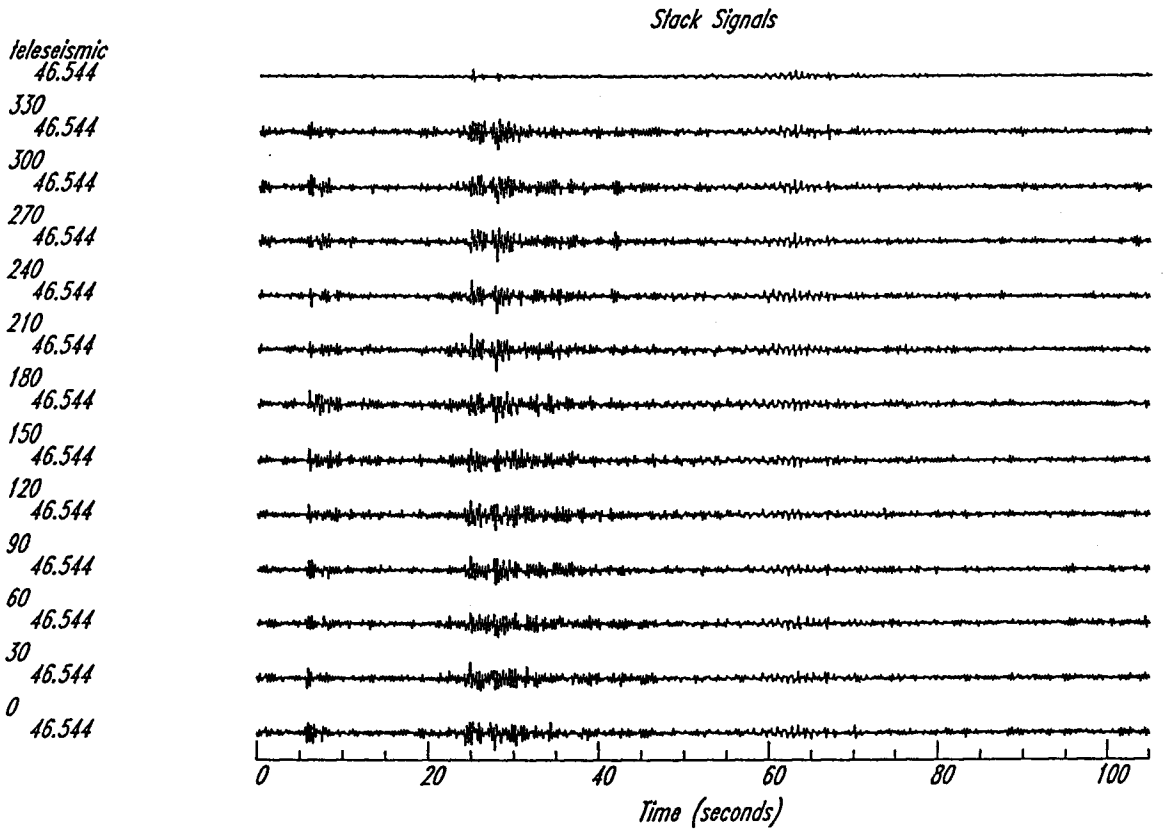

Figure 13. A plot of the beams formed for a set of azimuths. These beams are generated from the data shown in Figure 11. The bearing of the beam and the maximum amplitude are shown to the left of the trace.

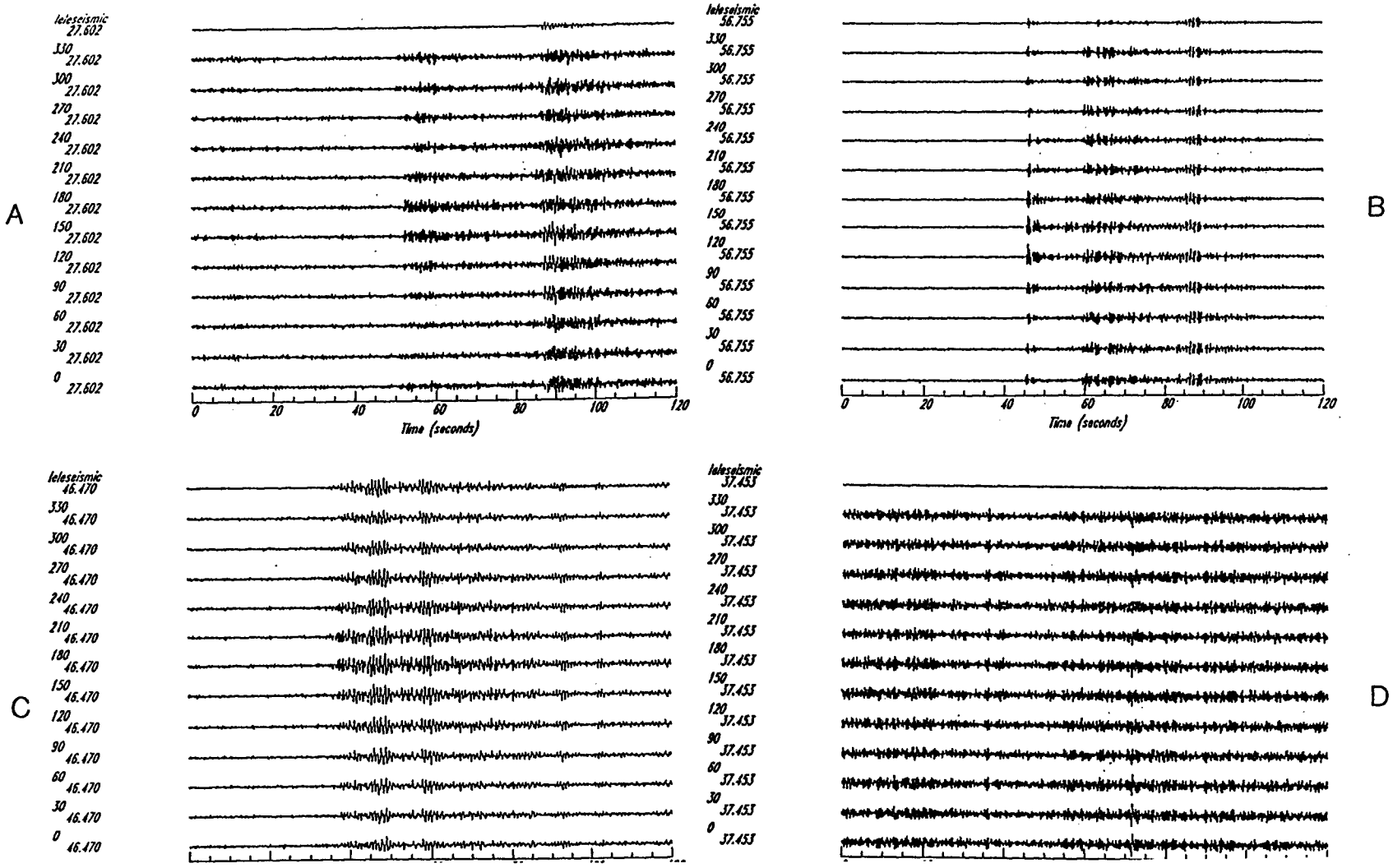

Figure 14. Beamforming output for four events. A: a quarry blast from the south; B: a mining explosion from the southeast; C: a teleseism from Mexico; D: a small quarry blast from the northeast.

The multi-azimuthal beamforming procedure was repeated for the entire block of forced-record data, operating upon the transected files individually. Events were found by visual inspection of the printouts. Figure 14 shows several events found using the beamforming procedure. Events from four different azimuths exhibiting an Rg phase were found in the data recorded during the forced-recording phase (events 2-5, Figure 4). Events containing an Rg phase were recorded from five different azimuths during the full operational period of the array.

DETERMINATION OF BACK-AZIMUTH

Once events displaying an Rg phase were identified, it was necessary to determine the back-azimuth for each. The back-azimuth is defined as the bearing from which an event arrives at the array, measured from the north, in a clockwise sense. Knowledge of the back-azimuth of an event serves three purposes:

1) It adds azimuthal constraint in the determination of the geographic origin of the seismic energy source.

2) It allows an estimate of the path along which the surface waves have propagated between the source and the receiver, to be made.

3) It facilitates determination of the angle that the horizontal components are to be rotated through, in order to resolve the north-south and east-west components into radial and transverse components.

Estimation of the back-azimuth was permitted by calculation of the frequency-wavenumber power spectrum. The frequency-wavenumber power spectrum shows how the power is distributed among different wave velocities and bearings (Aki and Richards, 1980). If the array is considered to exist on an $x-y$ plane, a wave field, $f(x, y, t)$, can be transformed to the frequency-wavenumber domain by a three-dimensional Fourier transform:

$$F(k_x, k_y, \omega) = \int\int\int_{-\infty}^{\infty} f(x, y, t)\exp(-ik_x x - ik_y y + i\omega t)\,dxdydt, \quad (4)$$

where ω is the angular frequency and $F(k_x, k_y, \omega)$ is the frequency-wavenumber spectrum. This gives the amplitude and phase of plane waves that propagate with an apparent velocity c in the $x-y$ plane, and in the direction specified by the azimuthal angle ϕ:

$$k_x = \omega \cos \phi / c,$$

$$k_y = \omega \sin \phi / c, \qquad (5)$$

The power spectrum is determined by absolute-value squaring and averaging of the Fourier-transformed data.

An ideal array has an identical response at each of its sensors. In the case of the array used in this study, the character of the signals varied somewhat from station to station (Figure 15). Because the recording instruments and the electronics were identical at each station, the site response must have been the factor in the variation of the response across the array. The events were lowpass filtered, prior to estimation of the frequency-wavenumber power spectra, to remove the high-frequency site response of each station and make the signals similar in amplitude and frequency content across the array (Figure 16).

For each event, a 2 to 15 second time-window was chosen around a particular phase on the vertical-component traces (Figure 17). The predominant frequency within the chosen window (ω_o) was determined and the wavenumber spectrum calculated for this particular frequency. This can be represented by a plane in

frequency-wavenumber space (Figure 18). The power spectrum at this frequency was then calculated and plotted with the k_y-axis aligned in the north-south direction and the k_x-axis in the east-west direction (Figure 19). The back-azimuth of the chosen phase or of the windowed seismic energy was given by the azimuth of the power spectrum maximum in the $k_x - k_y$ plane (Figure 19). The apparent velocity across the array was determined from the relation:

$$k_x^2 + k_y^2 = \omega^2/c^2. \qquad (6)$$

The power spectrum maximum lies on a circle of radius $(k_x^2 + k_y^2)^{1/2}$ and this quantity can be measured directly from the plot of the power spectrum (Figure 19). Since $\omega = \omega_o$ the value of c can be determined.

For each event, the frequency-wavenumber power spectra were determined for windows centered on the P-wave phase and on the Rg phase. The back-azimuth for each of these phases, along with the true bearing from the event location, are listed in Table 2. Seismic traces and frequency-wavenumber plots for each of the five events are shown in Appendix A. Each plot indicates the estimated back-azimuth and the apparent velocity across the array.

Examination of Table 2 reveals that the back-azimuth estimates may differ for the P-wave phase and the Rg phase and that both of these estimates differ from the true bearings of the sources. This indicates that the P-wave and the Rg phases traveled along paths that varied from a straight line between the sources and the array. The reasons for these bearing anomalies are probably different for the individual phases, as the P-wave phase appears to be a refracted arrival from deep within the crust, whereas Rg displacement by definition is confined to the upper 2-3 kilometers of the crust.

In the case of the P-wave, the apparent velocity across the array for events more distant than 100 kilometers (events 1, 3, 4 and 5) ranged from about 6.6 km/s to about 7.3 km/s. These velocities agree with deep-crustal velocities determined from explosion seismic studies in the region (Healy and Warren, 1969). Speculation about the cause of this bearing anomaly from body waves that propagate deep within the crust, is beyond the scope of this thesis, although lateral velocity heterogeneity within the lower crust may be a reasonable explanation. For event 2, the distance is so small (29.6 km) that only a small bearing anomaly was observed.

The bearing anomalies of the Rg phase may have been caused by variations in basement topography. Figure 20 shows a plot of the basement structure with the locations of the array and sources superimposed. Positive topographic expressions in the basement, such as that in northeast Woodson County, Kansas (along the line between the event 1 and the array) may have diffracted surface waves away from the straight-line path between the source and the array. Lateral variations in the seismic velocity of the basement rocks or within the sedimentary section would lead to lateral refraction or reflection of the surface-waves. Bickford et al., (1981) compiled a basement-rock-type map of Kansas and adjacent Mid-continent states on the basis of basement well samples (Figure 21). This map shows that the basement below the array (northeast Elk County, Kansas) is largely epizonal granite, about 1.4 billion years old, whereas the basement below the location of event 1 (extreme northeast Linn County, Kansas) is mesozonal granite, about 1.6 billion years old. Yarger (1983) has speculated on the location of the boundary between these two basement provinces (Figure 21), on the basis of aeromagnetic data. If the epizonal granite to the south has a higher seismic velocity than the mesozonal granite to the north, then surface-waves

generated by event 1 would be refracted towards the west when passing across the boundary between the two basement provinces. This refraction would serve to move the back-azimuth of the surface-wave energy towards the east (as is observed for event 1). Lateral refraction of this sort may also explain the Rg bearing anomalies from the events located in Oklahoma (note that the basement rock-type also changes south of the array, Figure 21). A combination of lateral refraction, reflection and diffraction of the surface-waves by basement structures may be the cause of the observed bearing anomalies.

TABLE 2

True And Measured Back-Azimuths

Event No.	True Back-az	P-wave Back-az	Rg Back-az
1	58°	67°	61°
2	103°	102°	102°
3	145°	141°	137°
4	161°	157°	151°
5	170°	171°	171°

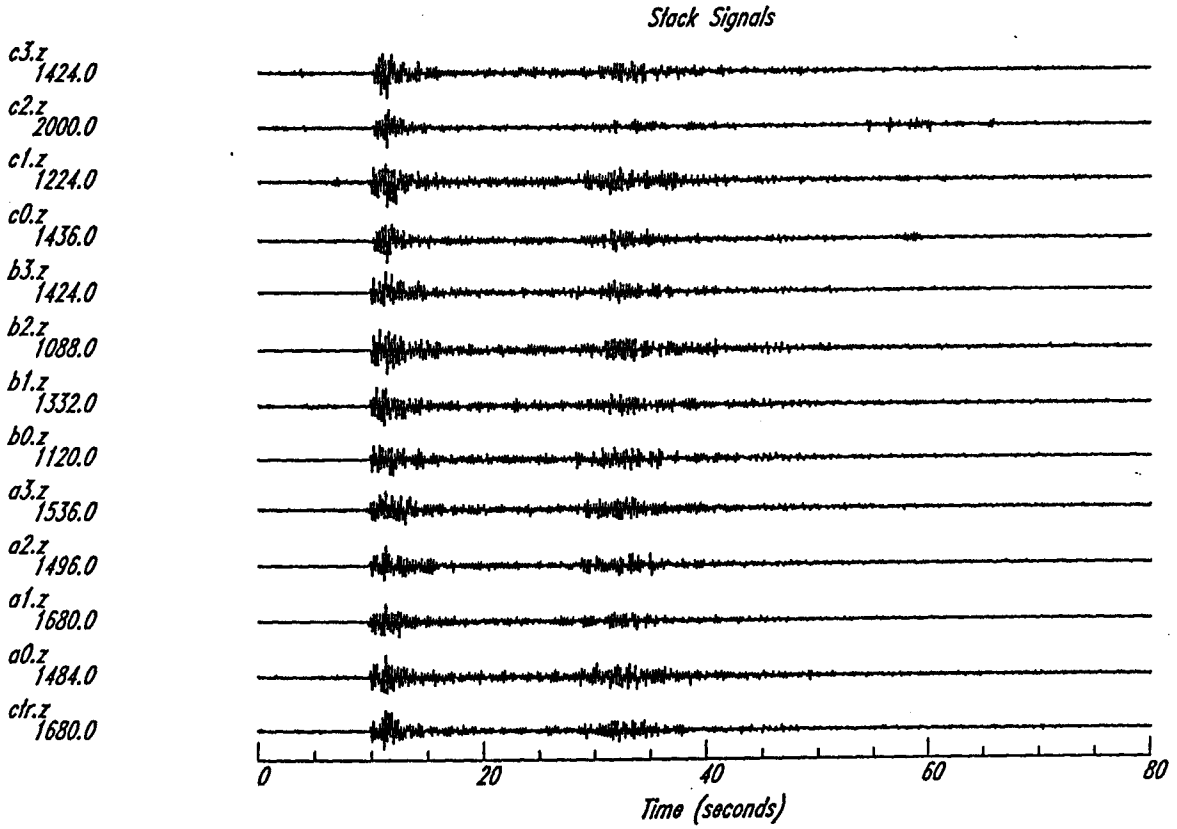

Figure 15. Print out of the thirteen vertical components for an event from the northeast. Note the difference in the character of the signal across the array.

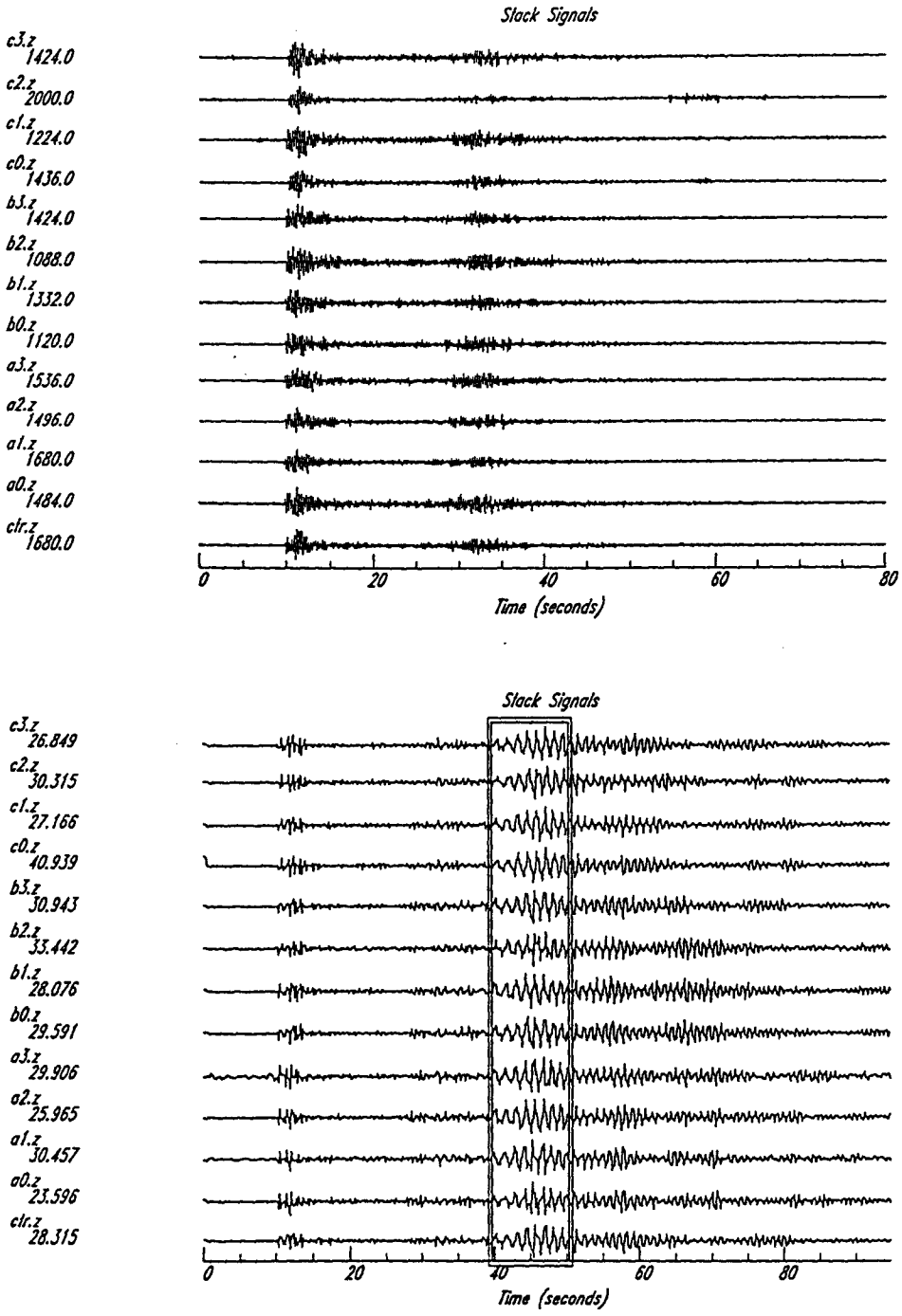

Figure 16. Top: thirteen vertical traces of an event from the northeast; Bottom: The same thirteen traces, filtered with a 1.5 Hz lowpass filter. Note the similarity of the signals across the array after the removal of the high frequency site response, particularly within the indicated window.

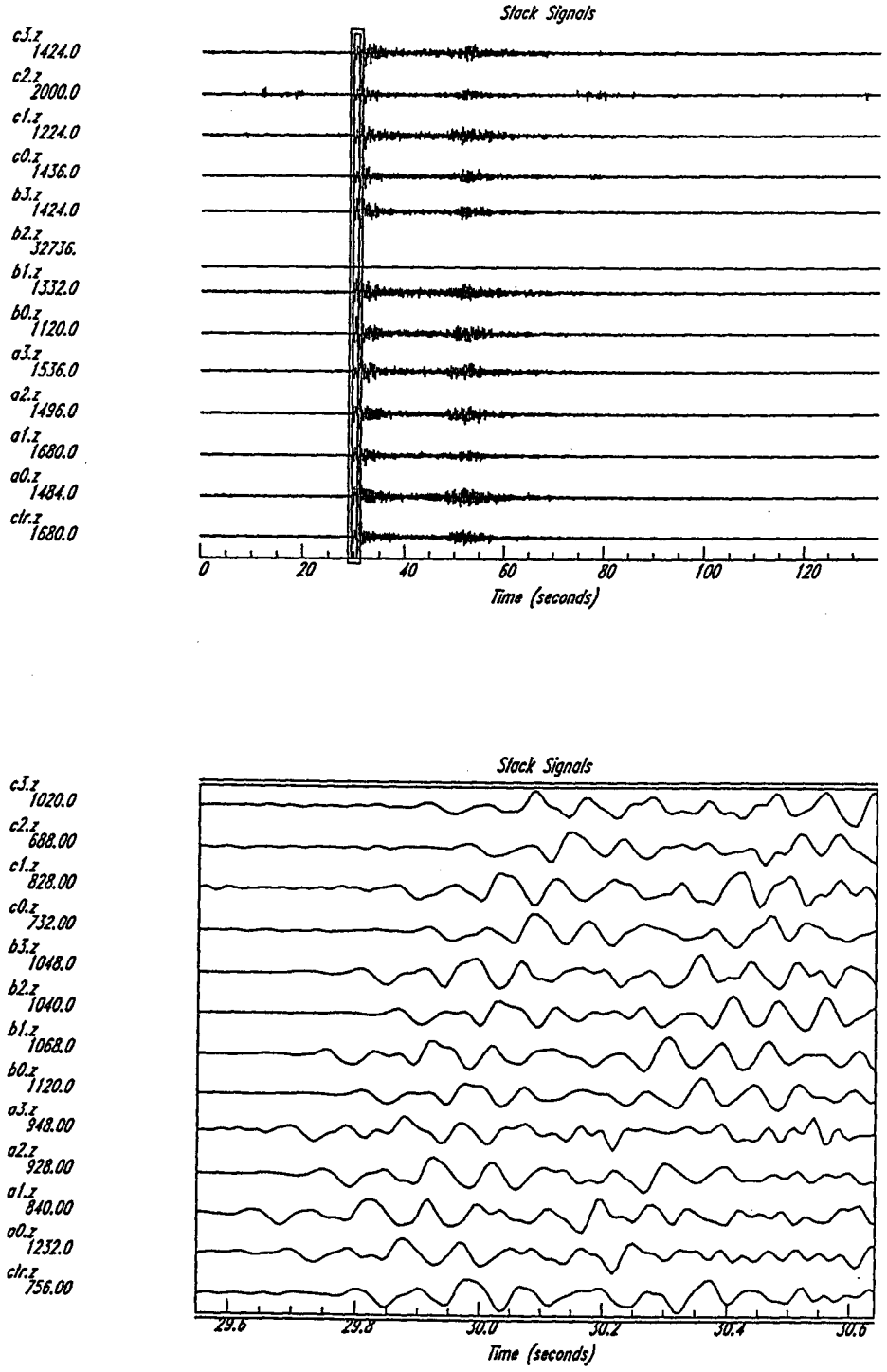

Figure 17. Top: a window chosen around the P-wave first arrival for an event 156 km to the northeast; Bottom: Magnification of the data in the above window. Note the moveout of the P-wave across the array.

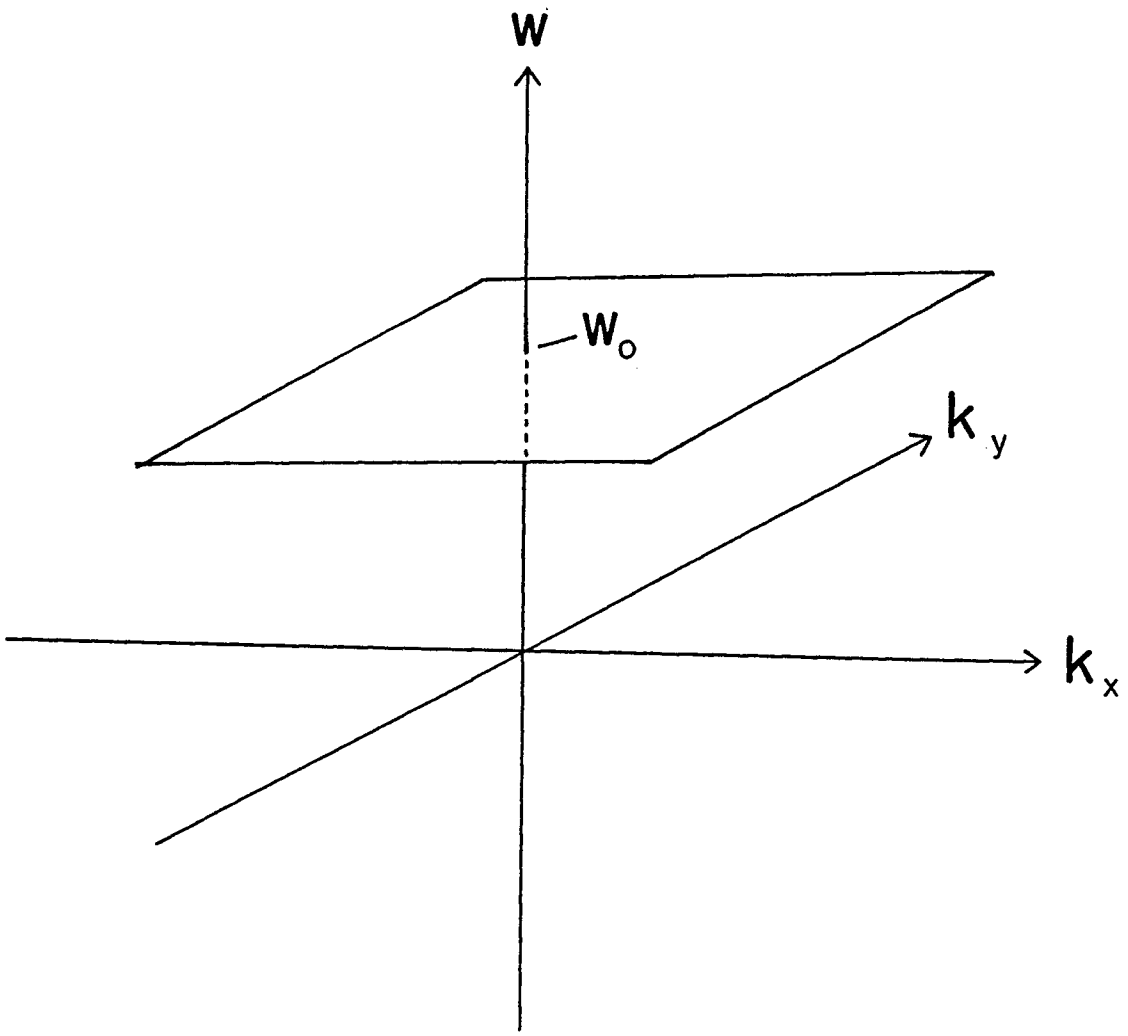

Figure 18. A plane at $\omega = \omega_o$ in frequency-wavenumber space.

NBFK - single window

Estimated bearing: 66.559

Estimated velocity: 6.5627

Analysis frequency: 4.805

Max. horiz. wavenumber: 1.0000

Scaling type: LINEAR

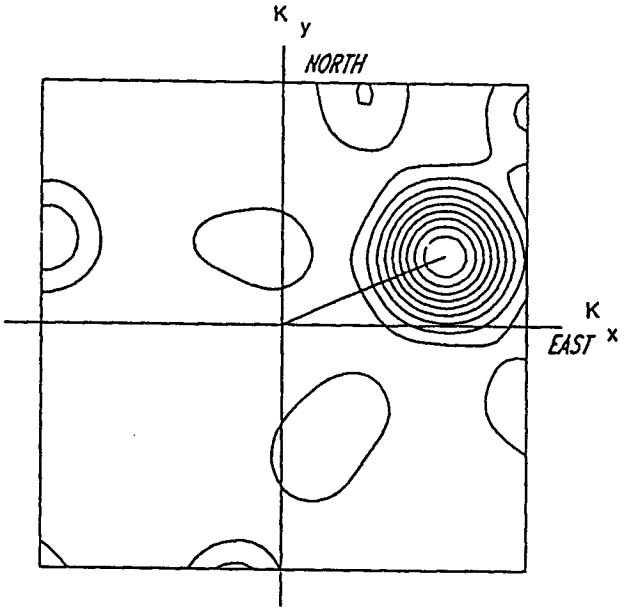

Figure 19. Narrow band frequency-wavenumber power spectrum for the event shown in Figure 17.

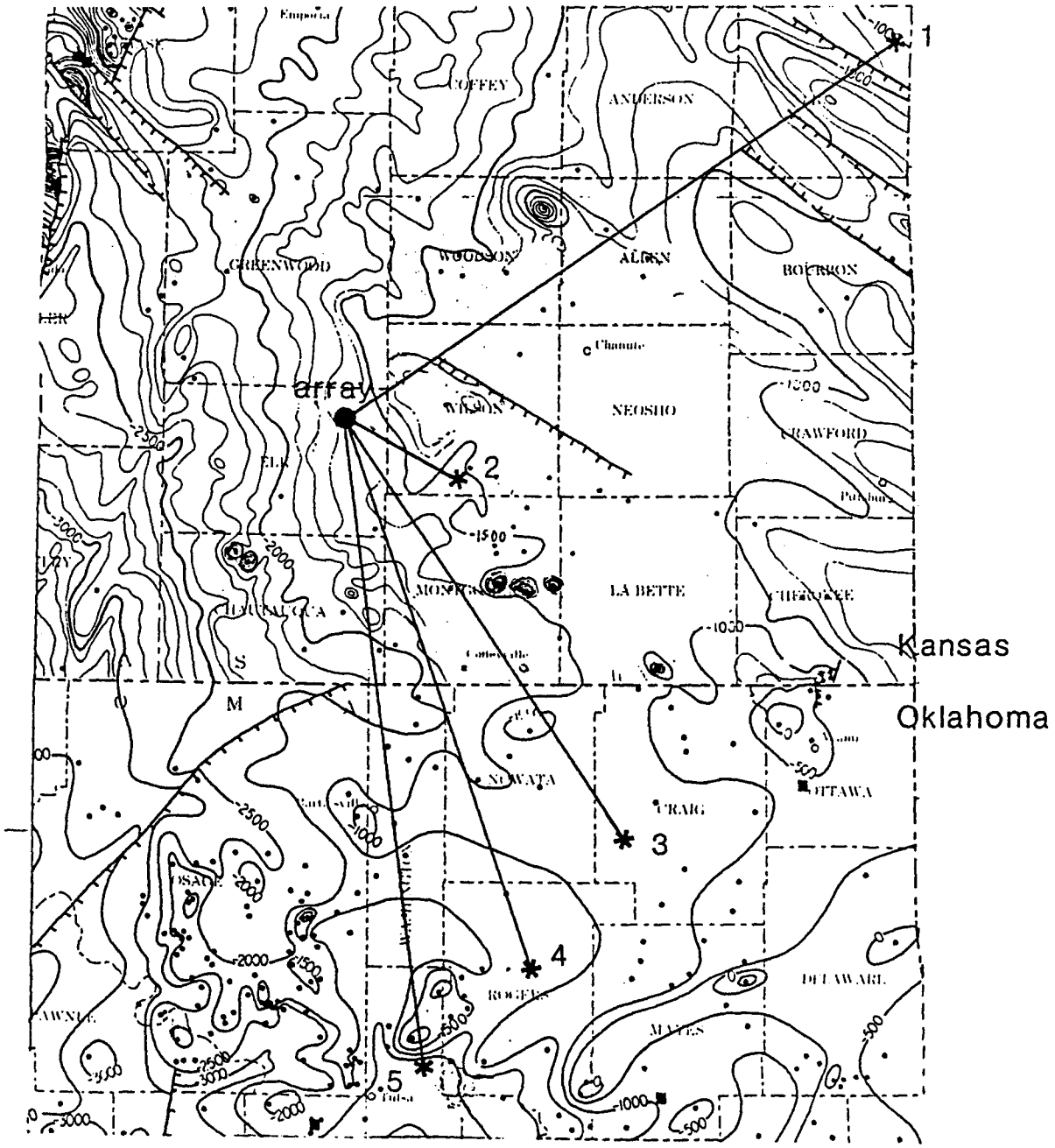

Figure 20. Locations of the events and the array superimposed on a map of Precambrian basement topography (modified from Burchett et al., 1983).

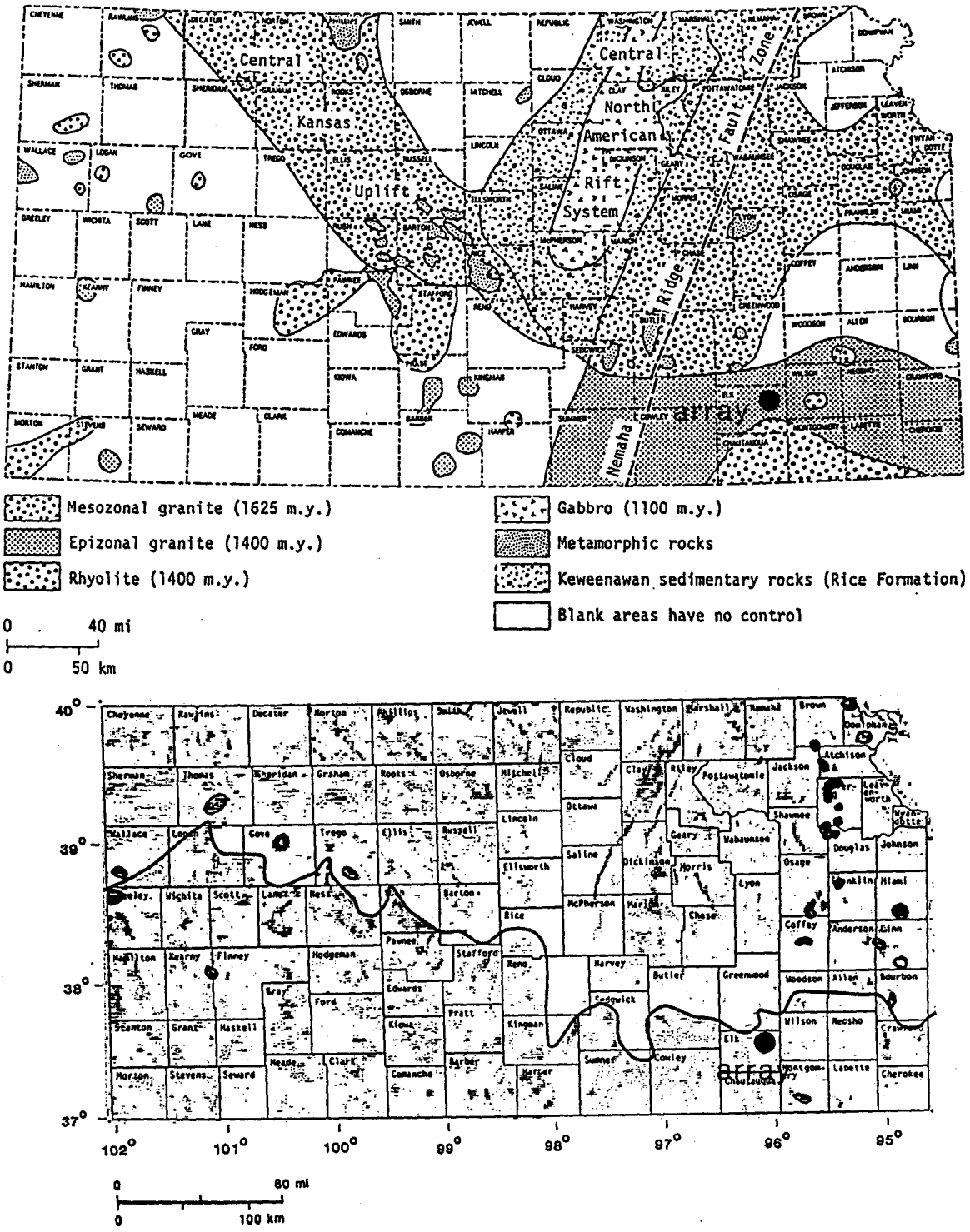

Figure 21. Top: a map of Precambrian rock types in Kansas (after Bickford et al., 1981); Bottom: Aeromagnetic map of Kansas showing the speculated boundary between basement types (after Yarger, 1983).

ROTATION OF HORIZONTAL COMPONENTS

To observe radial and transverse components of a seismic event, it is necessary to rotate the north-south and east-west components through the angle from which the event arrives (the back-azimuth). North-south and east-west digital acceleration records can be expressed as the vector sum of the radial and transverse components:

$$X(n) = R(n)\cos\phi - T(n)\sin\phi,$$
$$Y(n) = R(n)\sin\phi + T(n)\cos\phi, \tag{7}$$

where $X(n)$ is the digital accelerogram recorded by the north-south seismometer, $Y(n)$ is the digital accelerogram recorded by the east-west seismometer, $R(n)$ is the radial digital accelerogram, $T(n)$ is the transverse digital accelerogram, and ϕ is the back-azimuth from which the seismic energy arrives. Solving for $R(n)$ and $T(n)$:

$$R(n) = X(n)\cos\phi + Y(n)\sin\phi,$$
$$T(n) = Y(n)\cos\phi - X(n)\cos\phi, \tag{8}$$

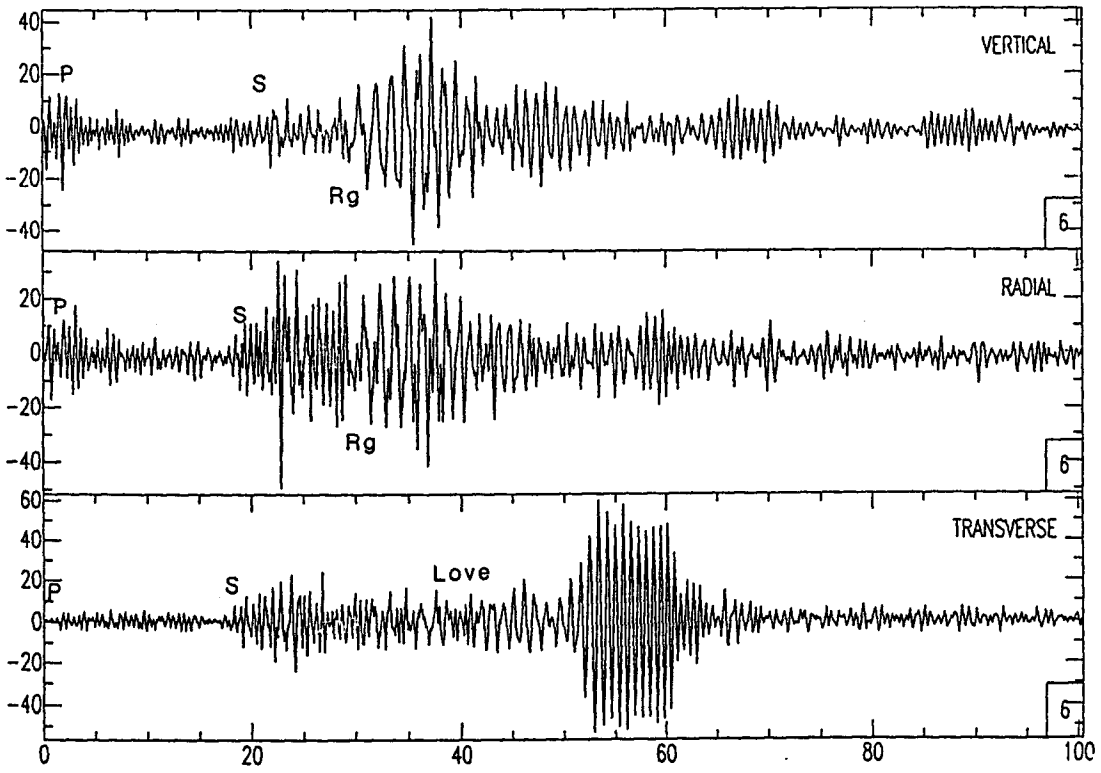

Figure 22. Vertical, radial and transverse accelerograms for event 1. A two Hz lowpass filter has been applied to accentuate the surface-wave trains.

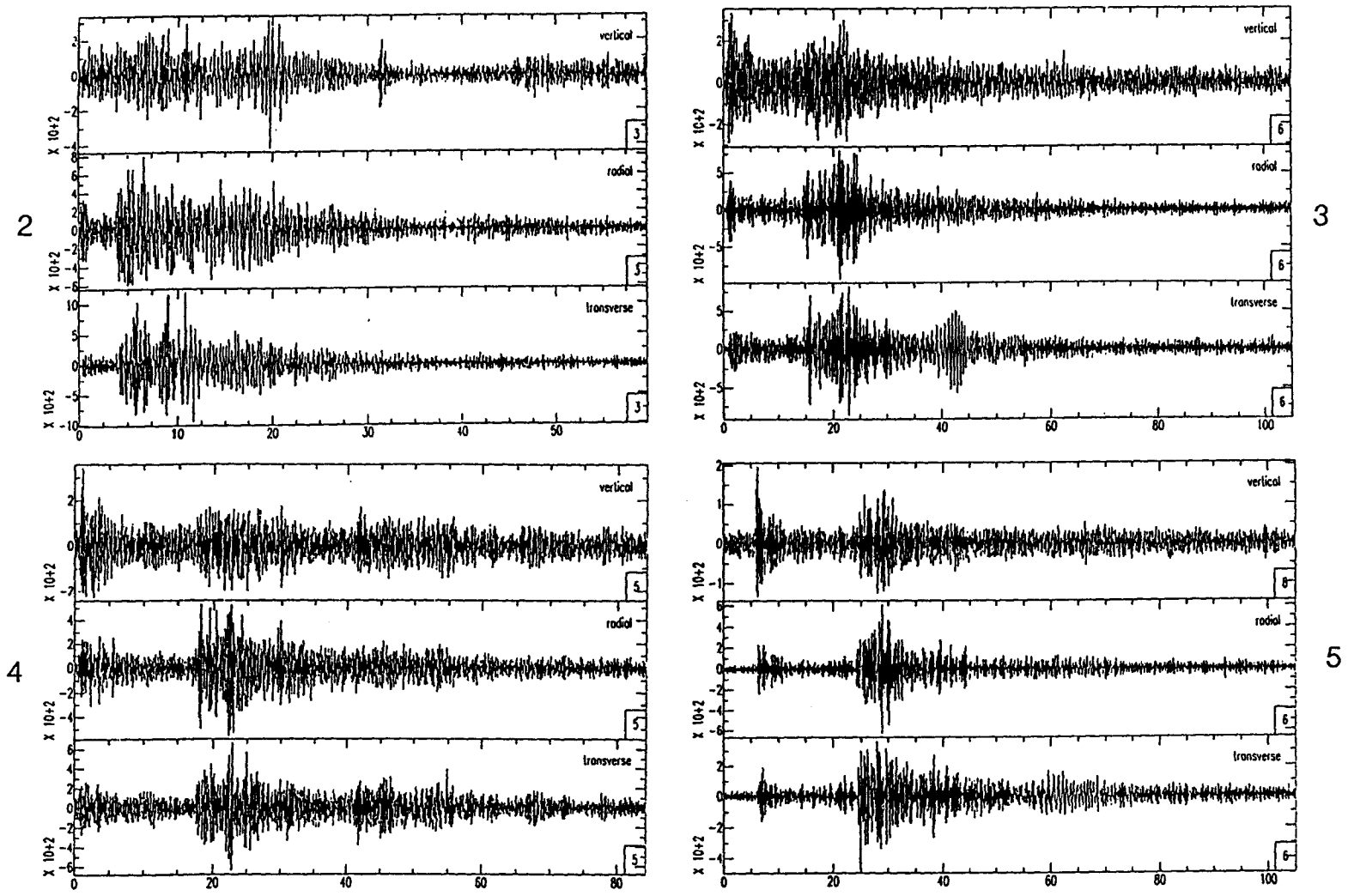

Figure 23. Vertical, radial and transverse accelerograms from events 2-5.

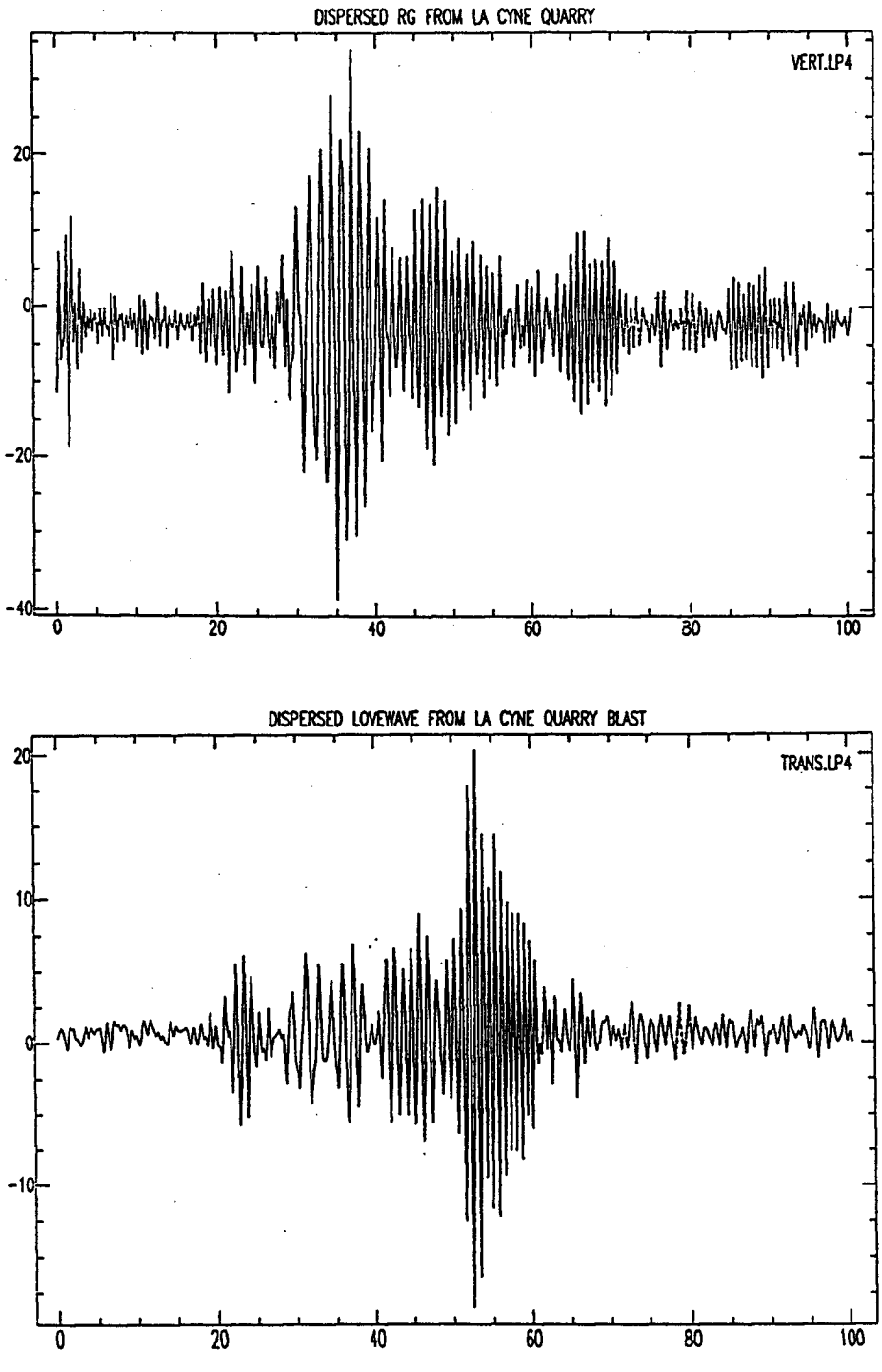

Figure 24. Rg and Love-wave phases for event 1. Rg has a 1.5 Hz lowpass filter applied and the Love wave has a 1.1 Hz low pass filter applied.

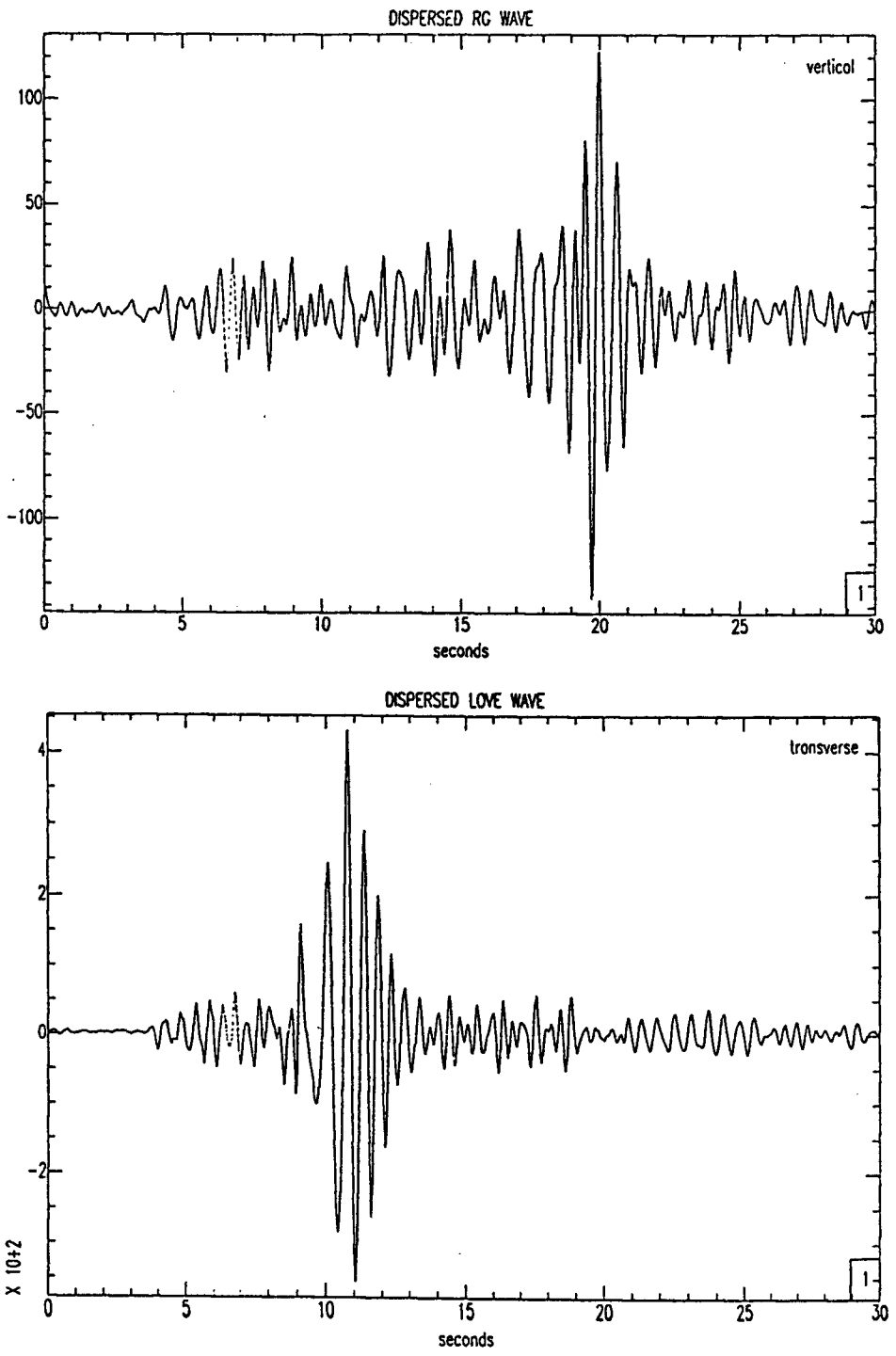

Figure 25. Rg and Love-wave phases for event 2. Both phases have a 2.0 Hz lowpass filter applied.

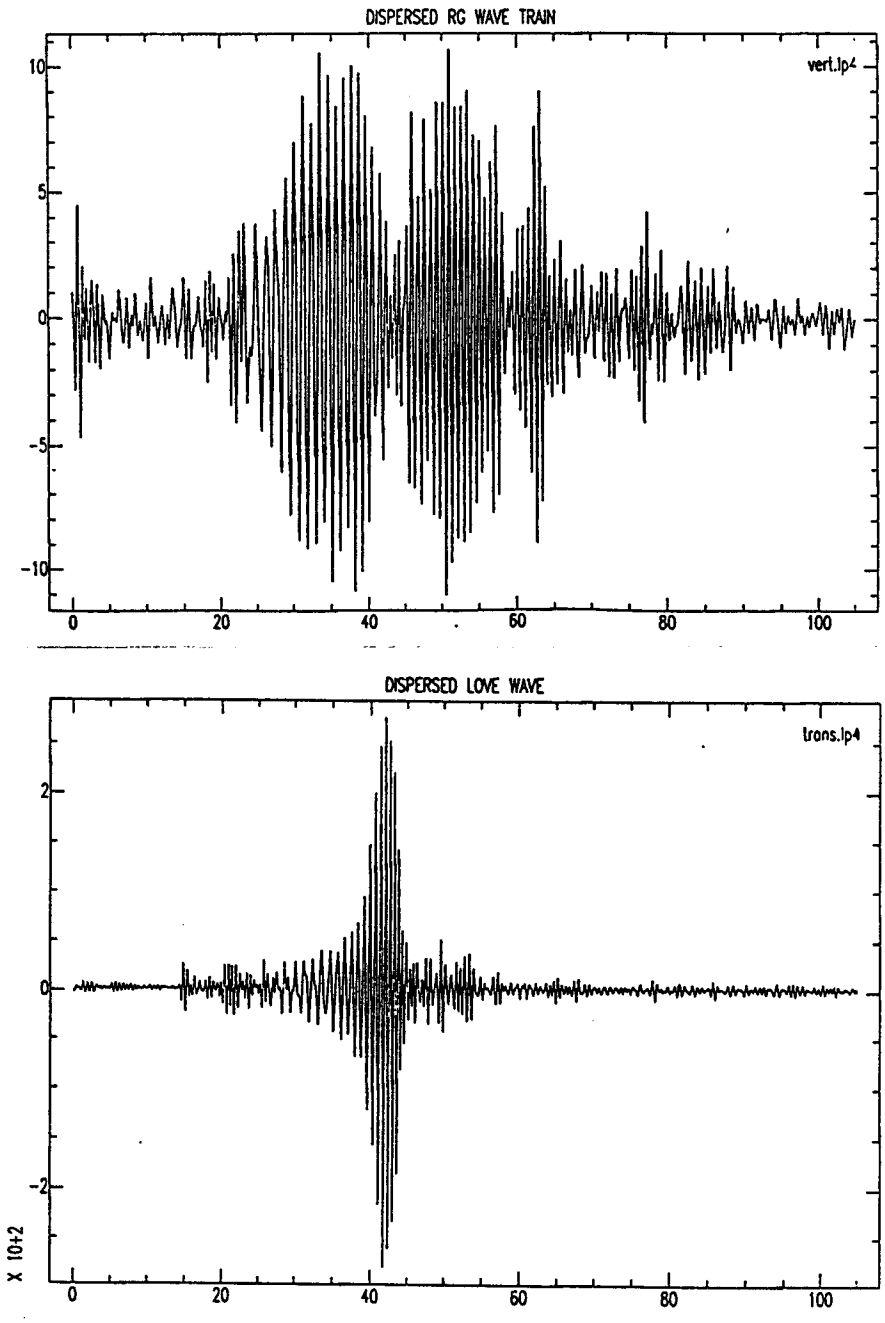

Figure 26. Rg and Love-wave phases for event 3. Both phases have a 1.5 Hz lowpass filter applied.

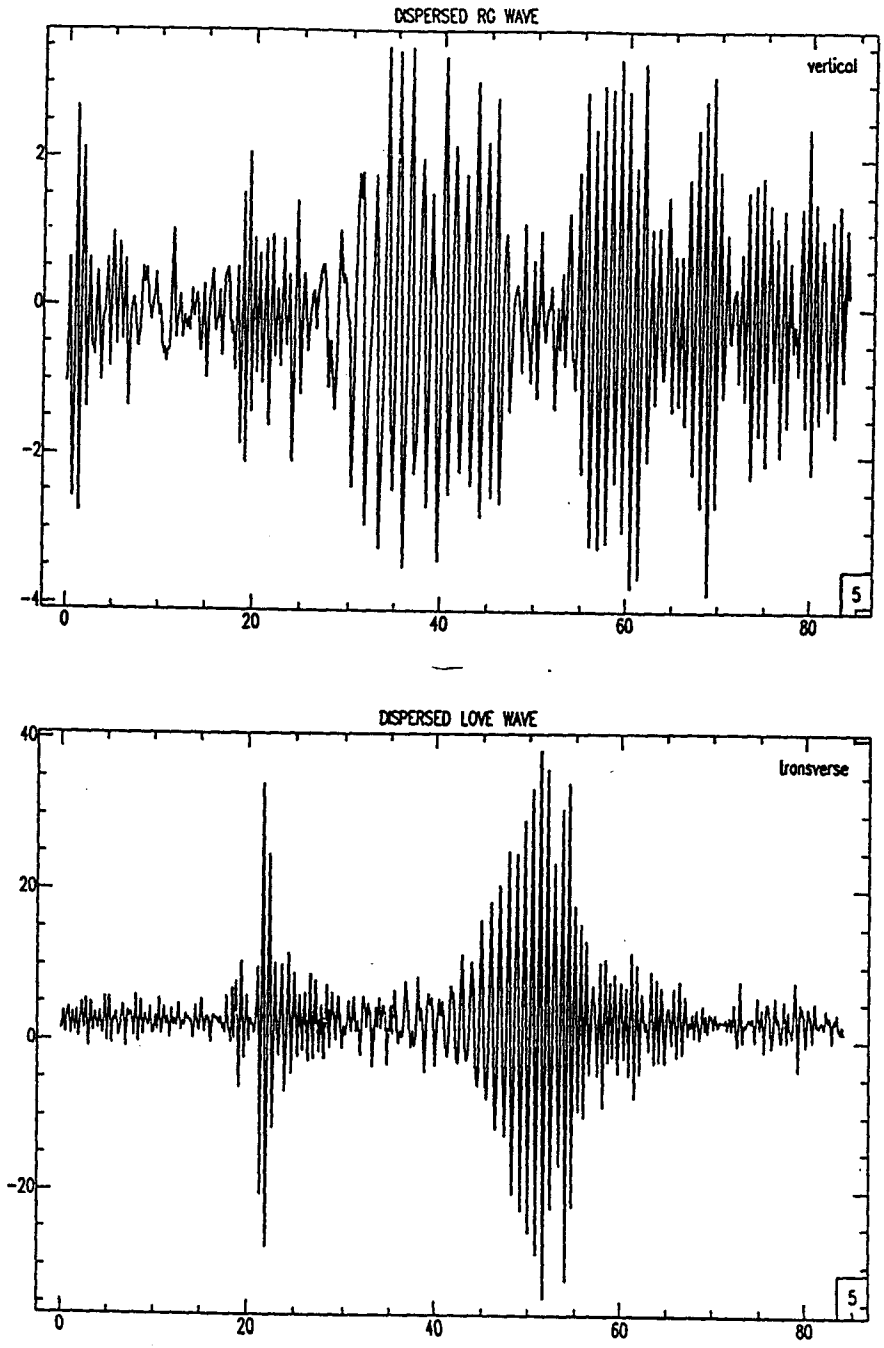

Figure 27. Rg and Love-wave phases for event 4. Both phases have a 2.0 Hz lowpass filter applied.

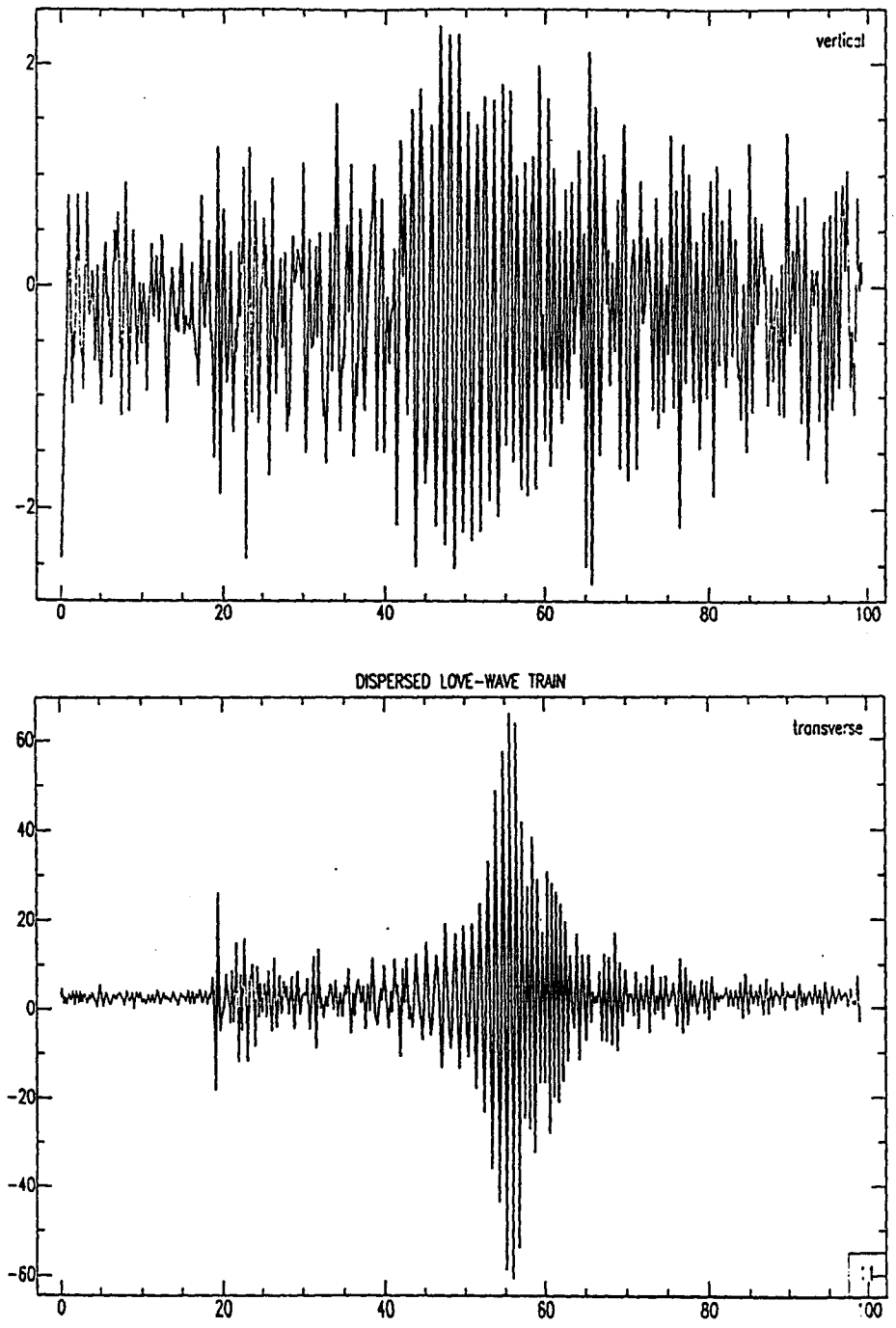

Figure 28. Rg and Love-wave phases for event 5. Both phases have a 1.5 Hz lowpass filter applied.

Therefore, with knowledge of the back-azimuth, data recorded on two perpendicular, horizontal-component instruments can be resolved into transverse and radial components.

The five events exhibiting an Rg phase were rotated into their radial and transverse components using the back-azimuths determined from the power spectra of the Rg phases. Figure 22 shows the vertical, radial and transverse accelerograms for event 1 and Figure 23 shows the three-component data for events 2 through 5. Upon rotation of the horizontal components, a dispersed, short-period, Love-wave phase became apparent (seen on the transverse component for events 1-5 on Figures 22 and 23). Figures 24-28 are plots of the Rg and Love-wave phases recorded at the center station of the array (station 1), filtered to accentuate the dispersion.

LOCATIONS OF EVENTS

Events were initially located by using P and S-wave arrival times measured from accelerograms at the array and from seismograms recorded at stations in Kansas and Oklahoma. Approximate azimuthal constraint was added by the back-azimuth estimates that were determined for the

P-wave and Rg phases. Events 1, 2, 3 and 5 were then identified as mining explosions, detonated at or near the surface, and the locations were verified by mine operators or by personnel at the Geological Survey of Oklahoma. Thus, the locations for these four events were fixed. Event 4 was not traced to a particular mine or quarry, but is presumed to have been a mining explosion detonated at or near the surface. The location based on the measured P and S-wave times was used as the final location for event 4, but group-velocity results derived from this event should be considered less accurate than those from the other four events, and subsequent velocity models are not as reliable for this event as for the others. Actual origin times of the explosions were unknown for all of the events. Table 3 lists the location of each explosion, the distance from the center of the array, and the true back-azimuth for each of the five events.

TABLE 3

Event Locations

Event No.	Location		Distance (km)	Back-az
	Lat N	Long W		
1	38.31	94.63	156.0	58°
2	37.51	95.81	29.6	103°
3	36.61	95.38	119.7	145°
4	36.42	95.85	135.4	161°
5	36.21	95.85	152.6	170°

DETERMINATION OF ORIGIN TIMES

To calculate group-velocity dispersion curves as accurately as possible, it is necessary to obtain accurate origin times for the seismic energy sources. For this study, actual origin times were not available, so it was necessary to estimate the origin times from the P and S-wave arrival times at the center station of the array. This can be done using two basic travel-time formulas:

$$t_p = t_o + x/v_p, \tag{9}$$

$$t_s = t_o + x/v_s, \tag{10}$$

where t_p and t_s are the P-wave and S-wave arrival times as measured from the acceleration records, x is the distance between the source and the center station of the array, v_p and v_s are the average P and S-wave velocities respectively, and t_o is the origin time of the seismic energy source. Through algebraic manipulation:

$$t_o = (t_s - (v_p/v_s)\,t_p)/(1 - (v_p/v_s)). \tag{11}$$

The total travel-time (T) of the P-wave from the source to the array center is given by:

$$T = t_p - t_o. \tag{12}$$

Combining Equations 11 and 12 and manipulating:

$$T = (t_s - t_p)/((v_p/v_s) - 1). \tag{13}$$

The local value of v_p/v_s was determined by regressing P-wave and S-wave arrival times for earthquakes. A value of $v_p/v_s = 1.74$ has been found using earthquakes in the region (Steeples, personal communication) and this value was used in Equation 13. The P and S-wave arrival times are measured from the three-component, digital accelerograms (Figures 22 and 23) to within .01 seconds and are listed in Table 4 along with the origin times and P-wave travel times determined using Equations 11 and 13. The P-wave travel-time is significant because the program that determines group-velocity dispersion operates on the signal from the onset of the P-wave, thus, the travel time prior to the P-wave arrival is needed to determine group velocities.

There are three major sources of error in the determination of the P-wave travel-times (and therefore

the group velocities of the dispersed surface-waves). These timing errors will be greatest for the earliest-arriving surface-waves (longest periods) and will decrease for the later-arriving shorter periods:

1) An error in the determination of t_p and t_s. The error in picking the P-wave and S-wave arrival times on the acceleration records is estimated to be about ± 0.05 seconds. The error in group velocity ranges from about ± 0.01 km/s for long periods, to about ± 0.002 km/s (virtually no error) for short periods.

2) An error in the estimation of the v_p/v_s ratio. As previously mentioned, when regressing P and S-wave arrival times from earthquakes in the region, an average value for v_p/v_s of 1.74 is found. There is some scatter in the data, and the v_p/v_s ratio may lie anywhere in the range from 1.70 to 1.78. This uncertainty amounts to an error in group velocity of ± 0.05 km/s at long periods, to ± 0.01 km/s at short periods.

3) An error is introduced by the fact that the surface-waves did not appear to follow straight-line paths between the sources and the array. A ten degree bearing anomaly gives a P-wave travel time that is approximately

2% low. This results in a maximum error in group velocity of -0.05 km/s for long periods, to -0.01 km/s for short periods.

Added together, the possible error in group velocities ranges from +0.06 km/s to -0.11 km/s for long periods and +0.01 km/s to -0.02 km/s for short periods. These possible errors will be considered following the inversion.

TABLE 4

Travel Time Information

Ev. No.	Date	Hour:min.	t_p	t_s	t_o	T (sec)
1	8-1-86	19:32	37.44	55.97	12.72	25.04
2	3-27-87	19:48	47.67	51.46	42.55	5.12
3	3-26-87	19:17	24.25	38.36	5.19	19.06
4	3-27-87	16:15	09.35	26.17	-13.37	22.72
5	3-26-87	21:29	03.20	21.42	-21.45	24.65

t_p = P-wave arrival time (seconds).

t_s = S-wave arrival time (seconds).

t_o = event origin time (seconds).

T = time from origin to onset of P-wave at station.

DETERMINATION OF GROUP-VELOCITY DISPERSION

Group velocities were determined by using multiple-filter analysis, introduced by Dziewonski et. al., (1969) as a method of analyzing variations of amplitude of a signal as a function of velocity (time) and period (frequency). The multiple-filter technique recovers broader portions of the dispersion present in a seismic signal, than the classical peak-and-trough method (Dziewonski et. al., 1969).

Initially, time series data containing dispersed surface-wave data is transformed, via the Fourier transform into the frequency domain:

$$F(\omega) = \int_{-\infty}^{\infty} f(t)\exp(-i\omega t)\,dt, \qquad (14)$$

where $f(t)$ is the time series data and $F(\omega)$ is the frequency domain data. In general $F(\omega)$ is a complex quantity:

$$F(\omega) = R(\omega) + iI(\omega) \qquad (15)$$

where $R(\omega)$ and $I(\omega)$ are the real and imaginary parts of $F(\omega)$. A series of one hundred bandpass filters are then convolved with the frequency data. These bandpass

filters are centered on frequencies evenly spaced between the specified upper and lower limits of analysis. This convolution is a windowing process in the frequency domain:

$$H_n(\omega) = G(\omega - \omega_n)\, F(\omega), \tag{16}$$

where $G(\omega - \omega_n)$ is a symmetrical bandpass filter centered on ω_n and $H_n(\omega)$ is the windowed frequency data for each center frequency.

The choices of the shape and the width of the window function are important to consider. For this study, a Gaussian-type function was chosen as the window function, because the frequency-time resolution is greater for a Gaussian than for any other type of function. In this case, the Gaussian is considered to be equivalent to an optimum-filter function (Dziewonski et al., 1969). The Gaussian-window function, $G_n(\omega)$ is expressed as:

$$\begin{cases} 0 & ;\text{for } \omega < (1-B)\omega_n \\ \exp(-\alpha((\omega/\omega_n)-1)^2) & ;\text{for } (1-B)\omega_n < \omega < (1+B)\omega_n \\ 0 & ;\text{for } \omega > (1+B)\omega_n \end{cases} \tag{17}$$

where B is the chosen bandwidth and $\propto$ is a falloff function that depends on the bandwidth. The bandwidth of the window is a variable. A narrow bandwidth has good frequency resolution, but poor time resolution. A broad window has poor frequency resolution and good time resolution. The appropriate bandwidth lies somewhere in between and is generally chosen by trial and error.

The result of the windowing at each center frequency is then transformed into the time domain, via the inverse Fourier transform:

$$h_n(t) = \int_{-\infty}^{\infty} H_n(\omega)\exp(i\omega t)\,d\omega, \qquad (18)$$

where $h_n(t)$ is the resulting time series. Figure 29 shows the result of this process, operating upon the Rg phase from event 1 (Figure 24), for a single center frequency. The data were windowed with a fairly broad, Butterworth-type (Sheriff, 1984) bandpass filter (instead of the aforementioned Gaussian), centered at 0.6 Hertz. The result, as shown in Figure 29, is a plot of an envelope superimposed on a nearly monochromatic, 0.6 Hertz sine-wave. The time of the maximum of the envelope is the group-arrival time of seismic energy in the 0.6 Hertz range.

Equation 18 gives only the in-phase, filtered signal for each ω_n (Dziewonski et al., 1969). Knowledge of the quadrature time function is required to evaluate the instantaneous amplitude, which is the construction of the envelope shown in Figure 24. The quadrature spectrum is found from the in-phase spectra by introducing a 90-degree phase shift:

$$Q_n(\omega) = H_n(\omega)\exp(i\pi/2)) \tag{19}$$

where $Q_n(\omega)$ is the quadrature spectrum for each individual center frequency. The quadrature time function $q_n(t)$ is obtained through use of the inverse Fourier transform:

$$q_n(t) = \int_{-\infty}^{\infty} Q_n(t)\exp(i\omega t)\, d\omega. \tag{20}$$

The instantaneous amplitude $A_n(t)$ is then given by:

$$A_n(t) = (h_n(t)^2 + q_n(t)^2)^{1/2}. \tag{21}$$

The time at which the instantaneous amplitude is a maximum is the group-arrival time of the seismic energy in the ω_n range and can be measured directly. This process was repeated for an array of 100 ω_n values, and

a corresponding group-arrival time was determined for each one of these values. The group- arrival times were converted to group velocities with the additional knowledge of the P-wave travel-time from the source to the array (T from Table 4) and the distance between the source and the array (x from Table 3):

$$U_n = x/(Y_n + T) \tag{22}$$

Here Y_n are the group-arrival times (relative to the P-wave arrival) as determined by the multiple-filter method.

A basic procedure was followed for determining the group-velocity dispersion for the Rg and Love-wave phases for each of the five events:

1) Vertical and transverse-component records of the events, recorded at station 1, were place in separate files.

2) Data were resampled (and concurrently lowpass filtered to avoid aliasing) from 120 samples per second to 10 samples per second.

3) Amplitude spectra for the 0-5 Hertz range were calculated and visually inspected for each component, to estimate the high and low-frequency limits for the multiple-filter analysis (Figure 30).

4) The multiple-filter-analysis program was run on the vertical-component data (Rg) with the high and low frequency limits (Hertz), filter bandwidth (Hertz), P-wave travel time (seconds) and the distance from the source (kilometers) as the input parameters.

5) The program was run on the transverse component data (Love wave).

Program output is a plot of the group velocity for individual periods of the surface-wave. Figure 31 is a plot of group-velocity dispersion for the Rg and Love-wave phases from event 1, determined using multiple-filter analysis. Figure 32 shows group dispersion of both surface-wave phases for events 2 and 3 and Figure 33 shows the same for events 4 and 5. A filter bandwidth of .1 Hertz was generally found to give the widest range of frequencies and was used for both phases of all five events.

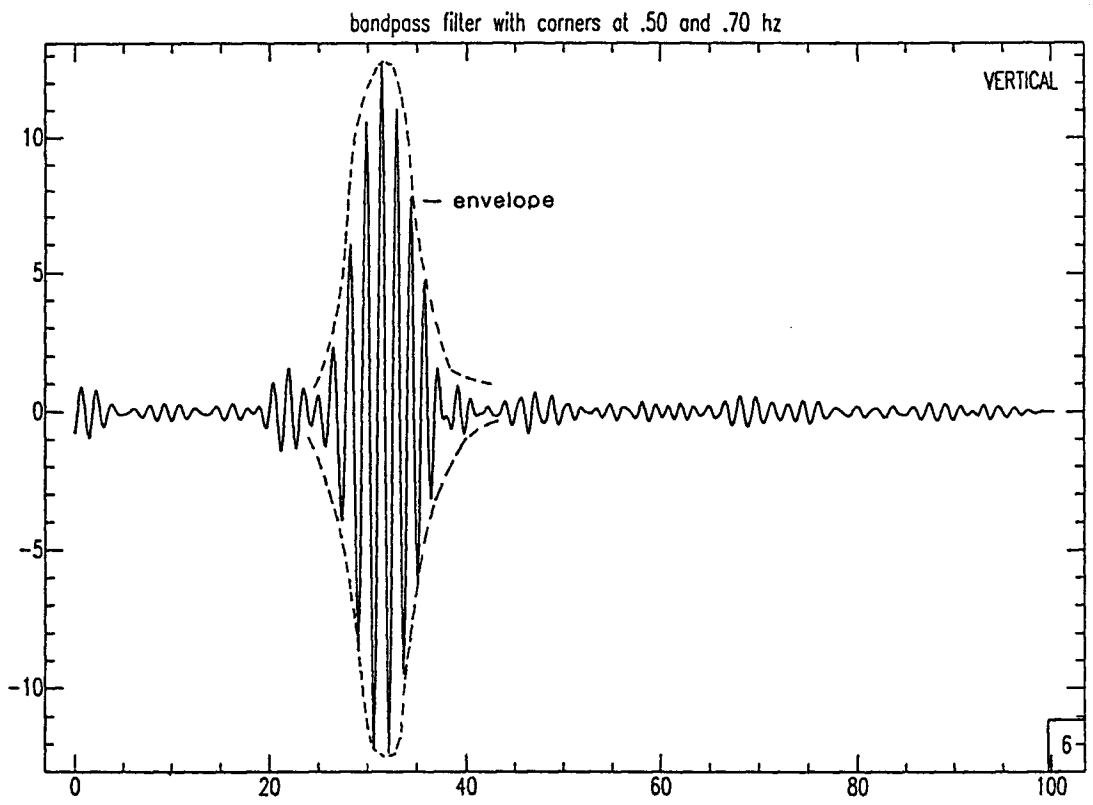

Figure 29. Result of convolution of the Rg phase from event 1 with a Butterworth-type bandpass filter, centered at 0.6 Hz. Note that the peak of the envelope is the group-arrival time of Rayleigh-wave energy in the 0.6 Hz range.

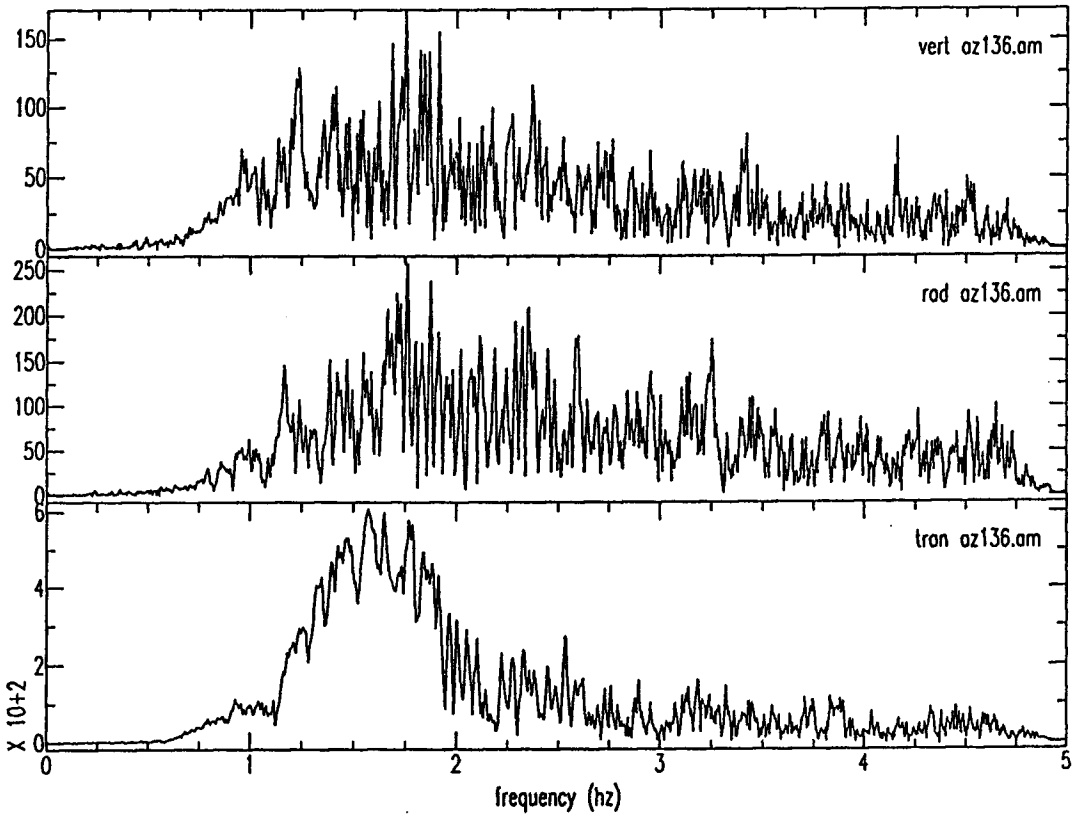

Figure 30. Spectra for the vertical, radial and transverse components of the signal from event 3, recorded at station 1. Note the strong peak in the 1-2 Hz range on the transverse component. This is the spectrum of the Love-wave phase.

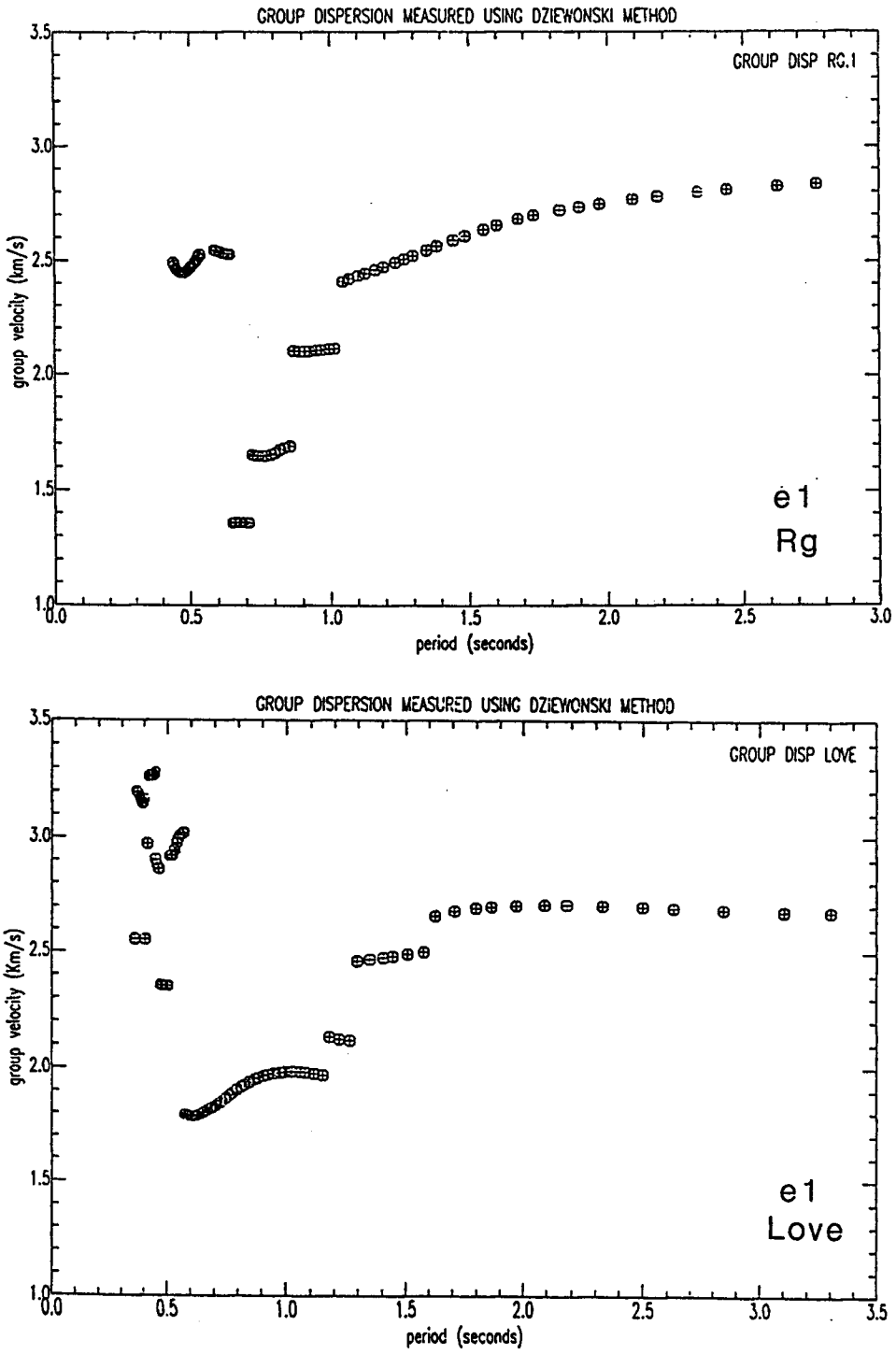

Figure 31. Group-velocity dispersion for event 1.

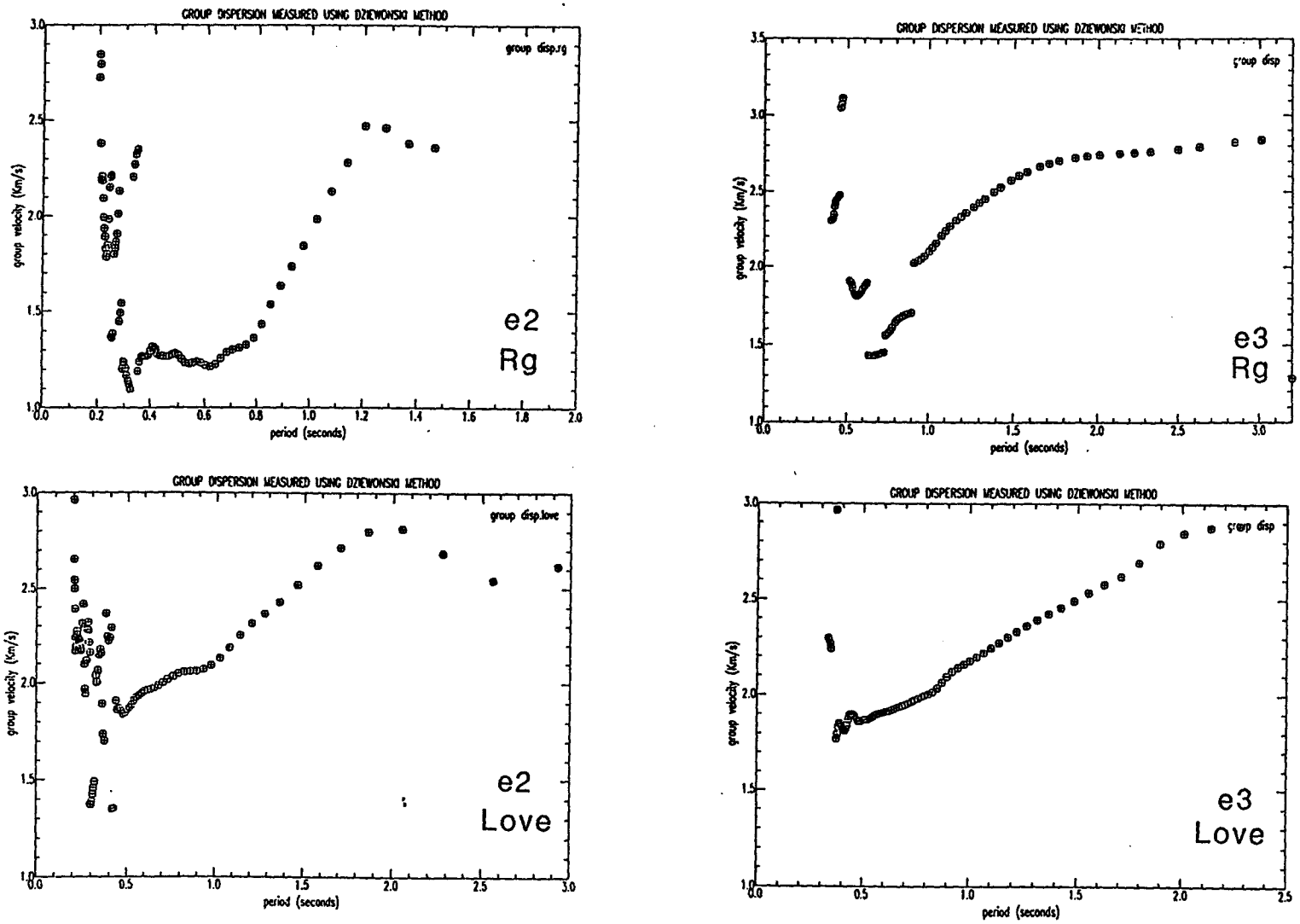

Figure 32. Group-velocity dispersion for events 2 and 3.

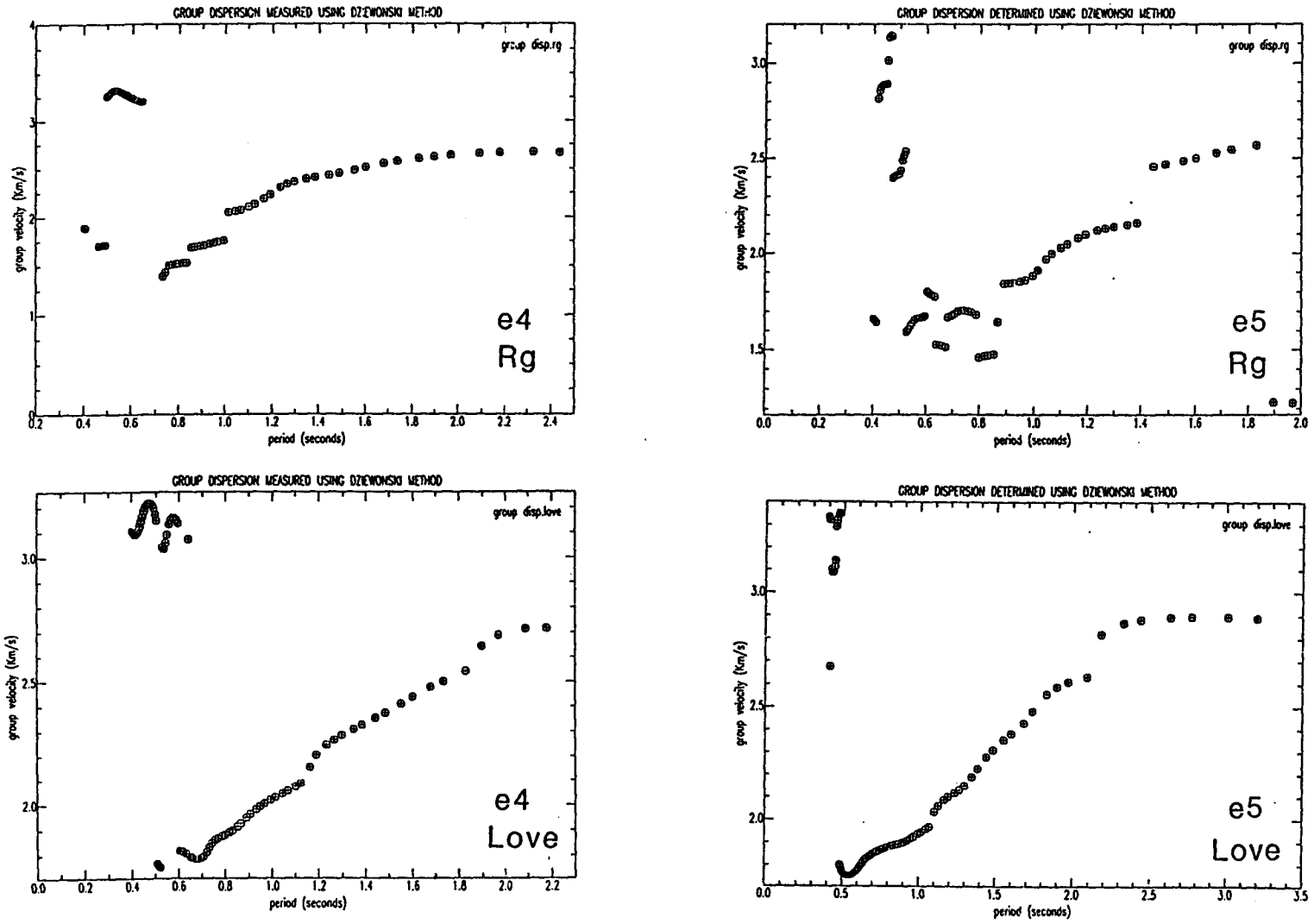

Figure 33. Group-velocity dispersion for events 4 and 5.

REMOVAL OF INSTRUMENT DELAY

The response curve for an S-13 seismometer is given, in terms of the group delay as a function of frequency (Figure 34). Also shown is the cumulative delay attributed to the electronics present at each site. The group delay is the time delay introduced by the various instruments and is determined from the Fourier phase, $\theta(\omega)$ of the instrument response:

$$t_{gr}(\omega) = d(\theta(\omega))/d\omega, \tag{23}$$

where $t_{gr}(\omega)$ is the group delay. The delay was removed from the recorded data by subtracting the group delay due to the instruments from the group-arrival times measured using multiple-filter analysis.

ANALYSIS OF MEASURED DISPERSION

From analysis of the measured group-velocity dispersion (Figures 31-33) several general observations can be made:

1) The Rg and fundamental-mode, Love-wave dispersion curves are clearly seen from their respective dispersion

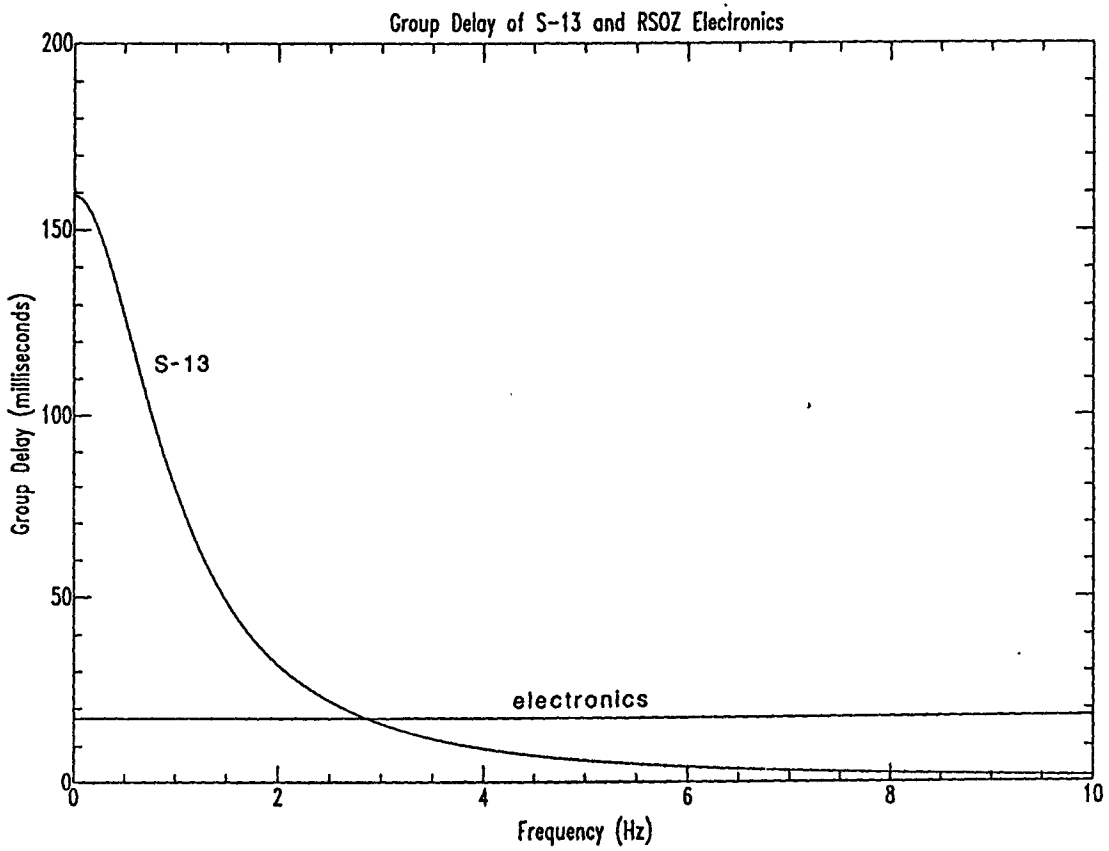

Figure 34. Plot of group delay for the seismometers and the combined electronics.

plots. The Rg phases lie in the period range of 0.6 to 3.1 seconds and the fundamental-mode, Love-wave phases lie in the range of 0.5 to 3.2 seconds.

2) All of the measured fundamental-mode dispersion curves have a disjointed appearance. This phenomenon appears to be due to multipathing effects. Multipath arrivals are laterally refracted or reflected surface-wave trains that follow different paths and therefore arrive behind the direct surface-wave arrival. The effects of multipath arrivals on surface-wave trains and the measured dispersion curves are referred to as multipathing effects. Multipathing is discussed in the following chapter. The Rg dispersion curves appear to be more severely disjointed than do the Love-wave curves.

3) Energy at periods below those of the fundamental-modes is due either to shear waves, or higher-mode surface-waves. This energy typically arrives with velocities between 2.5 and 3.5 km/s. Some of this energy appears to be dispersed, which would indicate that it is due to higher-mode surface-waves. Once the inversion is completed, the suspected higher-mode energy

can be compared to theoretical, higher-mode dispersion curves generated from the resulting models.

4) Both Rg and fundamental-mode, Love-wave dispersion curves appear to asymptotically approach a velocity of 3.0 km/s as the period increases. At periods greater than 2.2 seconds, Love-wave group velocities appear to be too low. This is probably due to the fact that most of the energy in the Love waves is concentrated in the latter parts of the wave trains (Figure 26 for example). The long-period components of the Love waves have extremely low amplitudes. With such low amplitudes, it is difficult to accurately determine group-arrival times. Group velocities from the Rg phases are not affected because the amplitudes at long periods are sufficient to determine accurate group-arrival times (Figure 26). During the inversion process, Love-wave group velocities above 2.2 seconds are not used as a constraint.

5) The shapes of the Rg dispersion curves are similar for all five of the events, but the curves are displaced with respect to each other in the period-group velocity plane. The group-velocity minima are at velocities of

about 1.3 km/s. Figure 35 shows a cumulative plot of all the Rg dispersion curves.

6) The shapes of the fundamental-mode, Love-wave dispersion curves are also very similar for each of the five events. These curves are also displaced with respect to each other. The group-velocity minima for the Love waves have velocities of about 1.8 km/s. Figure 35 shows a cumulative plot of all the fundamental-mode, Love-wave dispersion curves.

7) The Rg phases have extended wave trains because there is a broad range of velocities covered by the dispersion (1.3 to 2.9 km/s). The fundamental-mode, Love-wave phases have relatively short wave trains because the range of velocities covered is somewhat smaller than those of the Rg phases (1.8 to 2.9 km/s).

8) Fundamental-mode dispersion curves from event 2 have a slightly different range of periods than the other events (Rg; 0.4 to 1.2 seconds, Love wave; 0.5 to 2.1 seconds). The difference in the range of periods is due to the proximity of the source to the array (29.6 km). Since the distance that surface waves from event 2 travels is small, the seismic energy suffers relatively

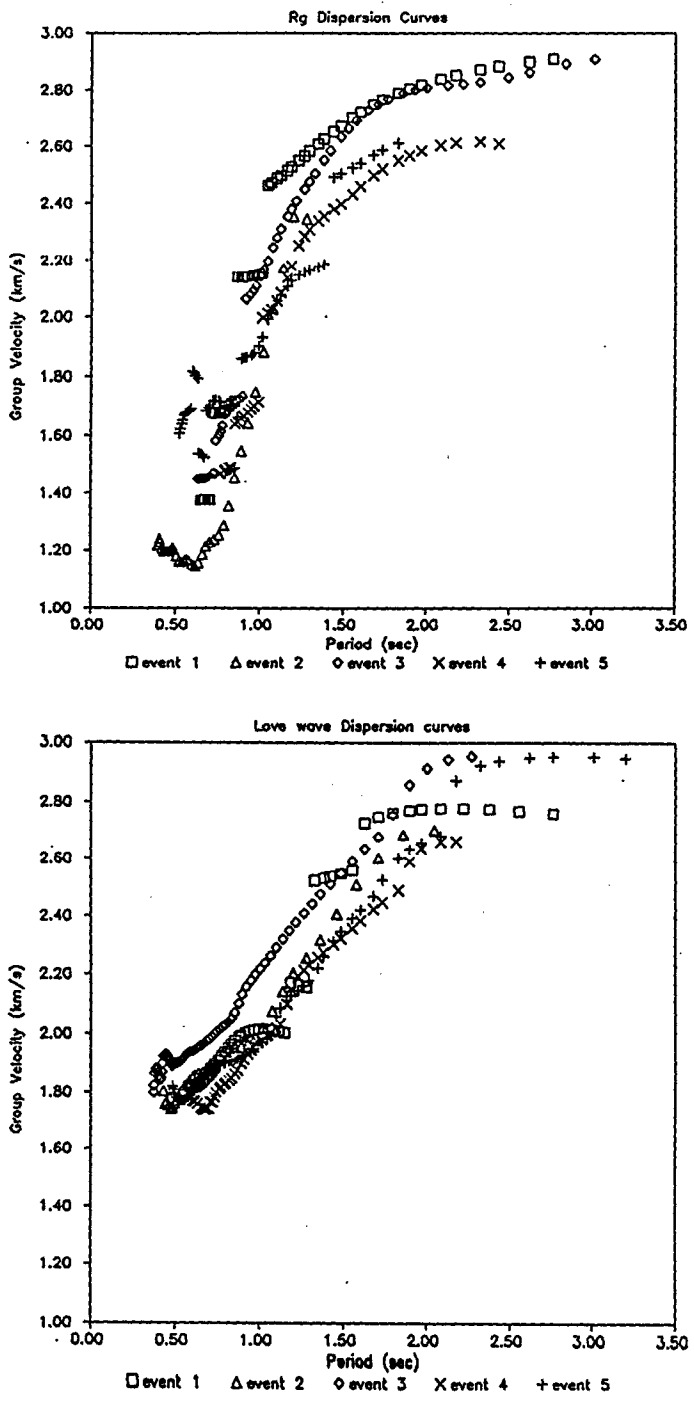

Figure 35. Composite plots of the Rg and Love-wave dispersion curves.

less attenuation than events originating from significantly greater distances (see Table 3). As a result of the lower attenuation, there is lower-period energy present in the dispersed Rg and Love-wave phases. This additional short-period energy is important because it contains information about the shallow velocity structure to which the other events are not as sensitive.

EFFECTS OF MULTIPATHING

As previously mentioned, the fundamental-mode dispersion curves suffer from being somewhat discontinuous. This makes comparisons with theoretical dispersion curves (for the purpose of inverting for seismic velocity structure) difficult. This problem may be the consequence of secondary surface-wave arrivals that act to interfere destructively with the primary surface-wave train. Secondary arrivals are referred to as multipath arrivals because they follow paths different than that followed by the primary surface-wave train (they may be laterally refracted or reflected). The problem is severe in some cases (Rg from event 1), minor in other cases (Love wave from event 5), and non-existent in one particular case (both phases for event

2). The effects of multipathing on surface-wave trains and their measured dispersion curves can be examined qualitatively, using synthetic surface-wave seismograms.

Synthetic, short-period, surface-wave records, genetically similar to those that are recorded in the study region can be produced quite simply. As previously stated (Equation 23), the group-arrival times, as a function of frequency, can be determined by differentiation of the Fourier phase spectrum. Conversely, integration of the group-arrival curve produces the Fourier phase spectrum:

$$\theta(\omega_1) = \int_o^{\omega_1} t_{ga}(\omega)\, d\omega, \qquad (24)$$

where $t_{ga}(\omega)$ is the measured group-arrival curve. To generate a synthetic, fundamental-mode, Rg wave train, the group-arrival times of the Rg phase from event 1 were approximated by a polynomial function (Figure 36). The polynomial was integrated to arrive at the synthetic phase spectrum. The synthetic amplitude spectrum was chosen so that the frequency content of the synthetic seismogram was similar to that of the actual Rg phase for the event. For this purpose a Butterworth-type bandpass filter with corners at 0.6 and 1.2 hertz was chosen (Figure 37). This type of filter has a flat

frequency response between the chosen corners and falls off rapidly outside of these corners. The real and imaginary frequency domain components were calculated from the synthetic amplitude and phase spectra and transformed into the time domain via the inverse Fourier transform. The result of the inverse transform is the synthetic, surface-wave seismogram shown as the top trace of Figure 38.

A surface-wave train that is contaminated with a multipath arrival was simulated by duplicating the original synthetic wave-train, multiplying the duplicate wave train by a factor of .5, time-delaying by 5 seconds, and adding the original and duplicate seismograms together. The result of this is shown as the bottom trace of Figure 38. This simulates a primary surface-wave arrival, followed 5 seconds later by a similar surface-wave train with an amplitude one-half that of the primary wave train. Note the modulated appearance of the synthetic multipathed trace, as well as the Rg phase from event 1 (Figure 24). This modulated effect is observed in many of the surface-wave records (Figures 24-28). The occurrence of modulation effects in the synthetic seismogram, as well as in the real data, helps confirm the idea of the real data being contaminated with one or more multipath arrivals.

The synthetic seismograms were subjected to multiple-filter analysis to observe what effects multipathing has on the group-velocity dispersion curves. Multiple-filter analysis of the uncontaminated synthetic trace (top trace, Figure 38) returned the original polynomial function, band-limited by the chosen Butterworth bandpass filter. Multiple-filter analysis of the multipathed synthetic trace (bottom trace, Figure 38), generated a group-velocity dispersion curve that was highly discontinuous (Figure 39). A comparison of Figure 39 with the Rg dispersion curve from event 1 (Figure 31) shows that the two curves have a similar appearance. Both curves are smooth at long periods, but become discontinuous at shorter periods. The similarity between the dispersion curves of the real and synthetic data indicates that multipathing is most likely responsible for the discontinuous structure of the dispersion curves at short periods.

Two important results are derived from this modeling. The first is that the disjointed appearance of the measured dispersion curves does appear to be due to multipath-propagation effects. The second is that the effects of the multipathing can be accounted for when inverting the dispersion curves for seismic velocity structure. Figure 39 shows the dispersion

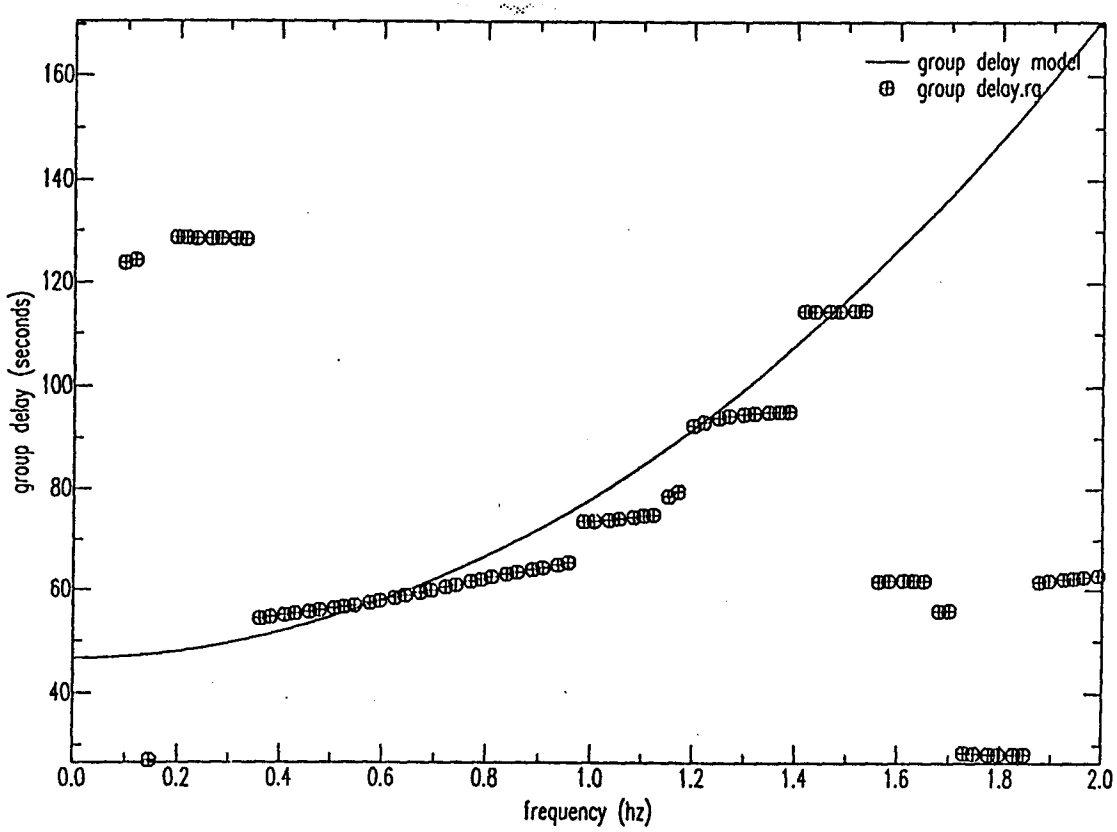

Figure 36. Approximation by a second-order polynomial for the group delay of the Rg phase from event 1.

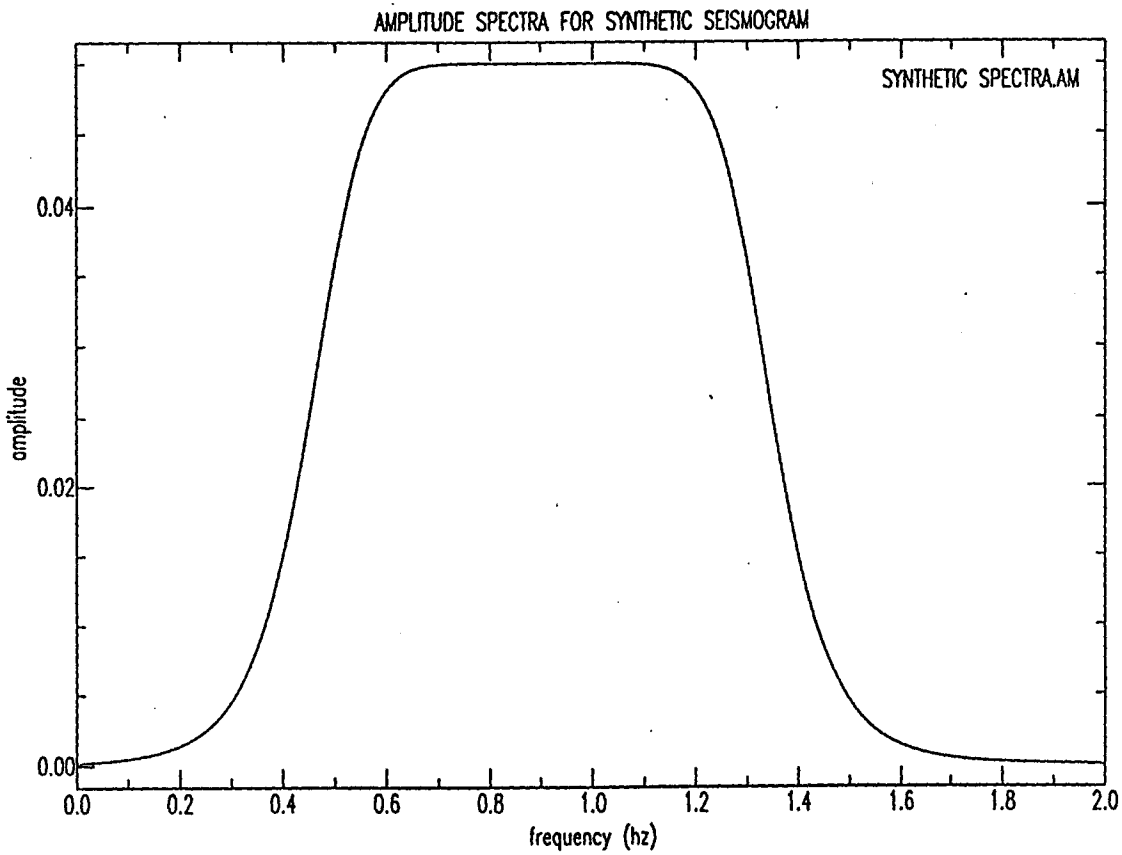

Figure 37. Butterworth-type Bandpass filter, centered at 0.9 Hz, with corners at 0.6 Hz and 1.2 Hz.

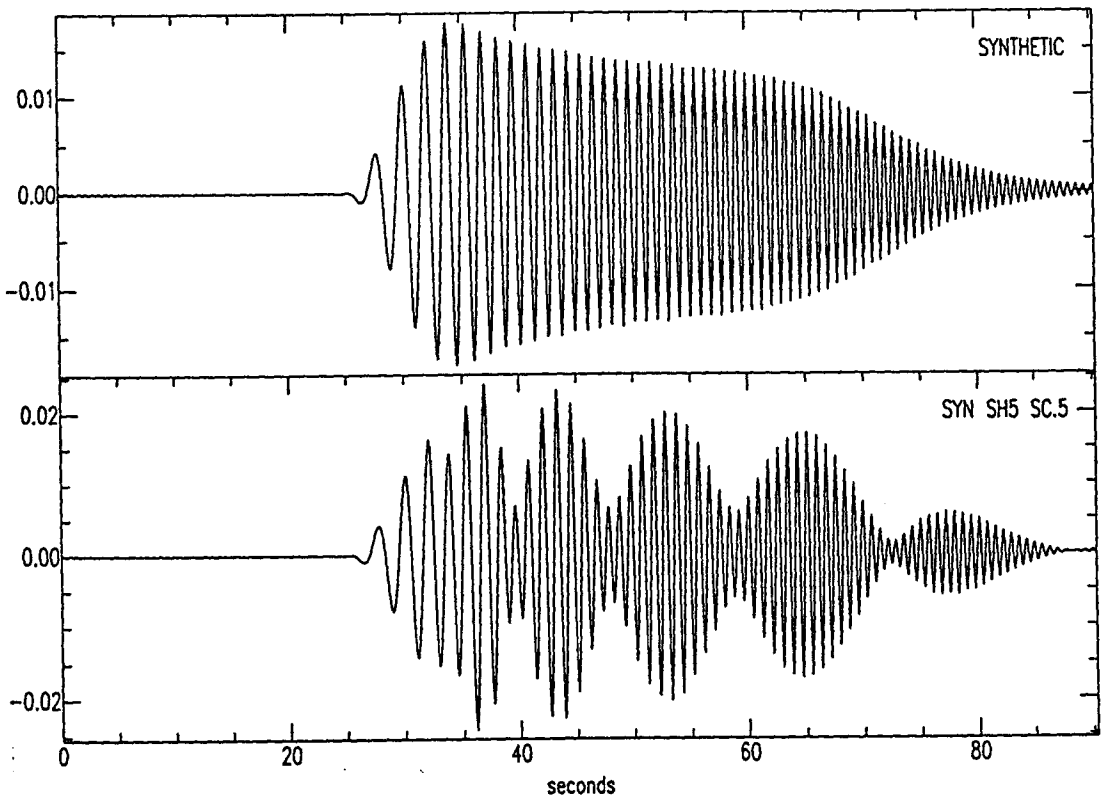

Figure 38. Synthetic surface-wave seismograms. Top: single surface-wave train; Bottom: Synthetic multipath seismogram.

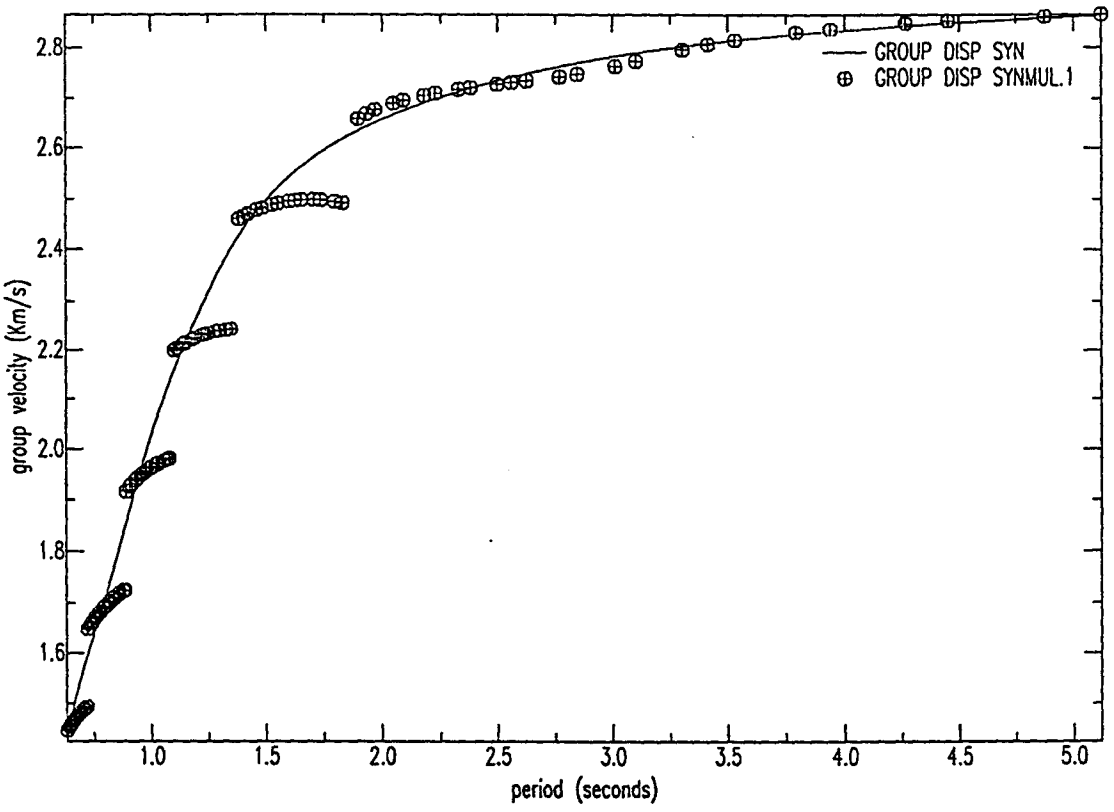

Figure 39. Group-velocity dispersion for an uncontaminated surface-wave train (shown by the line) and for a multipathed surface-wave train (shown by the crossed circles).

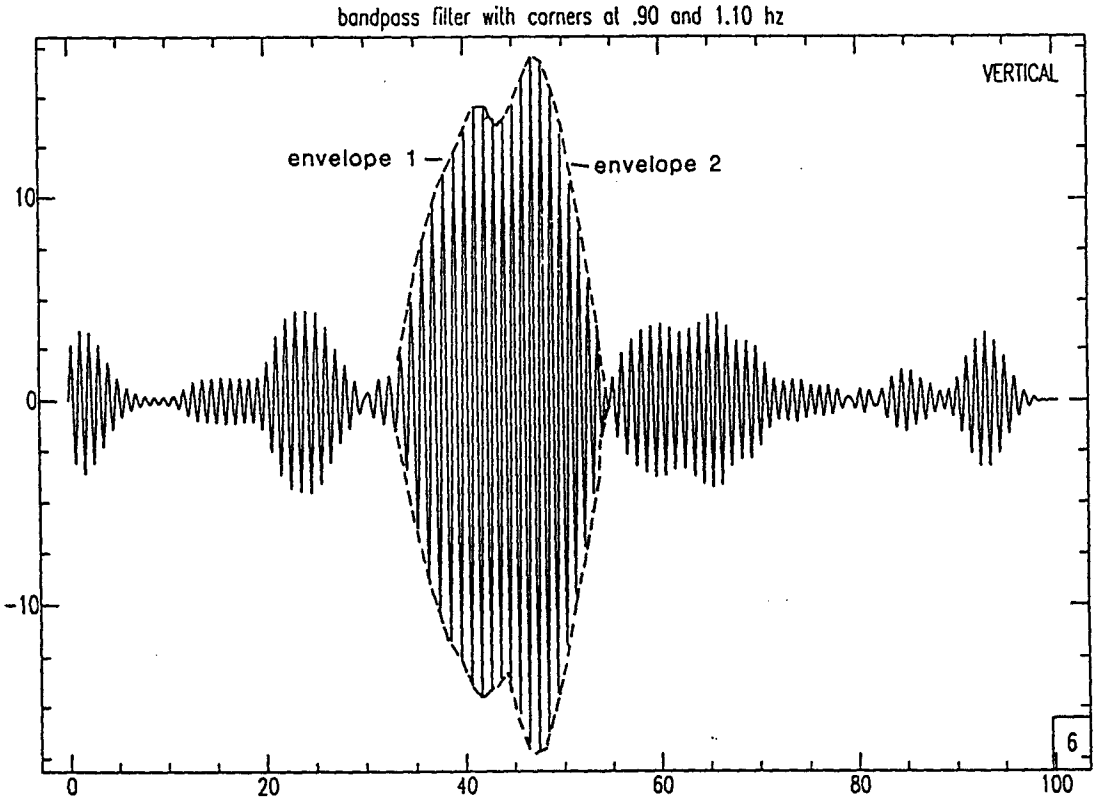

Figure 40. Result of convolution between Rg phase from event 1 and a Butterworth-type bandpass filter centered at 1 Hz. Note that there are two amplitude envelopes in close proximity. Envelope 1 is Rayleigh-wave energy in the 1 Hz range from the primary Rg arrival. Envelope 2 is Rayleigh-wave energy in the 1 Hz range for a multipath arrival.

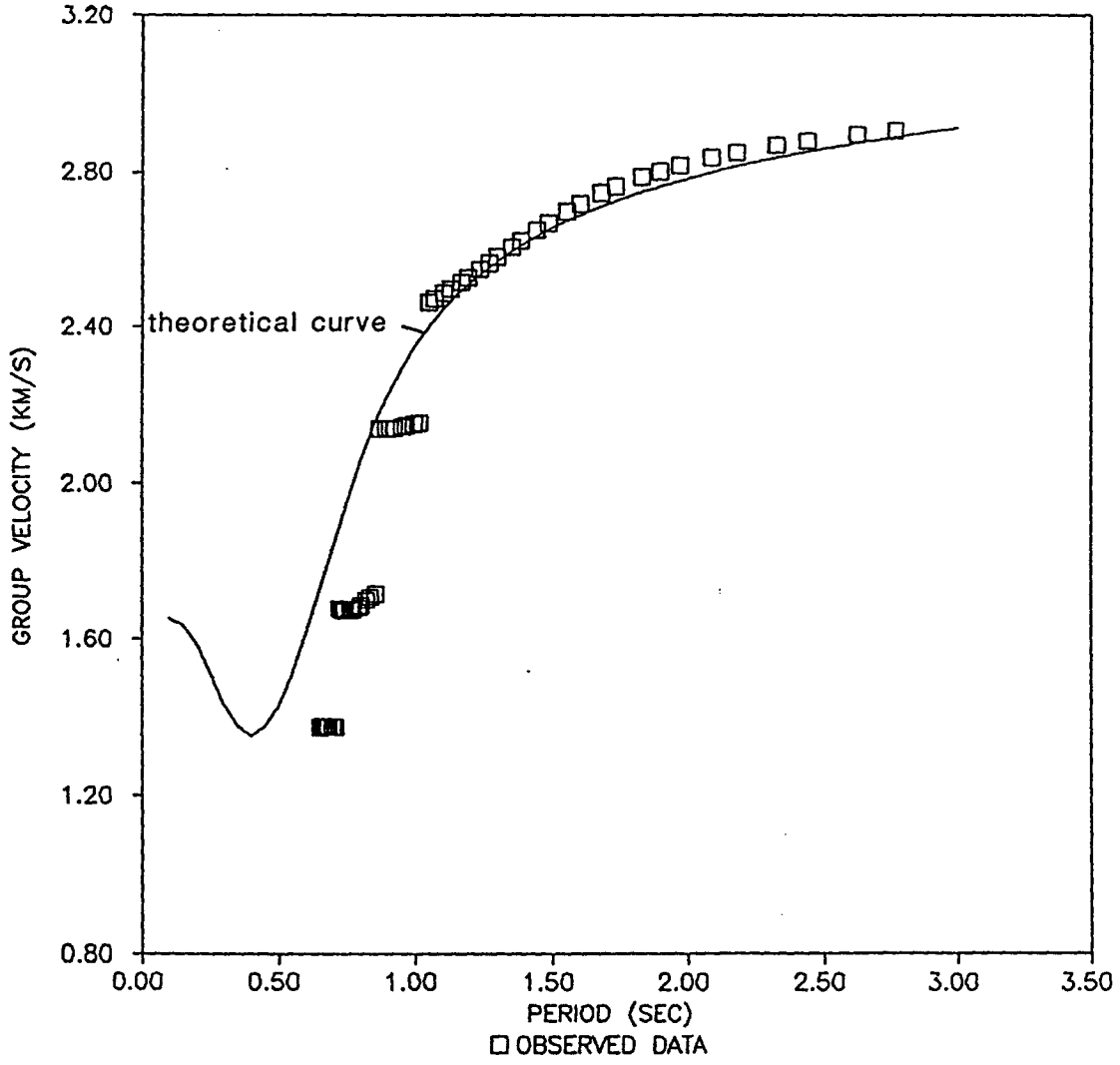

Figure 41. A comparison of observed Rg group velocities and a theoretical Rg group-dispersion curve. Note that at short periods, the theoretical dispersion-curve has higher group velocities than the observed data.

curve for the multipathed synthetic trace, as well as the dispersion curve for the uncontaminated synthetic trace. Note that the disjointed segments of the multipathed curve follow the trend of the uncontaminated curve. Also note that the segments of the multipathed curve are shifted just to the right of the uncontaminated curve. A shift occurs because energy from multipath arrivals at the same periods as the primary serve to broaden the instantaneous-amplitude envelope and shift the peak of the envelope towards greater group-arrival times (Figure 40). The shift in the peak of the instantaneous amplitude reduces group velocity values. The contaminated dispersion curves can be compared to theoretical dispersion curves, with the knowledge that the theoretical curves should follow the same trend as the contaminated curves, but will be shifted slightly upwards in group velocity along the contaminated portions of the curve (Figure 41).

INVERSION OF OBSERVED DISPERSION DATA

The process of determining a physical model which may have given rise to a set of observations is known as inverse modeling or inversion. In this study, an upper-crustal velocity model which gives rise to the observed

Rg and Love-wave dispersion was sought. The inversion was facilitated by comparing the observed Rg and Love-wave dispersion curves with theoretical Rayleigh and Love-wave dispersion curves, generated for various velocity models of the upper crust. An inversion is complete when theoretical dispersion data from some model matches the observed dispersion data as closely as possible. The theoretical dispersion curves (fundamental and higher modes) were generated by computer programs that use theory put forward by Thompson (1950) and Haskell (1953) and applied to Rayleigh and Love waves by Harkrider (1970). The programs compute the phase and group-velocity dispersion, as a function of period for flat-lying, multilayered media, overlying an isotropic half-space.

During the inverse modeling process, it is important to consider if a particular interpretation is unique. In most cases, a given dispersion curve can be interpreted in terms of more than one structure. If dispersion curves are available for both Rayleigh waves and Love waves, the number of structural interpretations that will fit both dispersion curves will be limited (Bath, 1971). The number of interpretations can be further reduced, if higher-mode dispersion data (for Rayleigh and/or Love waves) are available.

The physical parameters that control the character of Rayleigh-wave dispersion are: (1) the number of layers present; (2) the thickness of each layer; (3) the P-wave velocity, S-wave velocity, and density of each individual layer and the half-space. With the exception of P-wave velocity, the character of Love-wave dispersion is dependent on the same parameters that control the Rayleigh-wave dispersion. Knowledge of the values of these parameters that can be gleaned from previous geophysical or geological studies can simplify the inversion process, as well as further reduce the number of possible interpretations.

The effect that each parameter has on observed dispersion was investigated prior to the inversion. This was done by approximating the upper-crustal velocity model and perturbing each of the various parameters of the model individually, while holding other parameters constant. The effects of the perturbations on the observed dispersion curves can be seen by plotting variation curves for each of the varied parameters. This analysis is useful in determining which parameters are passive and which are active. Passive parameters are those to which the dispersion curves are insensitive, or in other words, the parameters that cause the dispersion curves to change

very little when the parameter is varied. Active parameters are those that cause the dispersion curves to vary significantly when perturbed. The base model for this sensitivity analysis is shown in Figure 42. The compressional-wave velocities for the Paleozoic sedimentary rocks and the Precambrian basement were based on the results of crustal scale refraction studies in north-central Kansas by Steeples and Miller (1987). The shear-wave velocities were fixed by assuming the v_p/v_s ratio is equal to 1.74 (Steeples, personal communication). The thickness of the Paleozoic section was taken from structure contour maps of the Precambrian basement (Burchett et al., 1983) and topographic maps of southeast Kansas and northeast Oklahoma. The density of the Paleozoic section was estimated from analysis of bulk-density, well-log measurements throughout the region. The Precambrian basement was given a density value of 2.67 g/cc, the value usually assigned to Mid-continent basement rocks in gravity modeling (Woollard, 1969). The variation curves for Rayleigh waves for periods from 0 to 3 seconds are shown in Figures 43 through 46. The Love-wave variation curves for the same period range are shown in Figures 47 through 49. Table 5 lists the abbreviations of the various parameters used in determining the variation curves.

Although the variation curves are based on a crustal model that may not adequately explain the observed dispersion, examination of these curves can lead to a qualitative "feel" for how surface-waves are dispersed at this scale. Analysis of the variation curves leads to a broad understanding of how the dispersion varies as a function of the physical parameters that control the dispersion.

A cursory check of the variation curves indicates that for the Rayleigh waves the passive parameters are P1, RH01, P2, and RH02. Small changes in the values of these parameters causes very little variation in the subsequent dispersion curves. It should be noted that the physical constraints on densities are smaller than the constraints on velocities and thicknesses. The densities of sedimentary rocks typically vary between about 2.3 and 2.7 g/cc (Dobrin, 1976), while seismic velocities have a much wider variance, and thicknesses have no limitations. The active parameters are S1, S2, and the layer thickness. Variation of S1 changes the group-dispersion curves at short periods (Figure 43), particularly by moving the group-velocity minimum up (increasing S1) or down (decreasing S1). At longer periods, the curves remain relatively unchanged. Variation of the layer thickness serves to shift the

group-velocity curves forward or backward in period (Figure 44). Variation of S2 slightly effects the curves at short periods (near the group-velocity minimum) but strongly effects the curves at longer periods, as each curve asymptotically approaches a value of about 0.9 of the varied S2 velocities (Figure 45).

For Love waves, the passive parameters are RH01 and RH02. The active parameters are S1, S2, and layer thickness. Variation of S1 causes an extreme change in the Love-wave dispersion curves for all the periods being investigated (Figure 47). Variation of S2 changes the Love-wave dispersion curves significantly at longer periods and very little at shorter periods (Figure 48). As with Rayleigh waves, variation of the layer thickness serves to shift the Love-wave curves backward or forward in period, with each curve essentially maintaining the same basic shape.

As previously mentioned, Love waves are independent of P-wave velocities. Rayleigh waves in principle are influenced by P-wave velocities. As shown through the variation curves through, the P-wave velocities are passive parameters and therefore Rayleigh waves are relatively insensitive to them. Because of this relative insensitivity to P-wave velocities, most of the results of surface-wave studies are presented as models

of S-wave velocities varying with depth (Garland, 1979). This study follows that convention. P-wave velocities can be related to S-wave velocities by considering the regional v_p/v_s ratio.

The inversion can be simplified through knowledge of the average thickness of the Paleozoic sedimentary section along the five propagation paths. The average thickness was determined from Precambrian-basement structure contour, and topographic maps of the region. Figure 50 shows cross sections of the total Paleozoic sedimentary section and the upper part of the basement for each of the five propagation paths. The cross sections shown have a vertical scale in feet, but the average thicknesses were converted to and are listed in kilometers. Group-velocity dispersion is dependent on the average thickness of the sedimentary layer; consequently, flat layers of constant thickness equal to the average thicknesses shown in Figure 50 were used in the inversion process.

As previously mentioned, the Paleozoic sedimentary section is composed of three major stratigraphic units (Figure 6). The thicknesses of these three units vary throughout the study region. The inversion was facilitated by varying the thicknesses of the three layers within the constraint that the total thickness of

the three must be equal to the known thickness of the total Paleozoic section. Simultaneously, S-wave velocities were varied within each layer and the basement. As with the base model for the sensitivity curves, the density of the Paleozoic section was fixed at 2.6 g/cc and the basement density was fixed at 2.67 g/cc. Since density is a passive parameter, an error in the assigned densities should have virtually no effect on the inversion.

The first step in the inversion process was to establish an initial velocity model. For this study the initial model consisted of three layers overlying a half-space (Figure 51), where h_i is the average thickness of the total Paleozoic section for the *ith* path. The velocities and densities of this model were the same as those shown in Figure 42. Theoretical Rg and Love-wave group-dispersion curves were generated from this model and plotted against the observed, Rg and Love wave group-dispersion data. Differences between the observed and theoretical data were noted and the variation curves were examined to estimate which parameters needed to be changed, and by what amount. The according parameters were changed, producing a new velocity model. From the new velocity model, a new set of theoretical, Rg and Love wave, group-dispersion

curves were generated and compared to the observed data. The differences between the observed and theoretical data should be smaller for the new model than for the initial model. Again, the differences between the observed and theoretical data were noted and the parameters of the model were changed so as to further reduce the differences between the observed and theoretical data. This procedure was repeated until the observed and theoretical data converged to a point where the residuals for both the Rg and the Love-wave curves were minimized.

This iterative, interactive, inversion process was followed for each of the five propagation paths. The final match between the observed and theoretical data for each of the paths is shown in Figures 52 through 56. The velocity models derived for the five paths are shown in Figure 57. Figures 52-56 also include the suspected, higher-mode data, along with theoretical 1st higher-mode, group dispersion curves. These higher-mode curves were generated from the final velocity model. The higher modes were not used as a constraint during the inversion, but rather as a check on the determined velocity model. The suspected higher-mode data may not be particularly well resolved because the data were resampled too severely.

TABLE 5

Definition of Parameters Used In Variation Curves

P1	P-wave velocity of layer
P2	S-wave velocity of layer
RHO1	Density of layer
P2	P-wave velocity of half-space
S2	S-wave velocity of half-space
RHO2	Density of half-space

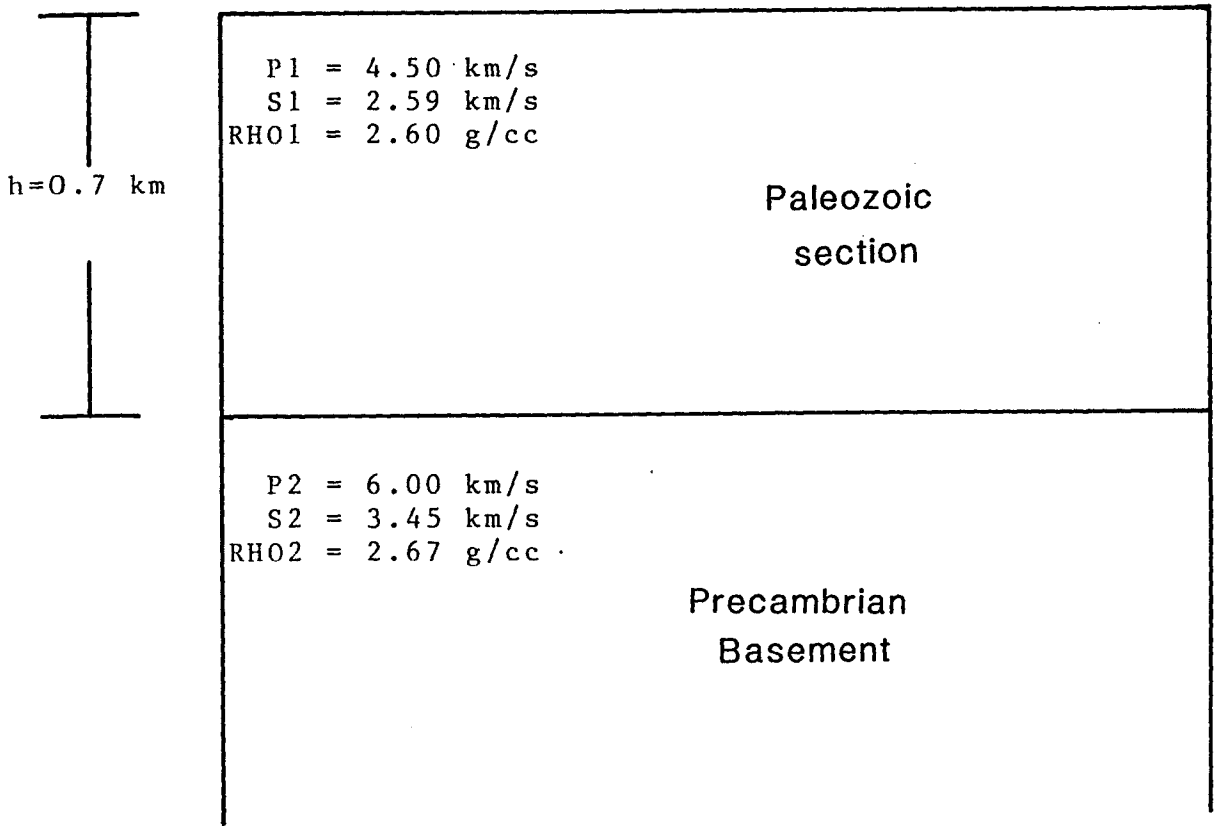

Figure 42. Base velocity model from which the variation curves are generated.

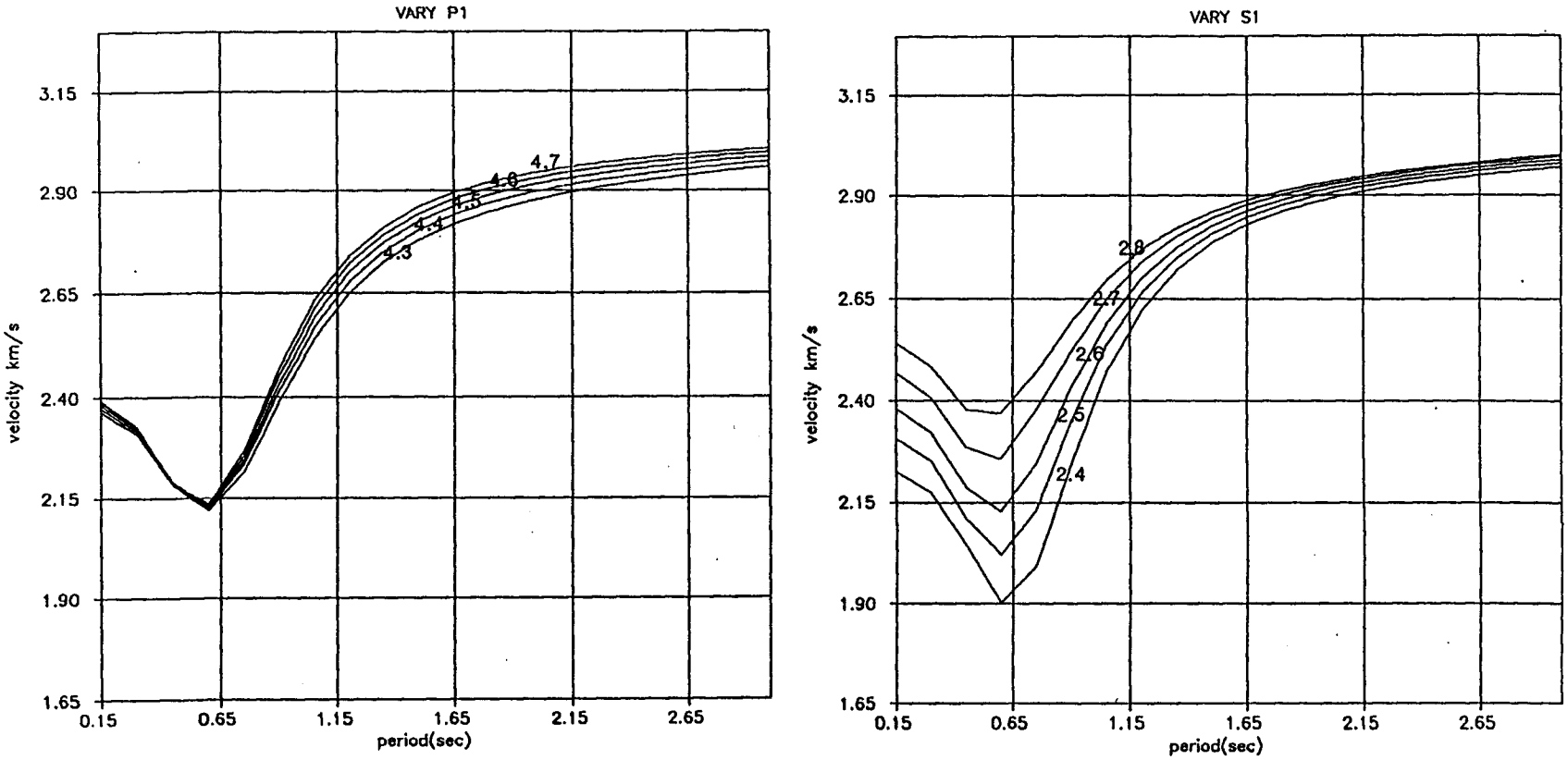

Figure 43. Variation curves for Rayleigh waves.

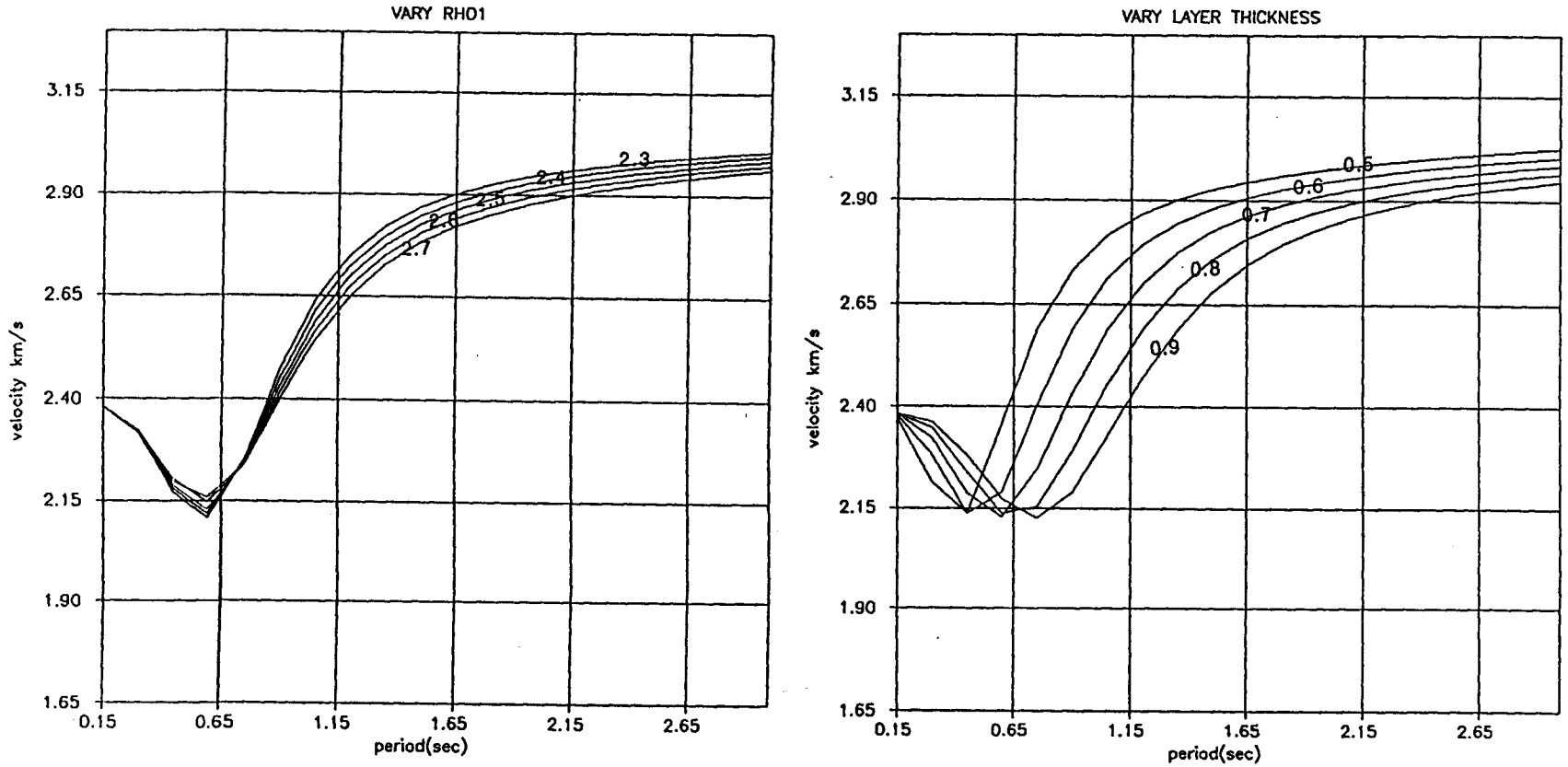

Figure 44. Variation curves for Rayleigh waves.

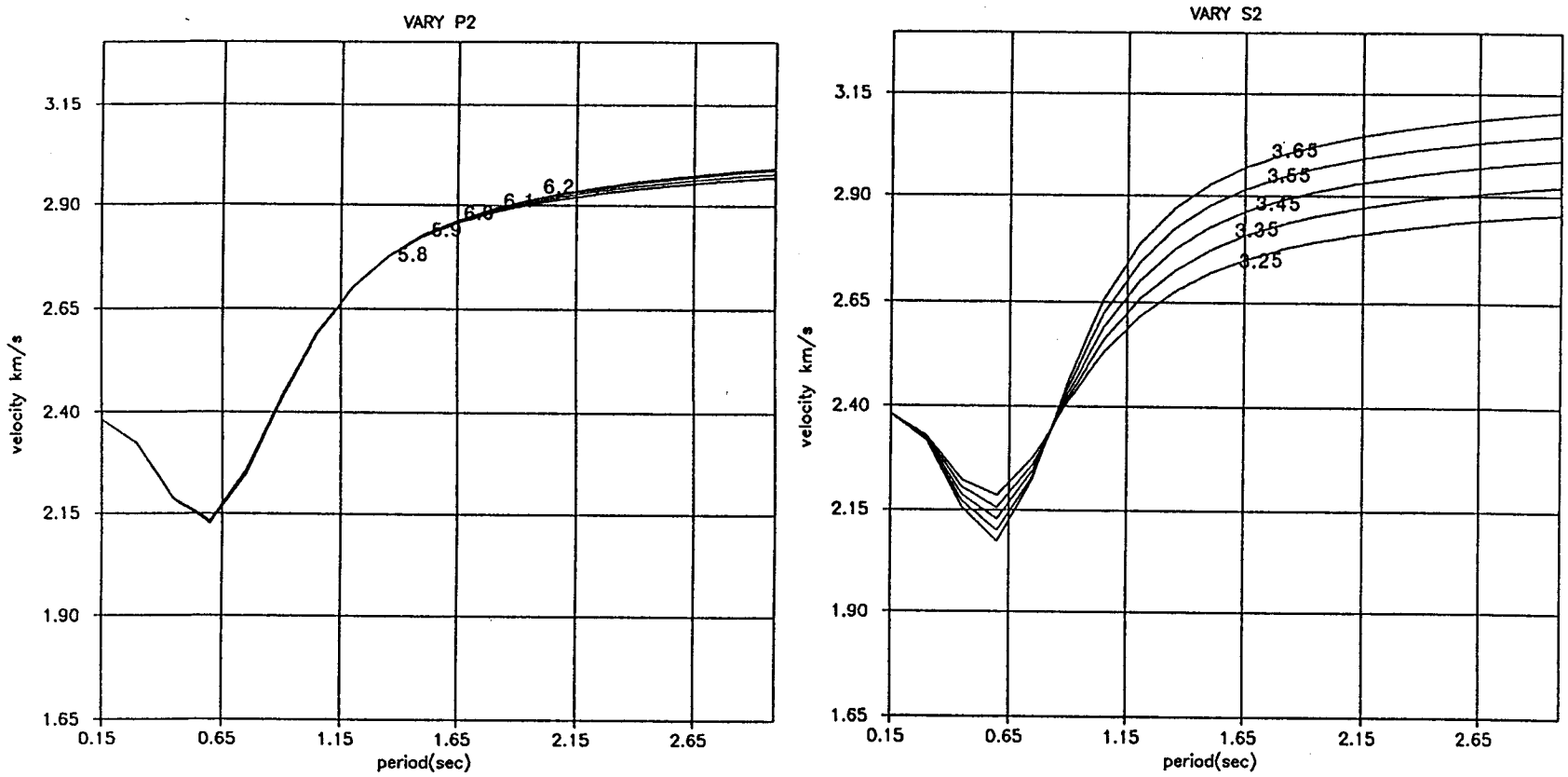

Figure 45. Variation curves for Rayleigh waves.

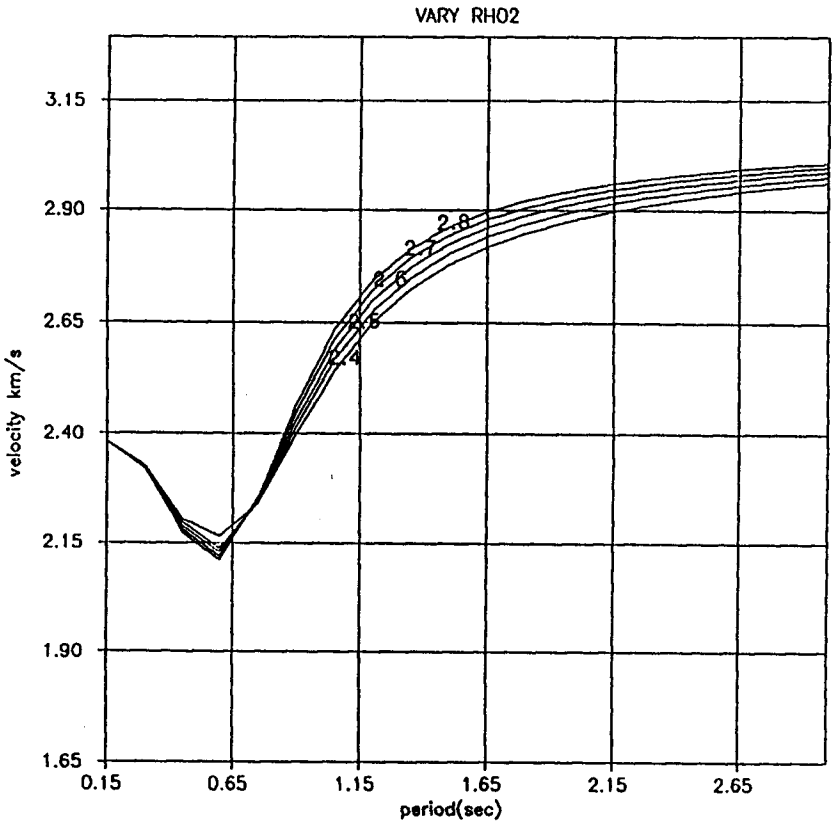

Figure 46. Variation curve for Rayleigh waves.

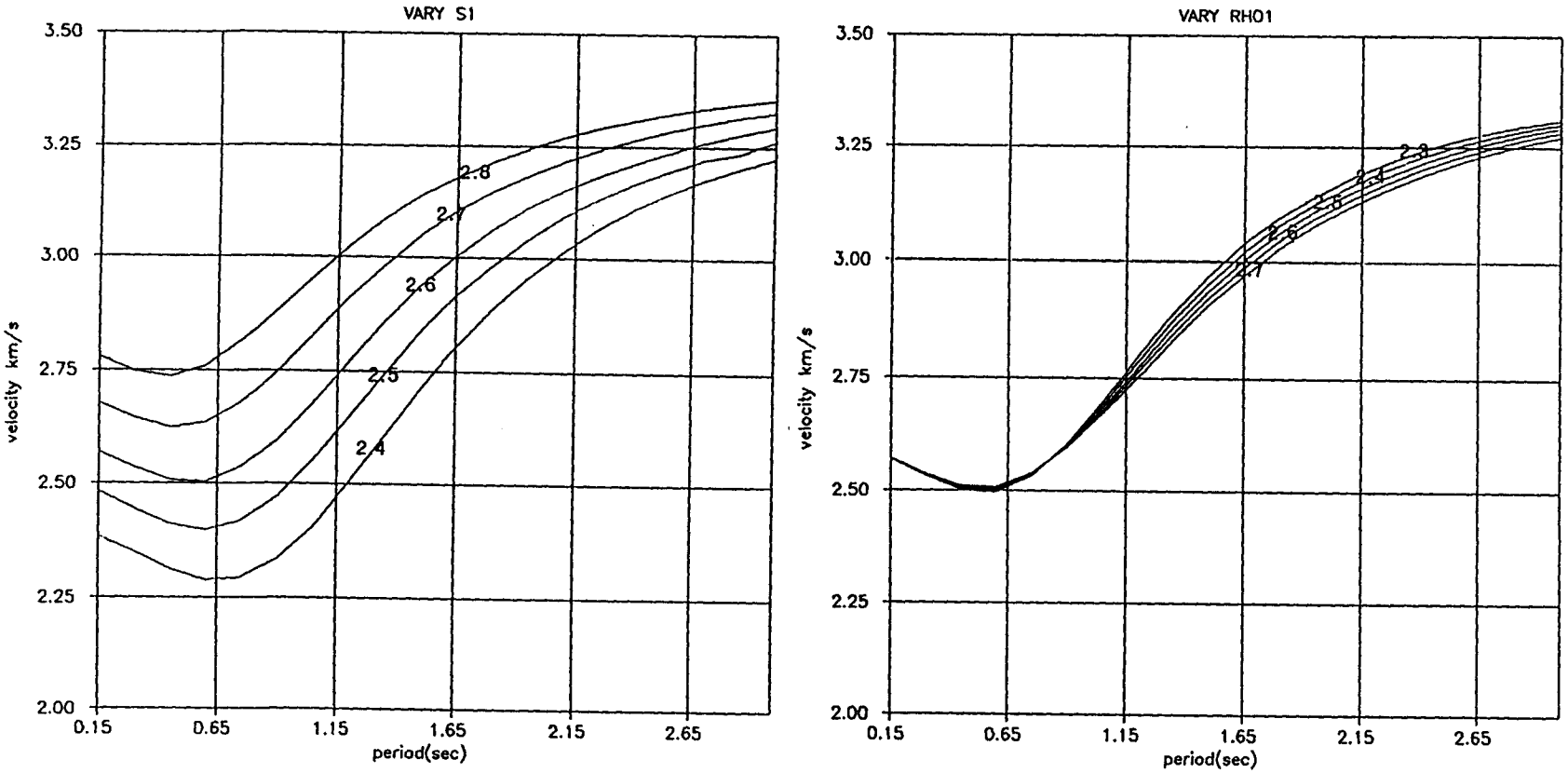

Figure 47. Variation curves for Love waves.

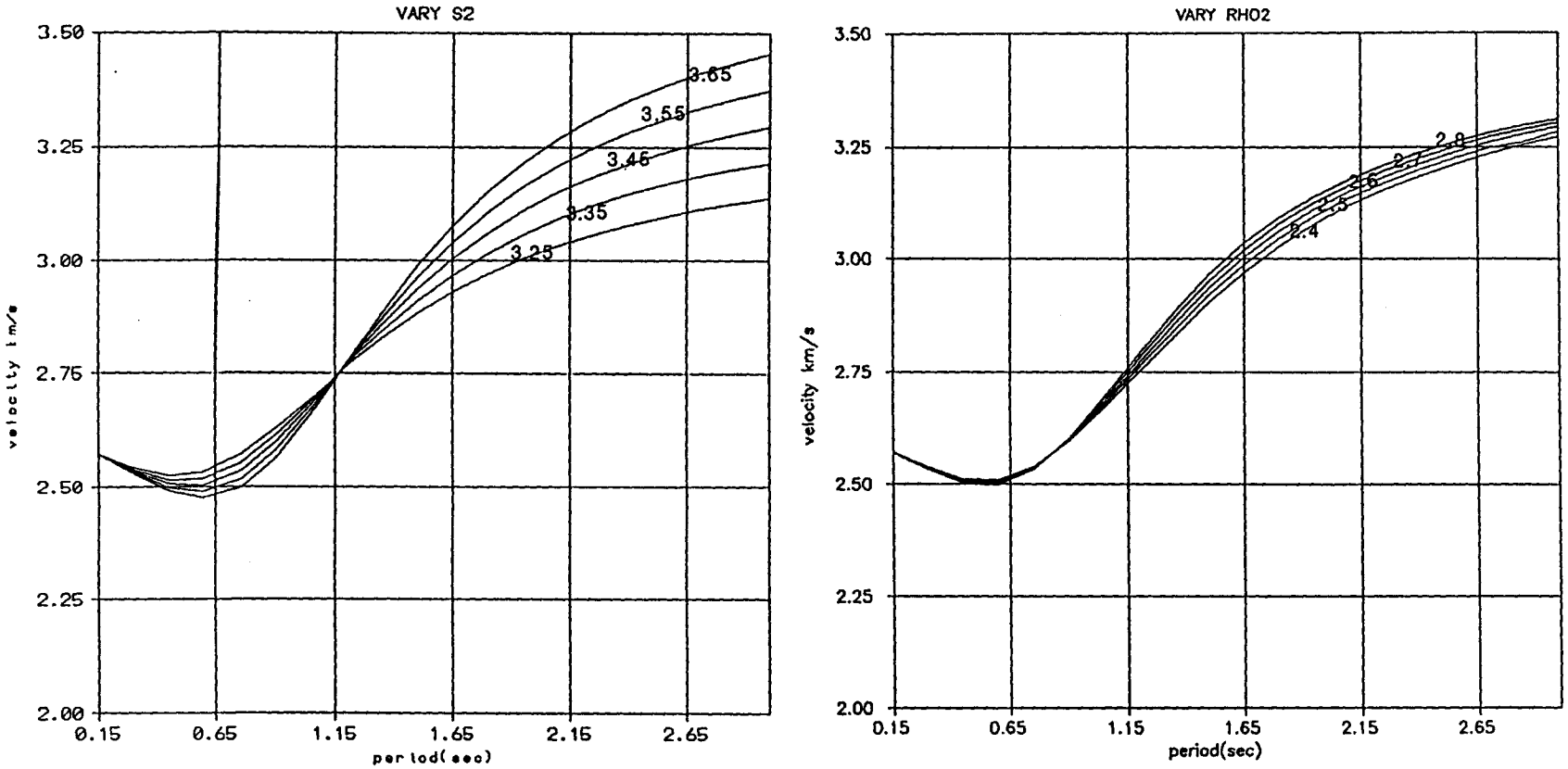

Figure 48. Variation curves for Love waves.

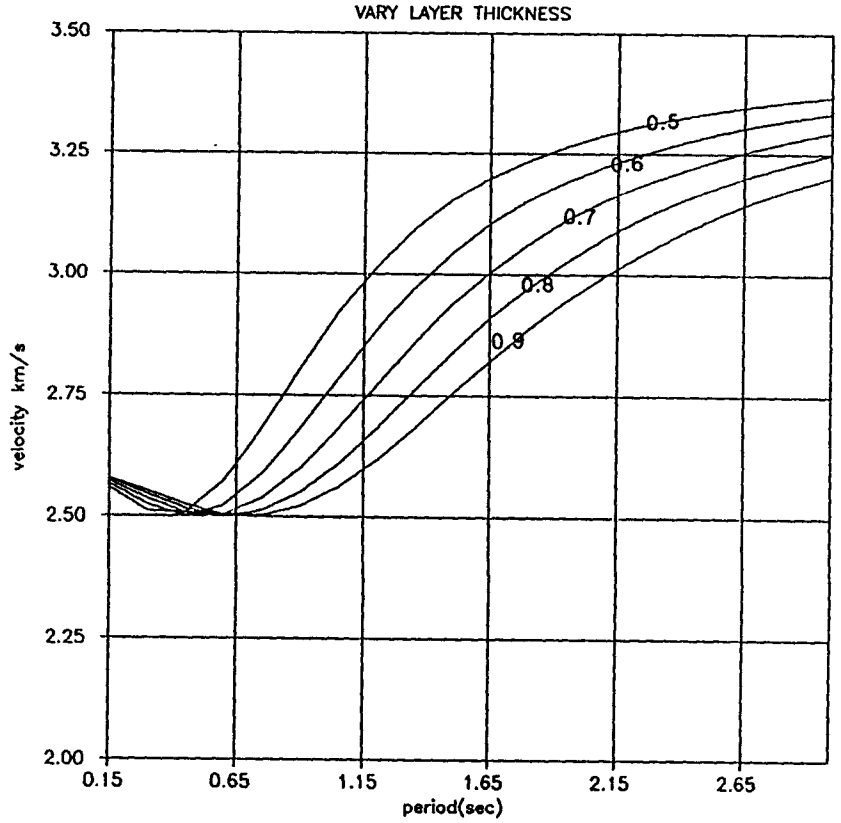

Figure 49. Variation curve for Love waves.

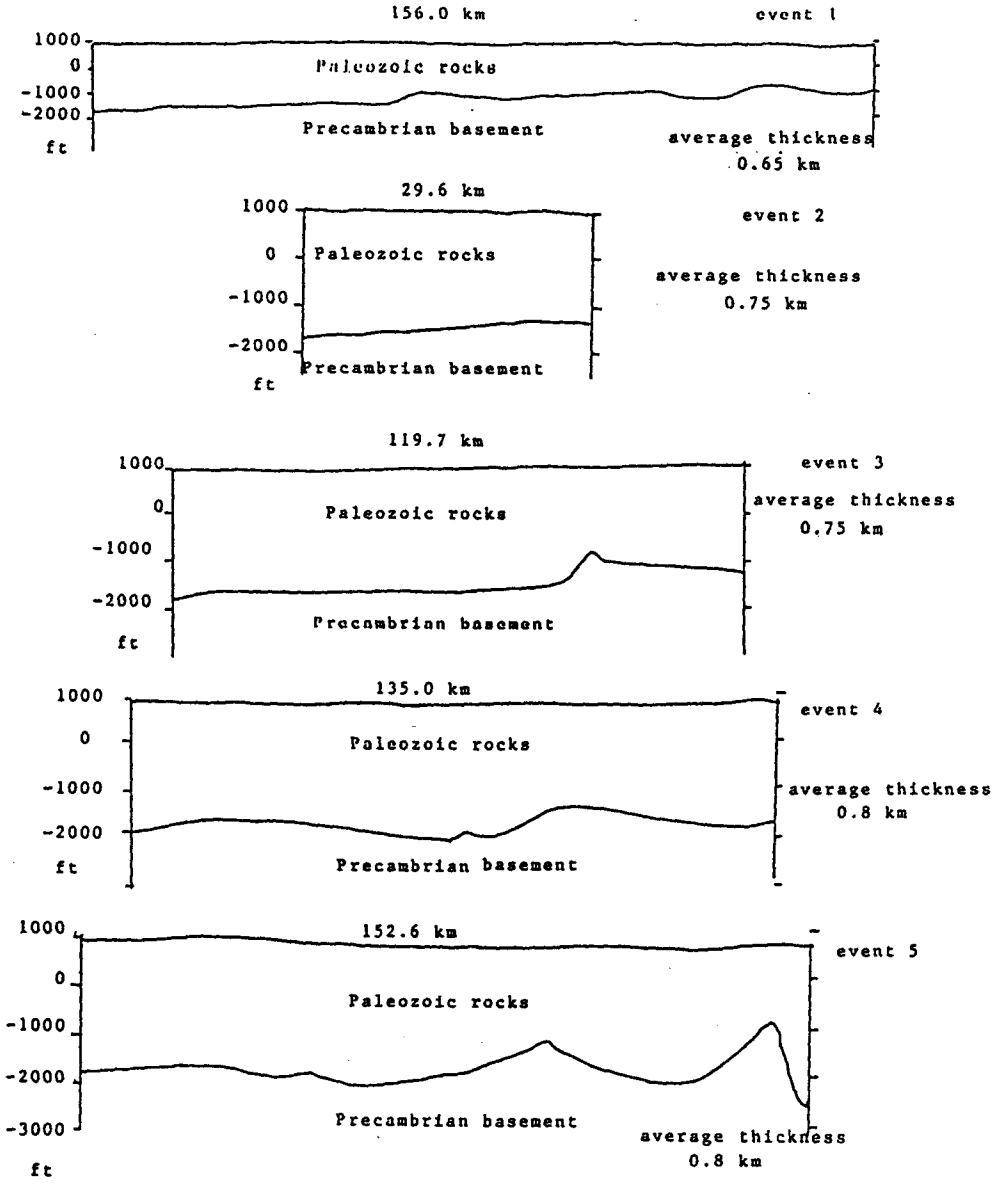

Figure 50. Thicknesses of the Paleozoic sedimentary section between the sources and the array.

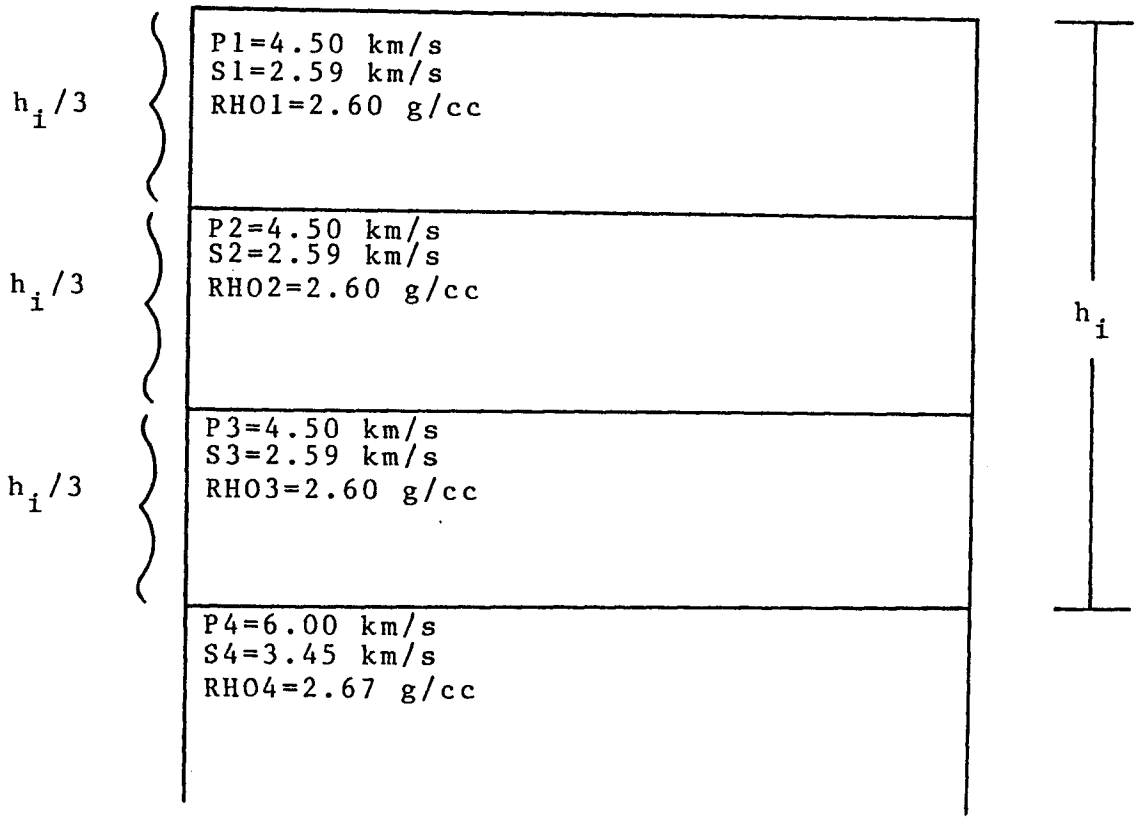

Figure 51. Initial velocity model for an inversion.

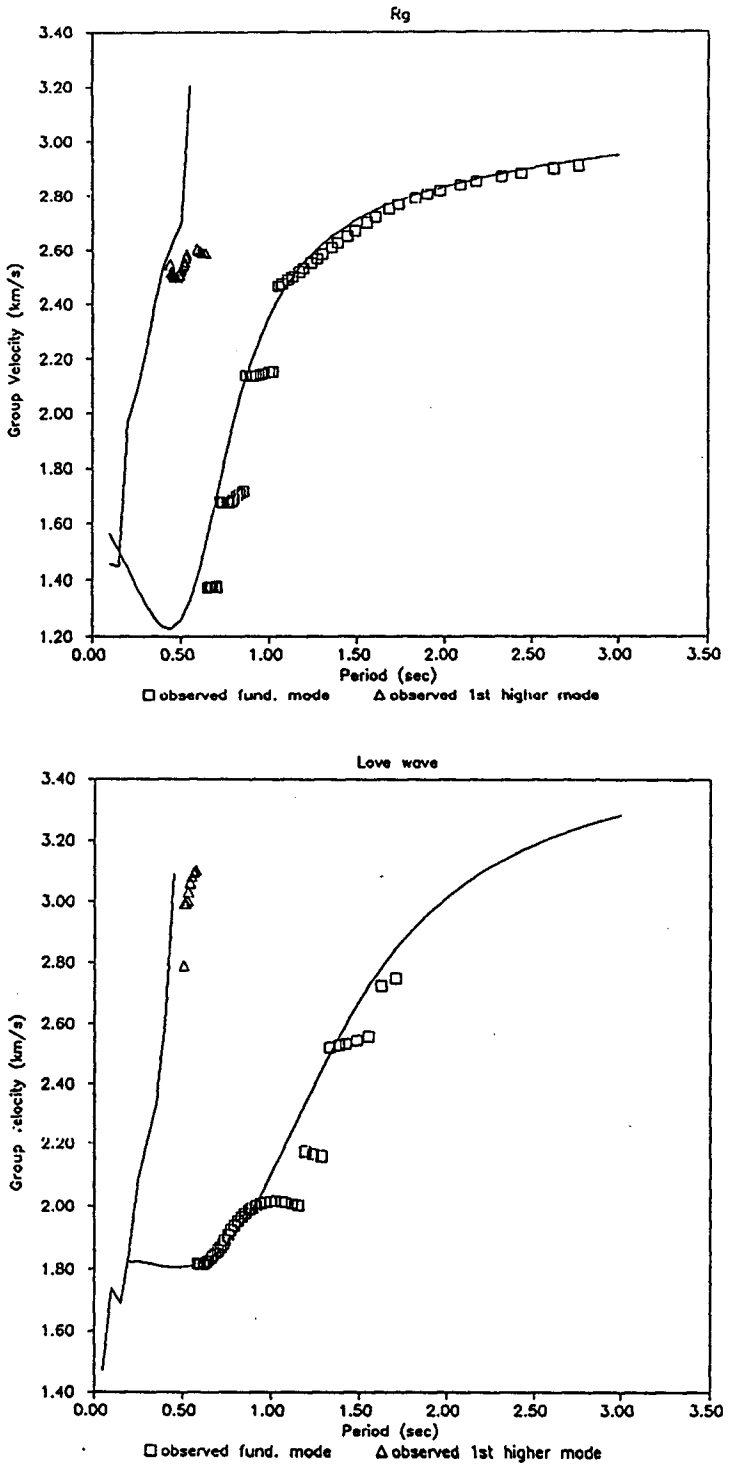

Figure 52. Final match between observed and theoretical dispersion data for event 1.

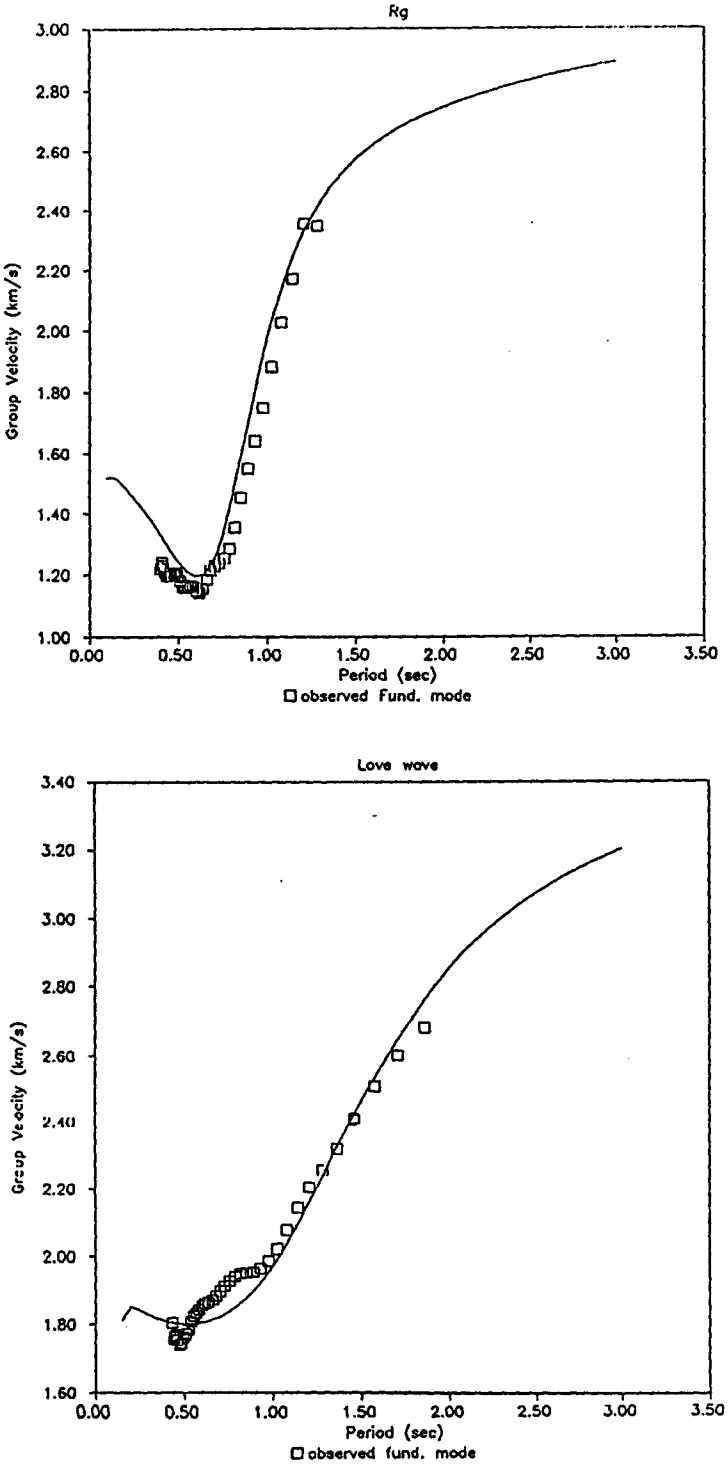

Figure 53. Final match between observed and theoretical dispersion data for event 2.

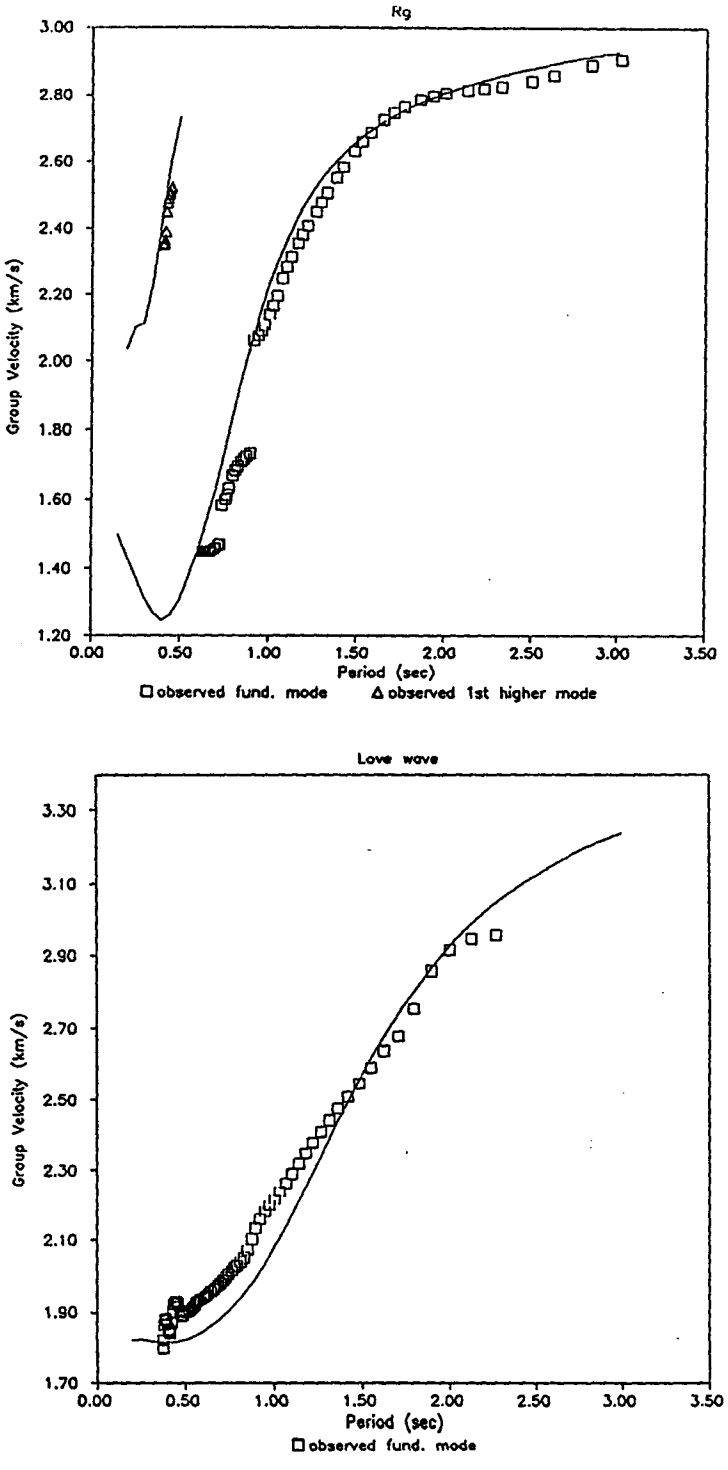

Figure 54. Final match between observed and theoretical dispersion data for event 3.

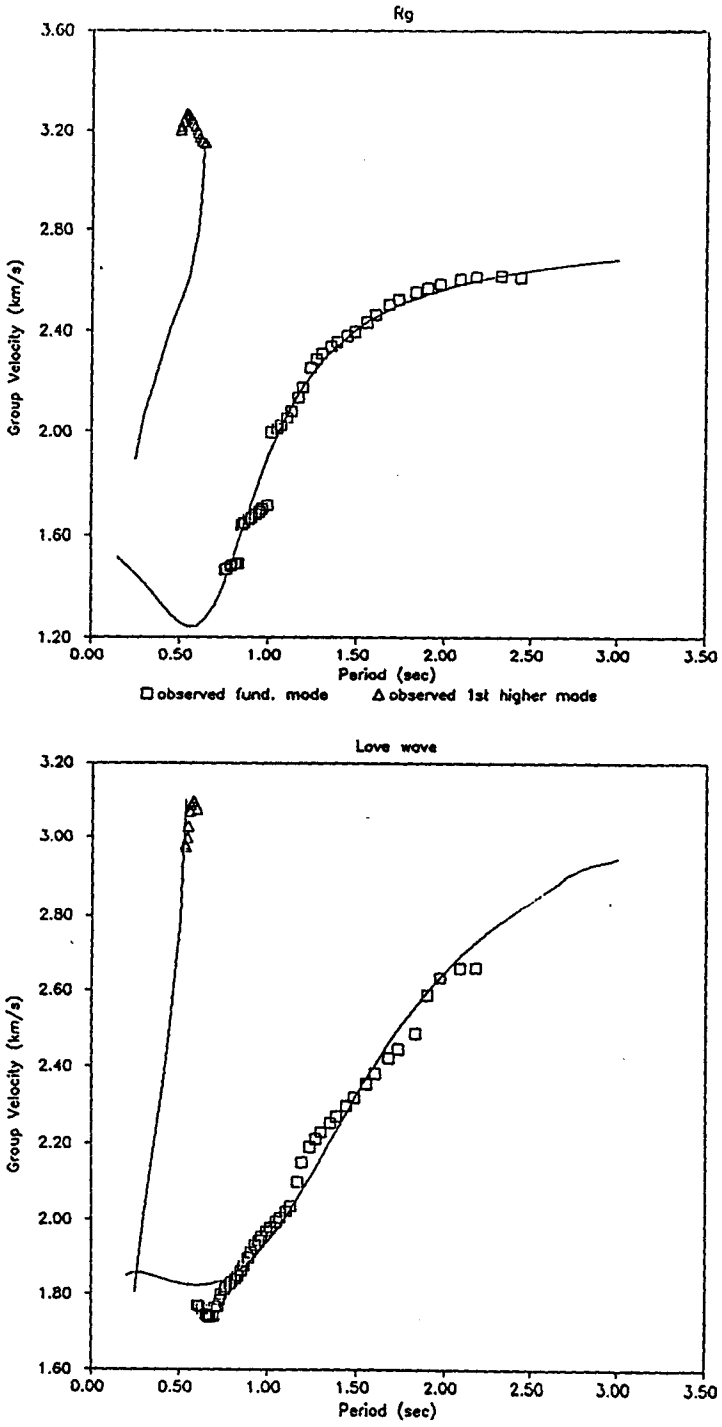

Figure 55. Final match between observed an theoretical dispersion data for event 4.

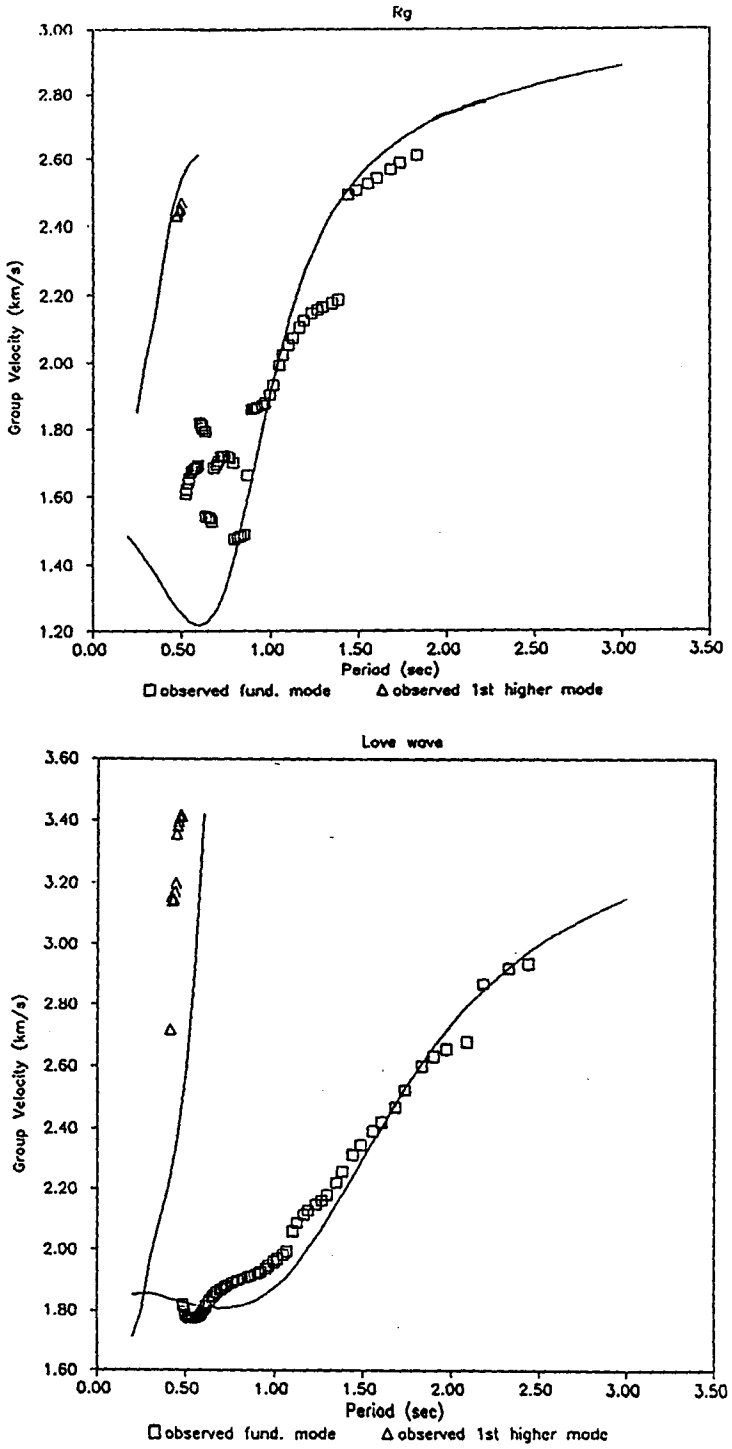

Figure 56. Final match between observed and theoretical dispersion data for event 5.

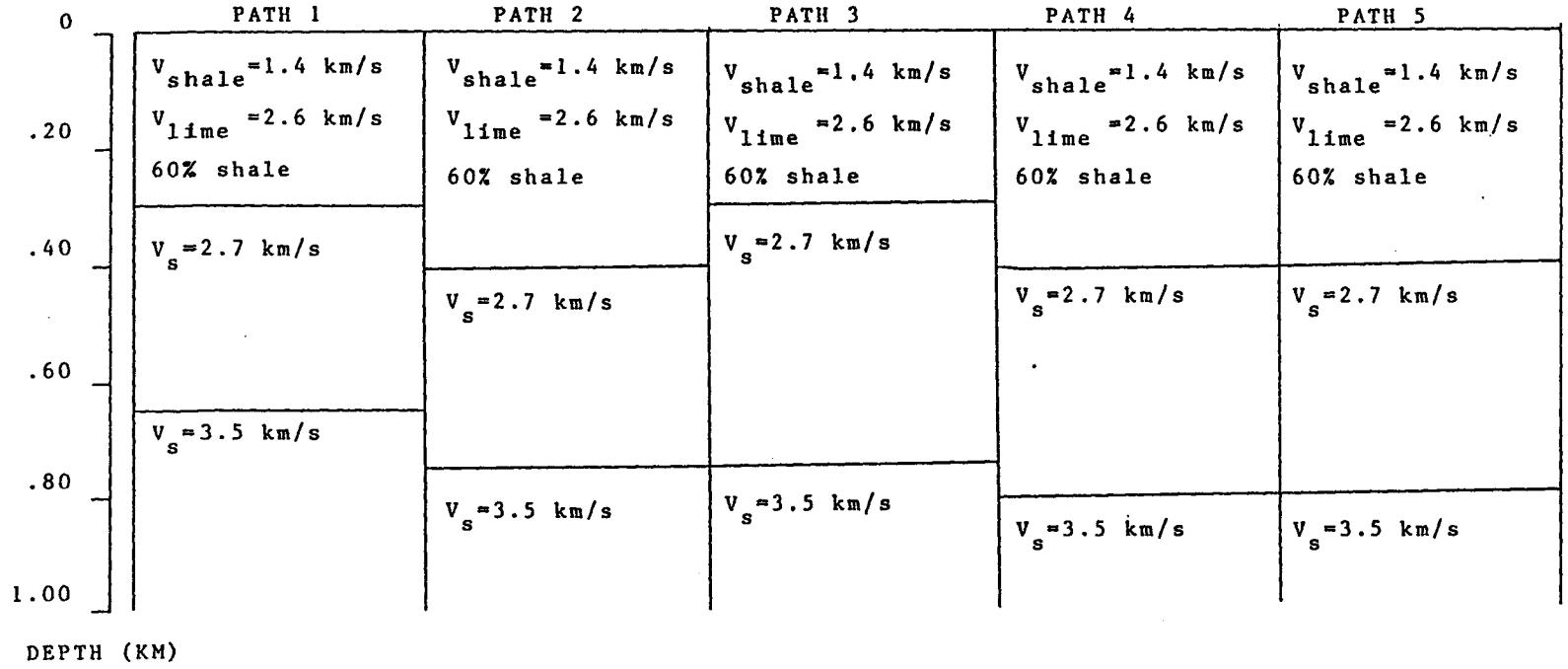

Figure 57. Final seismic velocity models along each of the five propagation paths.

THE EFFECTS OF NEAR-SURFACE LAYERING

During the inversion process, a question arose: Is it necessary to consider the interbedded nature of the shales and limestones within the Pennsylvanian section, or is it sufficient to derive a single average velocity for this layer? This question was answered through a simple modeling exercise.

Rg and Love-wave, group-velocity dispersion was determined for two velocity models (Figure 58). Model 1 has sixteen 0.02 km-thick layers with alternating S-wave velocities of 1.4 and 2.6 km/s (these are average shale and limestone velocities respectively, as shown by Dobrin, 1976), overlying one layer and a half-space. Model 2 has a single surface layer 0.32 km-thick, with a velocity equal to the average of the sixteen layers of model 1 (2.0 km/s). The calculated group dispersion (Figure 58) indicated that Rayleigh waves are very sensitive to layering of this sort near the surface. This is reflected in the differences between the two curves at short periods (Figure 58). Love waves are not found to be particularly sensitive to this layering at any period (Figure 58). The conclusion is that the interbedded layers of shale and limestone that compose the Pennsylvanian section should be considered in the

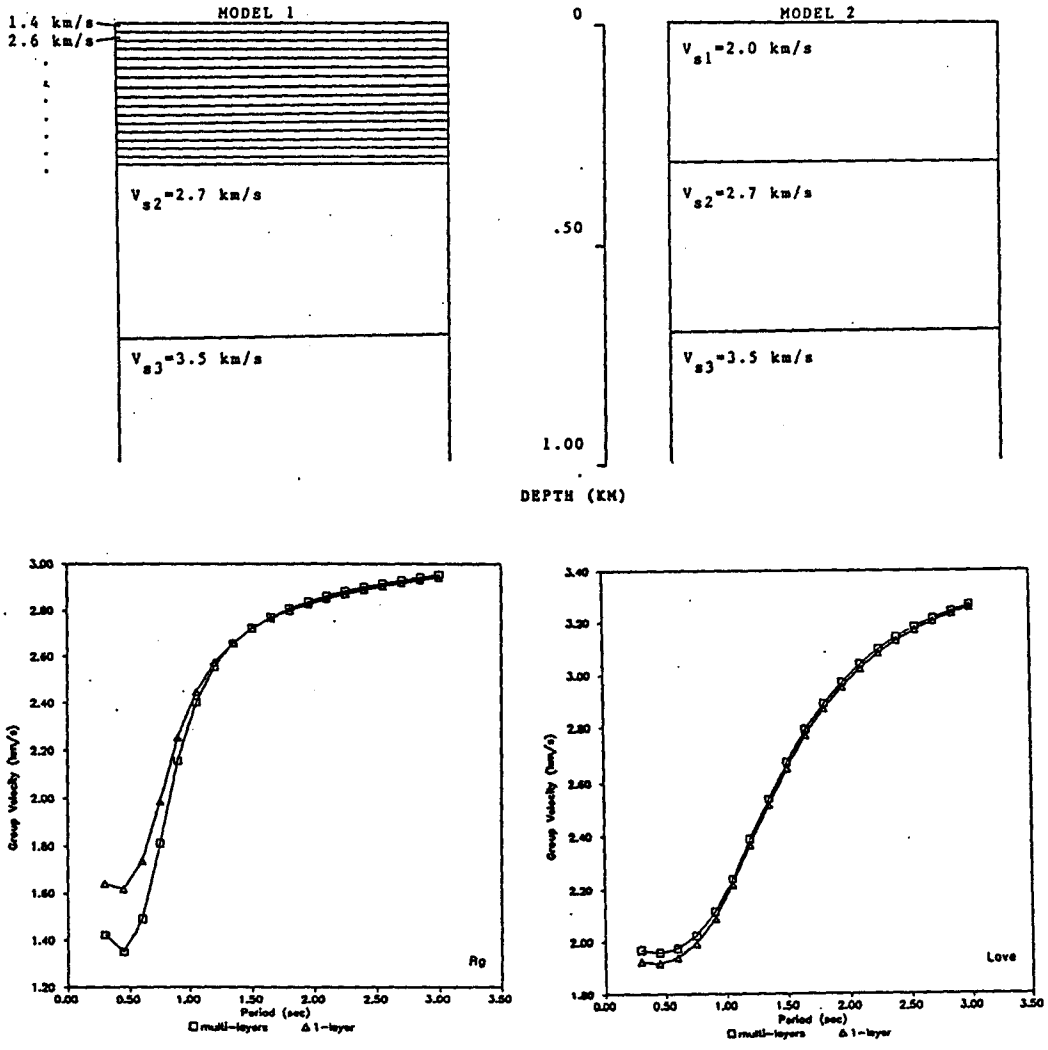

Figure 58. Single-layer average and multilayer models, as well as the computed group dispersion curves for these models. The squares show the dispersion for model 1 and the triangles show the dispersion for model 2.

inversion when there is dispersion data present at periods less than 1 second.

DISCUSSION

Analysis of the derived velocity models (Figure 57) indicates that the observed dispersion data can be explained by a velocity model of two layers over a half-space. The first layer appears to correspond to rocks of Pennsylvanian age. This layer has an average S-wave velocity of 1.9 km/s. The second layer appears to correspond to Mississippian and Cambro-Ordovician age rocks. This layer has an S-wave velocity of 2.7 km/s. The half-space corresponds to the Precambrian basement complex and has an S-wave velocity of 3.5 km/s. The thicknesses within the derived models are effectively constrained to within ± 0.05 km. The velocities of the first layer are constrained to within ± 0.1 km/s, layer 2 to within ± 0.2 km/s, and the half-space to within ± 0.1 km/s. Variations in the thicknesses of these two layers throughout the region seem to account for the slight differences in the various dispersion curves observed from different azimuths (Figure 35).

As previously mentioned, the Pennsylvanian section is composed largely of numerous layers of interbedded

shales and limestones (Figure 59). Initially, an average S-wave velocity and thickness were derived for this layer. The single layer was then replaced with a sequence of thin layers representing interbedded shales and limestones. The total thickness of the sequence was equivalent to the initially derived thickness of the layer. The interval velocities and the thicknesses of the thin layers, as well as the total thickness of the sequence, were perturbed to induce further convergence between the observed and theoretical data. The dispersion curves have minimum residuals (for all five of the propagation paths) for thin layers of shale and limestone with S-wave velocities of 1.4 km/s and 2.6 km/s respectively and a 3/2 shale to limestone ratio. Analysis of a composite Pennsylvanian section (Figure 59) indicates that the section is indeed roughly 60% shale (at least in Kansas). The information derived from the inversion agrees with geological information. Using an Rg phase recorded from a mining explosion, McEvilly and Stauder (1965) determined an S-wave velocity of 1.9 km/s for the Pennsylvanian section across the Illinois Basin, a value in agreement with the average velocity of the Pennsylvanian section determined in this study.

Early in the inversion process, it was assumed that the observed dispersion could be explained by a three-layer, over a half-space velocity model (Figure 51). During the inversion, the second and third layers converged into a single layer. This layer has a much higher S-wave velocity than does layer 1. The S-wave velocity of 2.7 km/s is very close to the average velocity found for carbonate rocks (Dobrin, 1976). The Mississippian and the Cambro-Ordovician age rocks in the study region are composed almost entirely of limestone (Mississippian) and dolomites (Cambro-Ordovician Arbuckle Group). This high-velocity layer correlates well with the Mississippian and Cambro-Ordovician rocks of the region (Figure 6). McEvilly and Stauder (1965) derived an S-wave velocity of 2.8 km/s for the Ordovician section across the Illinois Basin. Again this value agrees fairly well with the S-wave velocity for the rocks of Ordovician age found in this study.

The correspondence between the half-space of the derived velocity model and the Precambrian basement is unequivocal. The S-wave velocity of the half-space (3.5 km/s) is in close agreement with basement S-wave velocities determined in other short-period, surface-wave dispersion studies in the Mid-continent region (McEvilly and Stauder, 1965; Herrmann, 1969). The P-

wave velocity of the half-space is 6.09 km/s ($v_p = 1.74 v_s$). This value is consistent with basement velocities determined from crustal-scale refraction studies in the Mid-continent region (Tryggvason and Qualls, 1967; Healy and Warren, 1969; Steeples and Miller, 1987).

As previously mentioned, potential errors in the determination of the P-wave travel times can effect the measured group velocities greatly at long periods (maximum error from +0.06 km/s to -0.11 km/s) and somewhat less at short periods (+0.01 km/s to -0.02 km/s). Velocity models are derived for the observed group-dispersion data with the maximum positive and negative errors applied. For the maximum positive error (from +0.06 km/s at long periods to +0.01 km/s at short periods), the derived velocity models are very similar to those shown in Figure 57. The only difference being that the basement velocity is about 3% higher (3.6 km/s). For the maximum negative error (-0.11 km/s at longer periods to -0.02 km/s at shorter periods), the derived velocity models are somewhat similar to those shown in Figure 57. The thicknesses of the layers are identical, but the basement velocity is about 4% lower (3.35 km/s), layer 2 is about 2% lower (2.65 km/s) and layer 1 is about 3% higher (average = 1.95 km/s). These

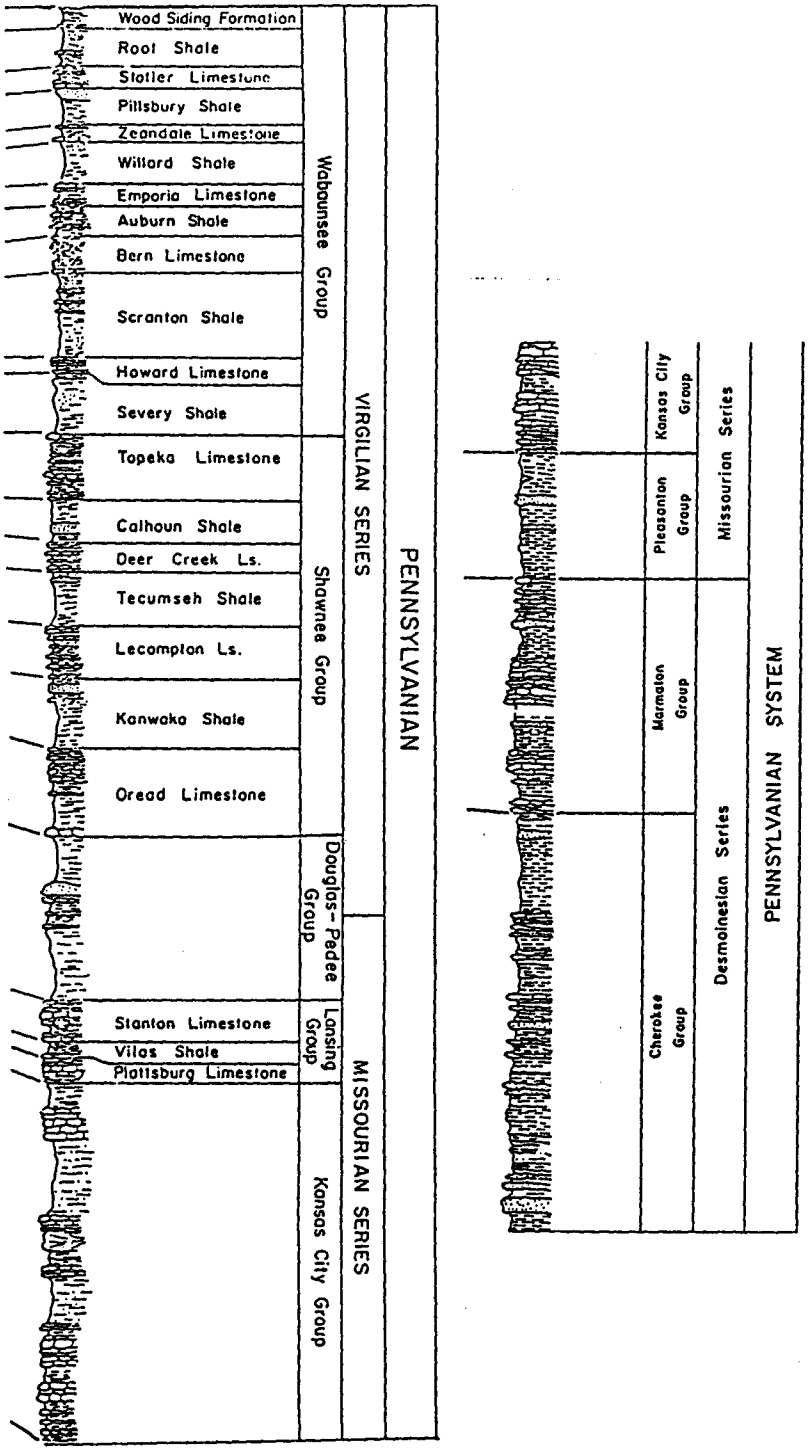

Figure 59. A composite Pennsylvanian surface section. Note that the section is composed of approximately 60% shale and 40% limestone (after Merriam, 1963).

upper and lower velocity limits represent the limits of the velocity model due to possible travel-time errors.

CONCLUSIONS

1) The observed Rg bearing anomalies may be due to a variety of reasons; diffraction by positive basement topography, lateral reflection, or lateral refraction across velocity boundaries in the basement. The lateral refraction theory appears to be particularly appealing. The basement-rock-type below the array is different than the basement-rock-types below the four source locations from which the bearing anomalies were observed. If the basement-rock-types have different seismic velocities then the surface waves will experience lateral refraction across the boundaries.

2) The observed surface-wave trains appear to be highly contaminated with multipath arrivals (particularly the Rg phases). Multipath arrivals give the measured group-dispersion data a highly disjointed appearance at short periods. The multipathed dispersion curves can be inverted with the knowledge that the multipathed segments follow the same trend as an unmultipathed

curve, but will be shifted slightly downward in group velocity.

3) The observed Rg and Love-wave dispersion curves can be simultaneously inverted for shallow-crustal velocity structure. Figures 52-56 show the final matches between the observed and theoretical Rg and Love-wave dispersion curves. The fit of the observed Rg dispersion data to the theoretical Rayleigh-wave dispersion curves is excellent. The fit of the observed Love-wave dispersion data to theoretical Love-wave dispersion curves is fairly good.

4) The generally good match between the suspected higher-mode data and theoretical, 1st higher-mode dispersion curves (Figures 52-56) indicates that at least 1st higher-mode energy exists. The higher-mode energy is not well resolved because the data were resampled too severely. Both Rg and Love-wave, 1st higher-mode data are present, but neither are used as a constraint in the inversion.

5) The result of each inversion leads to information about the shallow-crustal velocity structure along each of the five propagational paths. Throughout the study

region, the short-period, surface-wave dispersion can be explained by the same basic velocity model (Figure 57) of two layers overlying a half-space. The differences in the group dispersion observed from various azimuths can be explained by variations in the thicknesses of the two layers.

6) The derived velocity models appear to correlate well with the known geological structure of the region. The first layer has an average S-wave velocity of 1.9 km/s and corresponds to the Pennsylvanian age rocks of the region. The second layer has an S-wave velocity of 2.7 km/s and corresponds to Mississippian and Cambro-Ordovician age carbonate rocks. The half-space corresponds to the Precambrian basement complex with an S-wave velocity of 3.5 km/s.

7) A unique method of determining the ratio of limestone-to-shale for a section of Pennsylvanian rocks in Kansas or Oklahoma is proposed. At periods less than one second, Rayleigh-wave dispersion is very sensitive to the interbedded nature of the shales and limestones that compose the Pennsylvanian cyclothems in the region. It is necessary to model the Pennsylvanian section as a sequence of thin layers with alternating shale and

limestone velocities, as opposed to a single layer with a single average seismic velocity. Rayleigh-wave dispersion is so sensitive, that the proper choice of shale-to-limestone ratio is necessary to minimize the residuals between the observed and theoretical data. A 3/2 shale to limestone ratio was found for the Pennsylvanian rocks in the study region. This ratio is in agreement with a composite surface section shown by Merriam (1963). Love-wave dispersion is largely insensitive to the layering in the Pennsylvanian.

8) Short-period surface-waves can provide valuable insight into the near-surface crustal structure in a region where the geology is not independently known. This will be of value in the event that a seismic array is deployed in the USSR if a nuclear test ban treaty is signed.

BIBLIOGRAPHY

Aki, K. and P.G. Richards (1980). Quantitative Seismology: Theory and Methods. W. H. Freeman and Company, San Francisco, 2 vol., 932 p..

Anderson, J. and J. Dorman (1973). Local geological effects on short-period Rayleigh waves around New York City. Bull. Seis. Soc. Am., Vol. 63, p. 1487-1497.

Bath, M. (1973). Introduction to Seismology, Halstead Press, New York, 395 p..

Bath, M. (1975). Short-period Rayleigh waves from near surface events. Phys. Ea. and Plan. Int., Vol. 10, p. 369-376.

Bhattacharya, S. N. and H. N. Srivastava (1973).. Shallow structure of Poona-Karad profile using short-period Rayleigh-wave dispersion. Bull. Seis. Soc. Am., Vol. 63 p. 2197-2199.

Bickford, M.E., K. L. Harrower, R. L. Nussbaum, J.J. Thomas, B.K. Nelson and W. J. Hoppe (1981). Rb-Sr and U-Pb and geochronology and distribution of rock types in the Precambrian basement of Missouri and Kansas. Geol. Soc. Am. Bull., Vol. 92, p. 323-341.

Bolt, B.A. (1982). Inside The Earth : Evidence From Earthquakes. W.H. Freeman and Co., San Francisco, 191 p..

Burchett, R.R., K.V. Luza, O.J. Van Eck and F.W. Wilson (1983). Seismicity and Tectonic Relationships of the Nemaha Uplift and Midcontinent Geophysical Anomaly. U.S., Nuclear Regulatory Commission, Report no. NUREG/CR -3117.

Dobrin, M.B., R. F. Simon and P.L. Lawrence (1951). Rayleigh waves from small explosions. Trans. Am. Geophs. Un., vol. 32, p. 822-832.

Dobrin, M.B. (1976). Introduction to Geophysical Prospecting. McGraw Hill, New York, 630 p..

Dziewonski, A., S. Bloch and M. Landisman (1969). A technique for the analysis of transient seismic signal. Bull. Seis. Soc. Am., vol. 70, p. 427-444.

Ewing, M. and F. Press (1959). Determination of crustal structure from phase-velocity of Rayleigh waves. Bull. Seis. Soc. Am., Vol. 70, p. 229-244.

Garland, G. D. (1979). Introduction to Geophysics : Mantle, Core and Crust. W.B. Saunders Co., Philadelphia, 494 p..

Harkrider, D. G. (1970). Surface-waves in multilayered elastic media II : higher mode spectra and spectral ratios from point sources in plane layered earth models. Bull. Seis. Soc. Am., Vol. 60, p. 1937-1957.

Haskell, N.A. (1951). The dispersion of surface-waves on multilayered media. Bull Seis. Soc. Am., Vol. 43, p. 17-34.

Healy, J.H. and D.H. Warren (1969). Explosion seismic studies in North America. From: The Earth's Crust and the Upper Mantle, Pembroke J. Hart editor. Geophysical Monograph 13, Am. Geophy. Union, p. 208-225.

Herrmann, R.B. (1969). The structure of the Cincinnati Arch as determined from short-period Rayleigh waves. Bull. Seis. Soc. Am., vol. 59, p. 399-407.

Kafka, A.L. and E.C. Reiter (1987). Dispersion of Rg waves in southeast Maine: evidence for lateral anisotropy in the shallow crust. Bull. Seis. Soc. Am., vol. 77, p. 925-941.

McEvilly, T.V. and W. Stauder (1965). Effect of sedimentary thickness on short-period Rayleigh-wave dispersion. Geophysics, Vol. 30, p. 198-203.

Merriam, D.F. (1963). The Geologic History of Kansas. State Geological Survey of Kansas, Bull. 162. 317 p..

Oliver, J. (1962). A summary of observed seismic surface-wave dispersion. Bull. Seis. Soc. Am., vol. 52 p. 81-86.

Sheriff, R.E. (1984). Encyclopedic Dictionary of Exploration Geophysics. Society of Exploration Geophysicists, Tulsa, 323 p..

Steeples, D.W. (1982). Structure of the Salina-Forest City interbasin boundary from seismic studies. Univ. of Missouri-Rolla Jour. no. 3, p. 55-81.

Steeples, D.W. and R.D. Miller (1987). Kansas refraction profiles : Proc. of Symposium on Geophysics in Kansas - a 25 year update, Nov. 1984. Kansas Geological Survey bull. 226, in press.

Thompson, W.T. (1950). Transmission of elastic waves through a stratified solid medium. Jour. Appl. Phys., vol. 21, p. 89-93.

Tipler, P.A. (1982). Physics. Worth Publishers Inc., New York, 2 Vol., 1062 p..

Tryggvason, E. and B. R. Qualls (1967). Seismic refraction measurement of crustal structure in Oklahoma. Jour. Geophys. Res., Vol. 72, p. 3738-3740.

Woollard, G.P. (1969). Standardization of gravity measurements. From: The Earth's Crust and Upper Mantle, Pembroke J. Hart; Editor. Geophysical Monograph 13. Am. Geophys. Union, p. 283-293.

Yarger, H.L. (1983). Regional Interpretation of Kansas Aeromagnetic Data. Kansas Geological Survey Geophysical Series 1. 35 p..

APPENDIX A

Narrow-band, frequency-wavenumber power spectra of the P-wave and Rg phases for each of the five recorded mining explosions. The seismic traces and the analysis windows are also shown. The estimated bearings (back-azimuths) and estimated velocities as measured from the plots, as well as the analysis frequencies of the phases are indicated.

event 1

P-wave

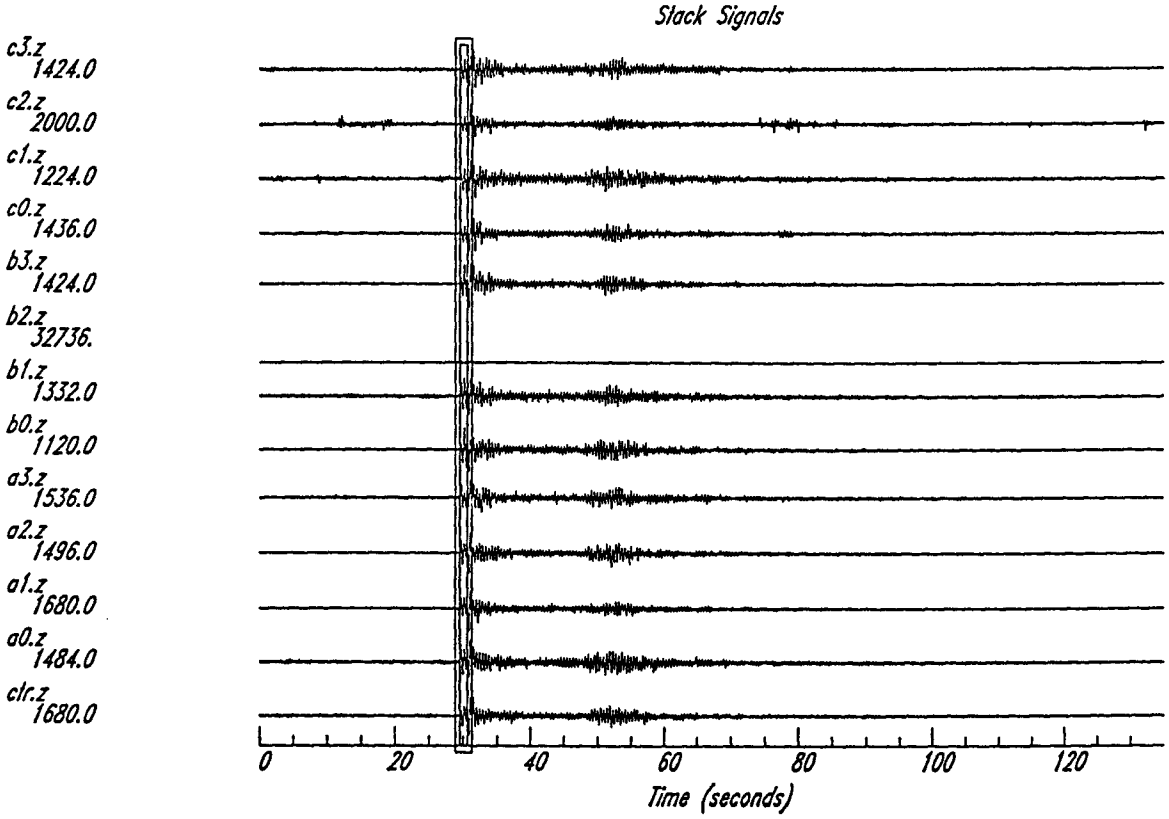

NBFK - single window

Estimated bearing: 66.559

Estimated velocity: 6.5627

Analysis frequency: 4.805

Max. horiz. wavenumber: 1.0000

Scaling type: LINEAR

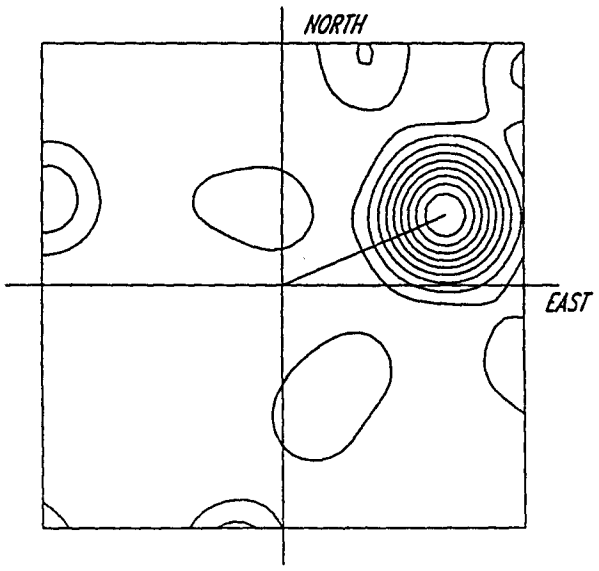

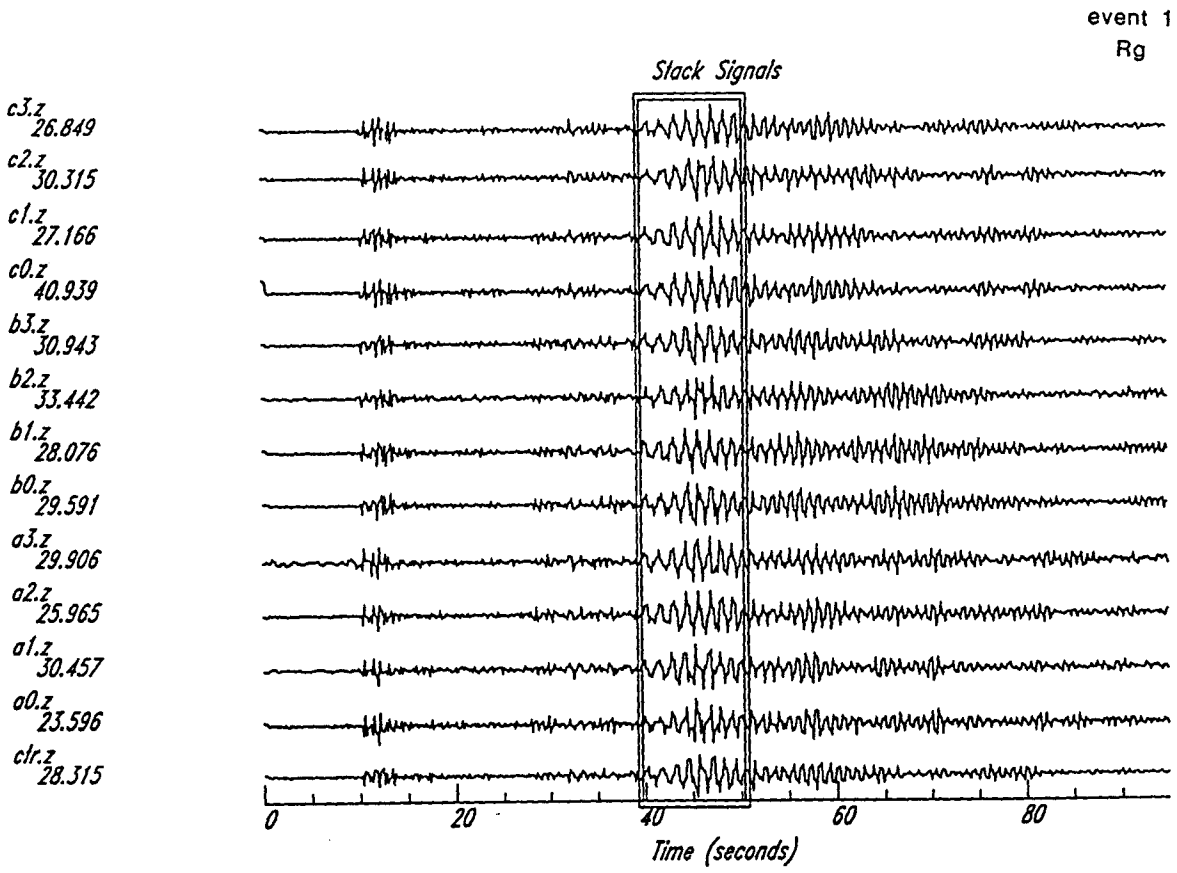

NBFK - single window

Estimated bearing: 60.781

Estimated velocity: 2.5832

Analysis frequency: 0.8094

Max. horiz. wavenumber: 1.0000

Scaling type: LINEAR

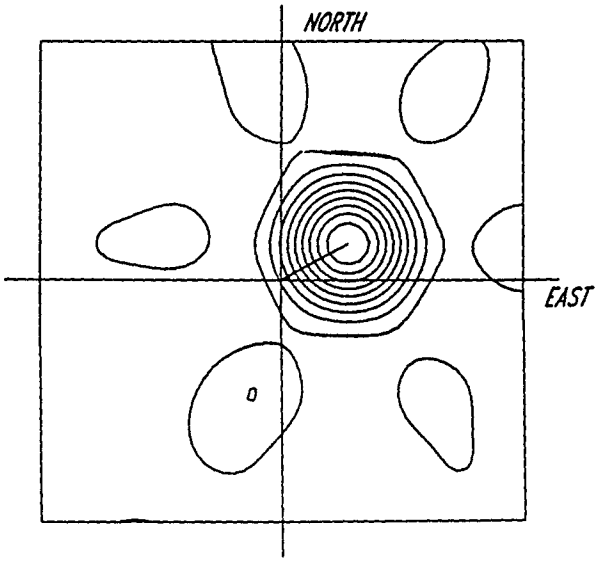

event 2
P-wave

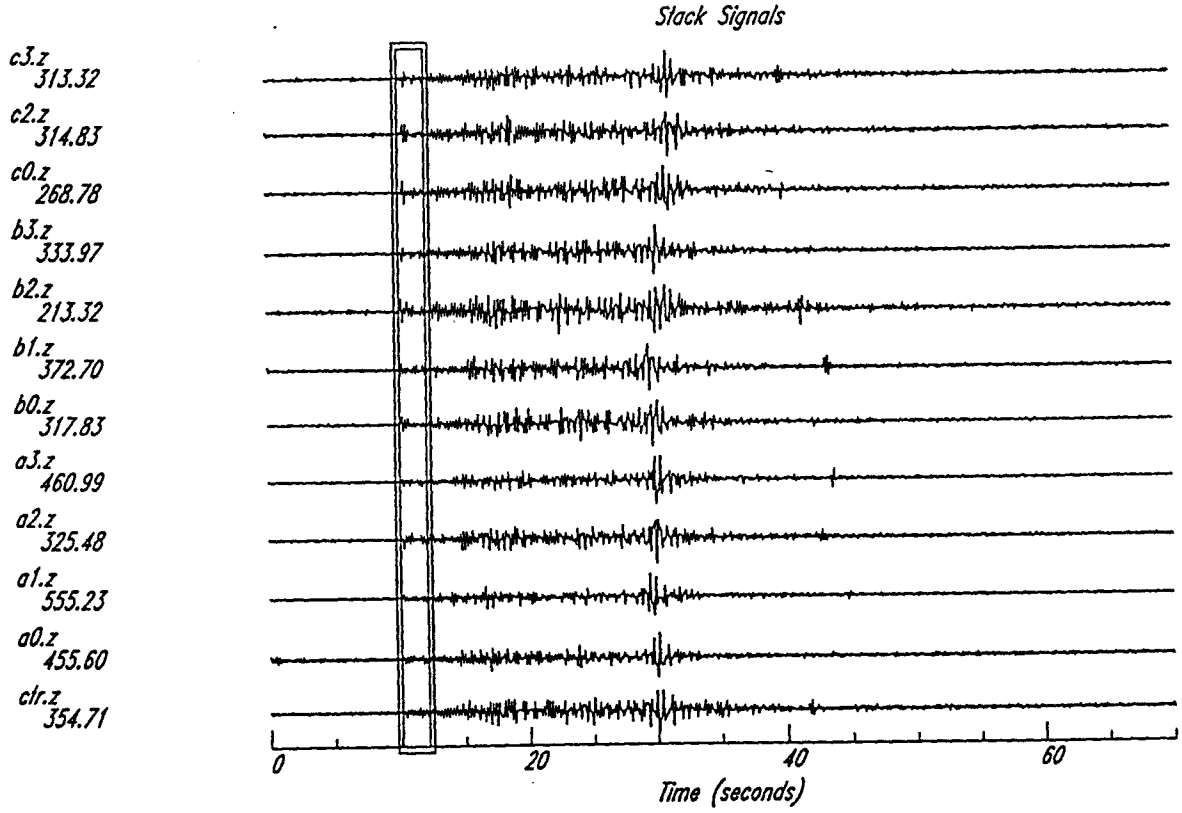

NBFK – single window

Estimated bearing: 103.44

Estimated velocity: 6.1085

Analysis frequency: 6.601

Max. horiz. wavenumber: 1.2000

Scaling type: LINEAR

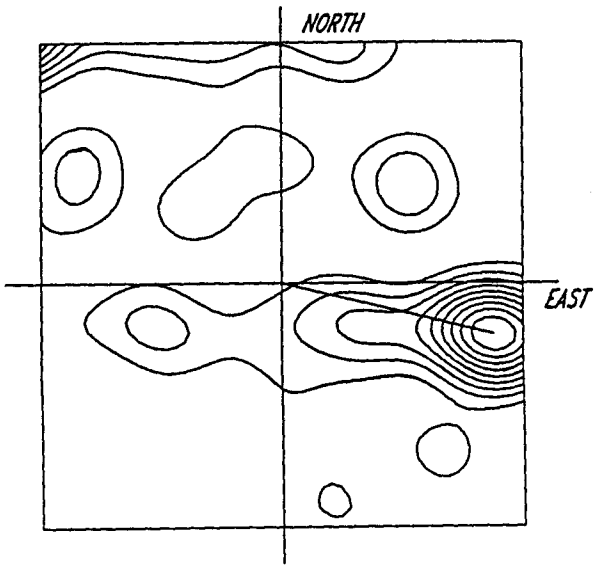

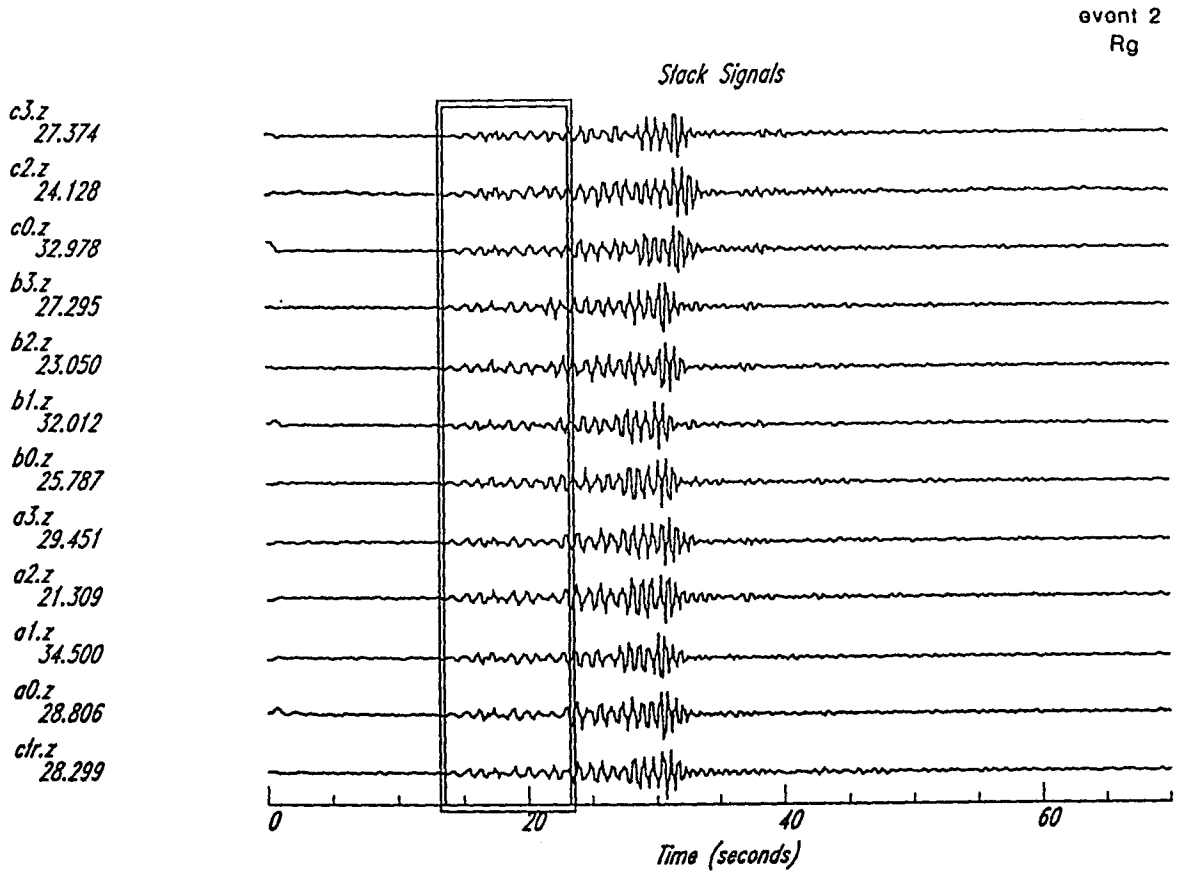

NBFK – single window

Estimated bearing: 101.80

Estimated velocity: 2.9987

Analysis frequency: 1.034

Max. horiz. wavenumber: 1.0000

Scaling type: LINEAR

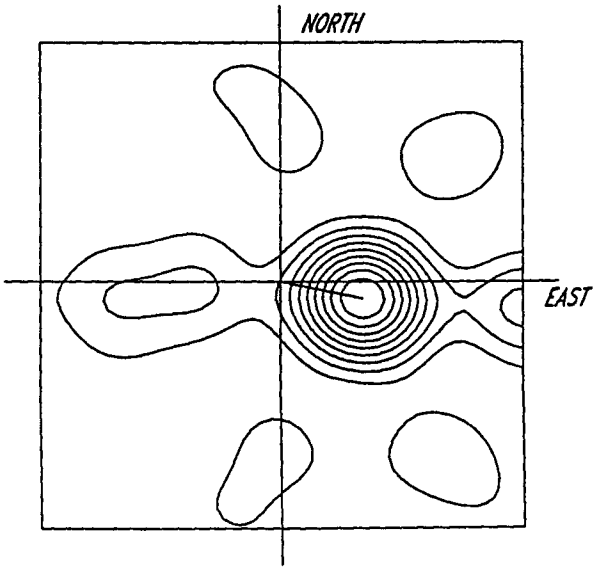

event 3
P-wave

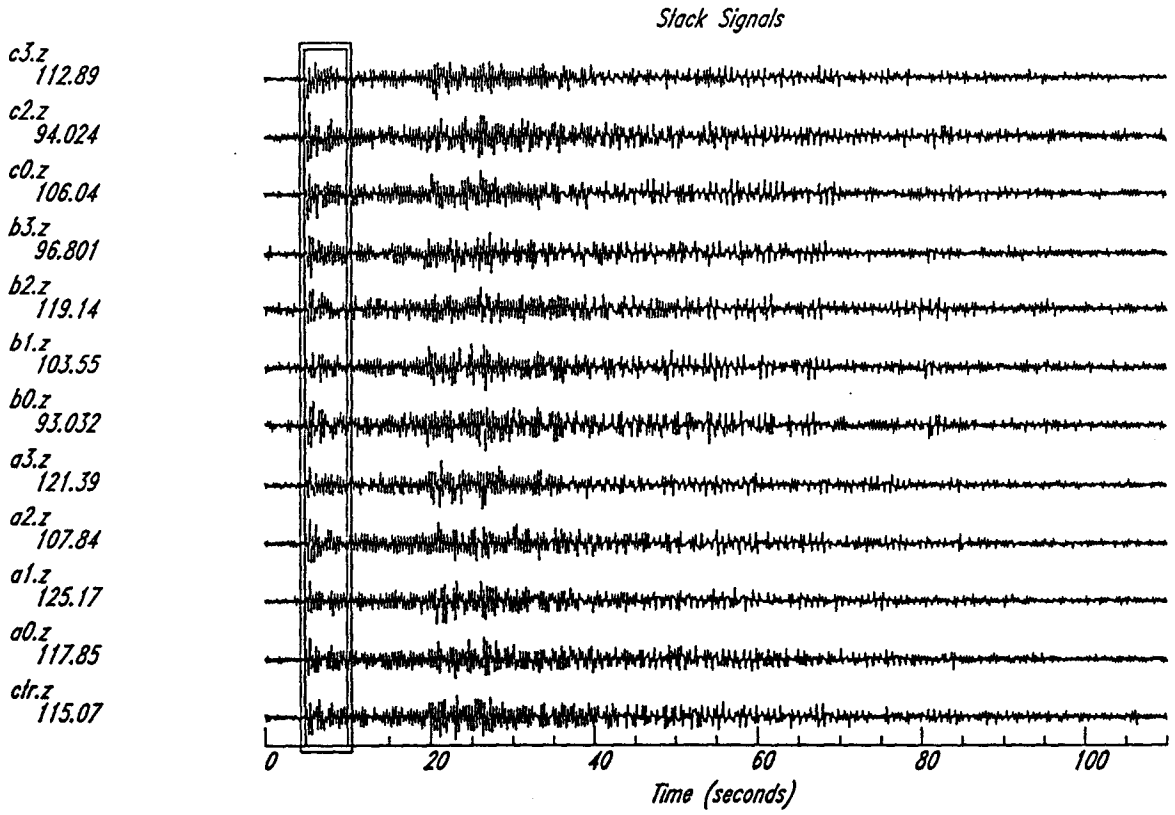

NBFK – single window

Estimated bearing: 141.32

Estimated velocity: 6.6231

Analysis frequency: 1.928

Max. horiz. wavenumber: 1.0000

Scaling type: LINEAR

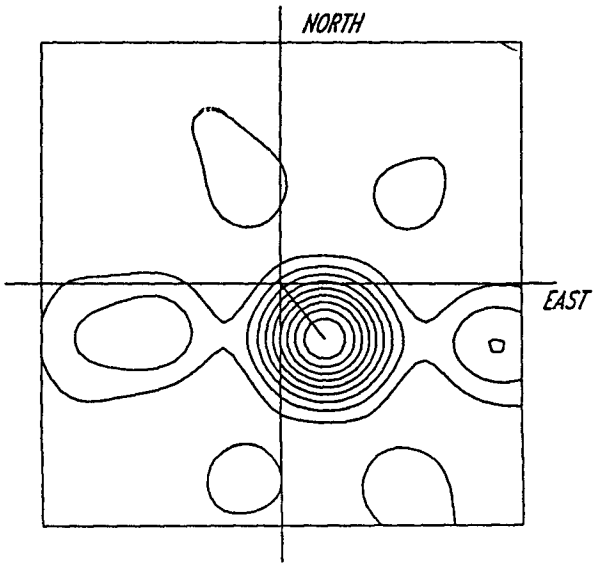

event 3
Rg

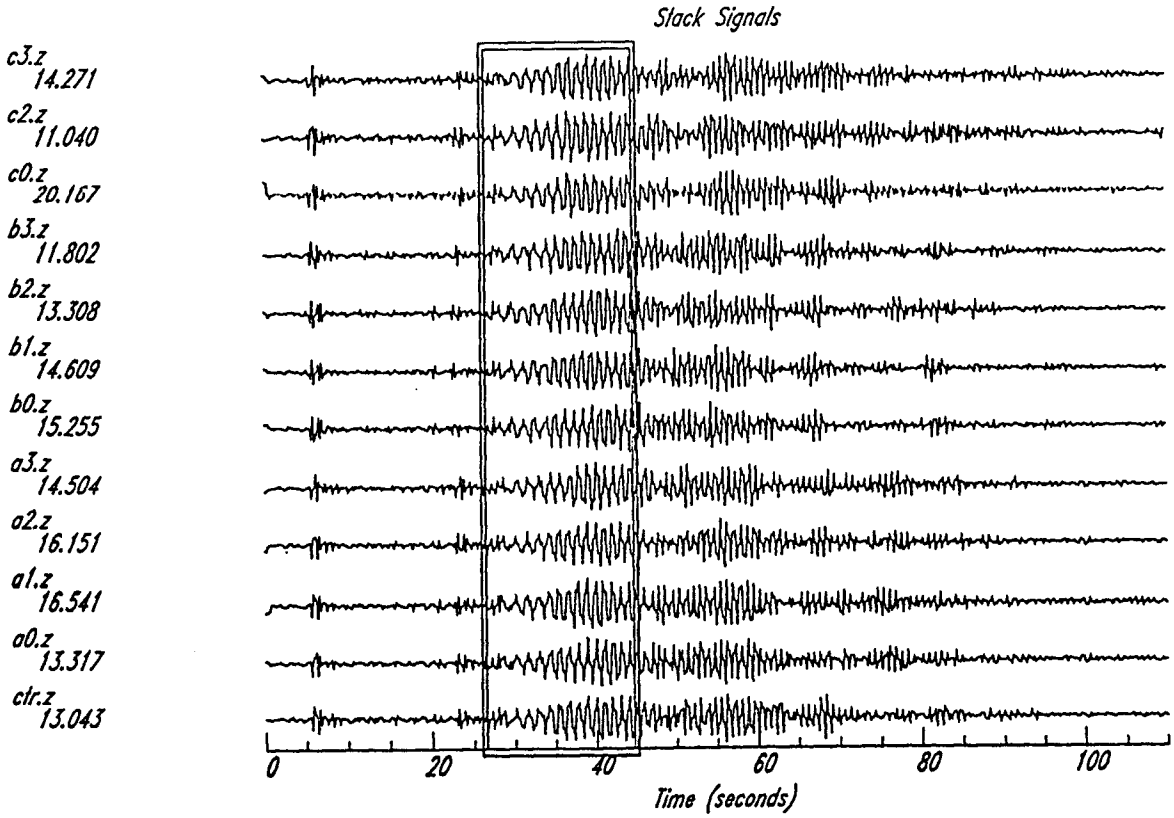

NBFK - single window

Estimated bearing: 136.58

Estimated velocity: 2.5172

Analysis frequency: 0.9384

Max. horiz. wavenumber: 1.0000

Scaling type: LINEAR

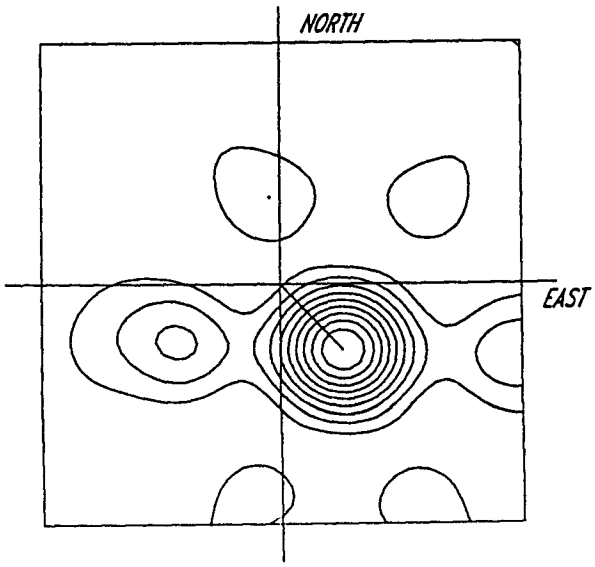

event 4
P-wave

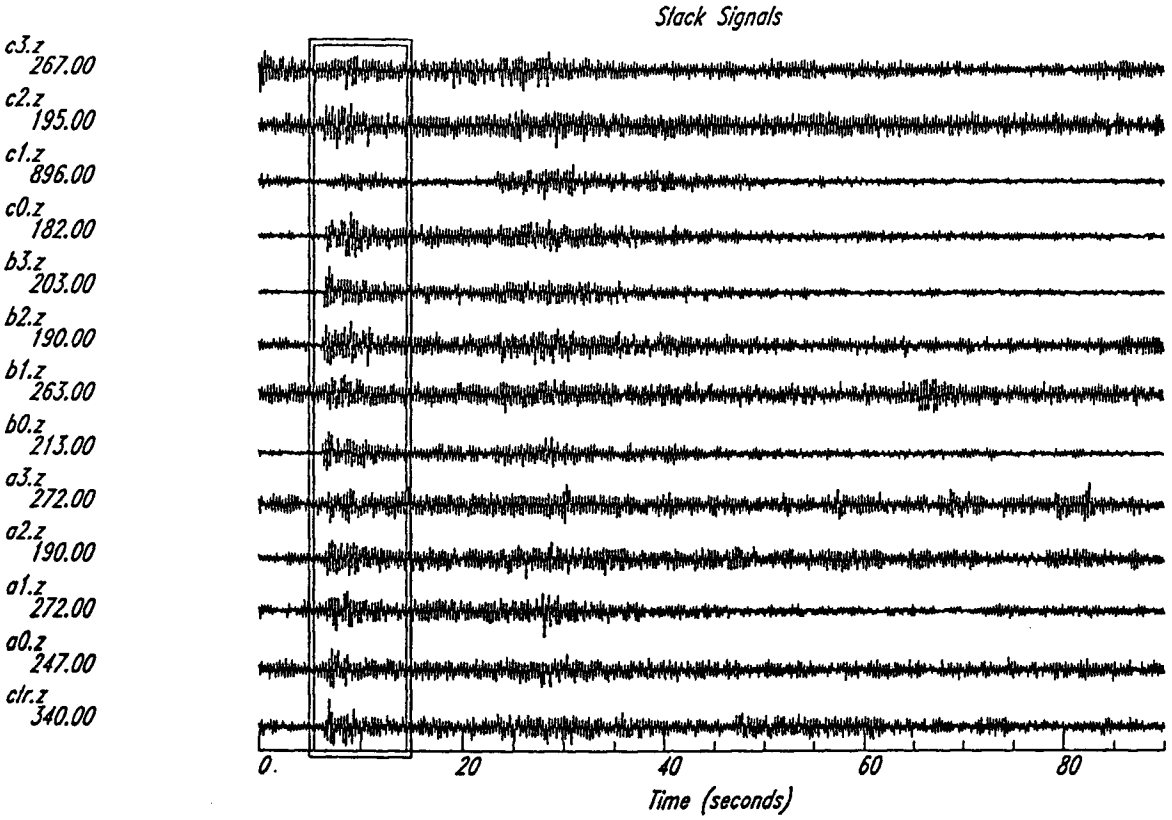

NBFK - single window

Estimated bearing: 157.10

Estimated velocity: 7.2739

Analysis frequency: 6.621

Max. horiz. wavenumber: 1.0000

Scaling type: LINEAR

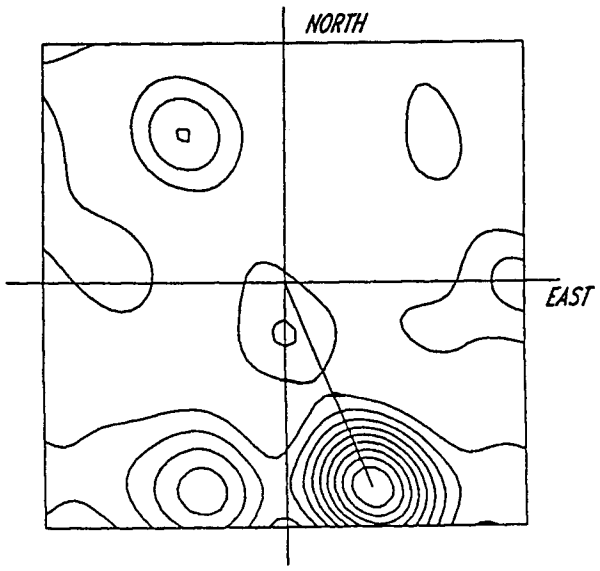

event 4
Rg

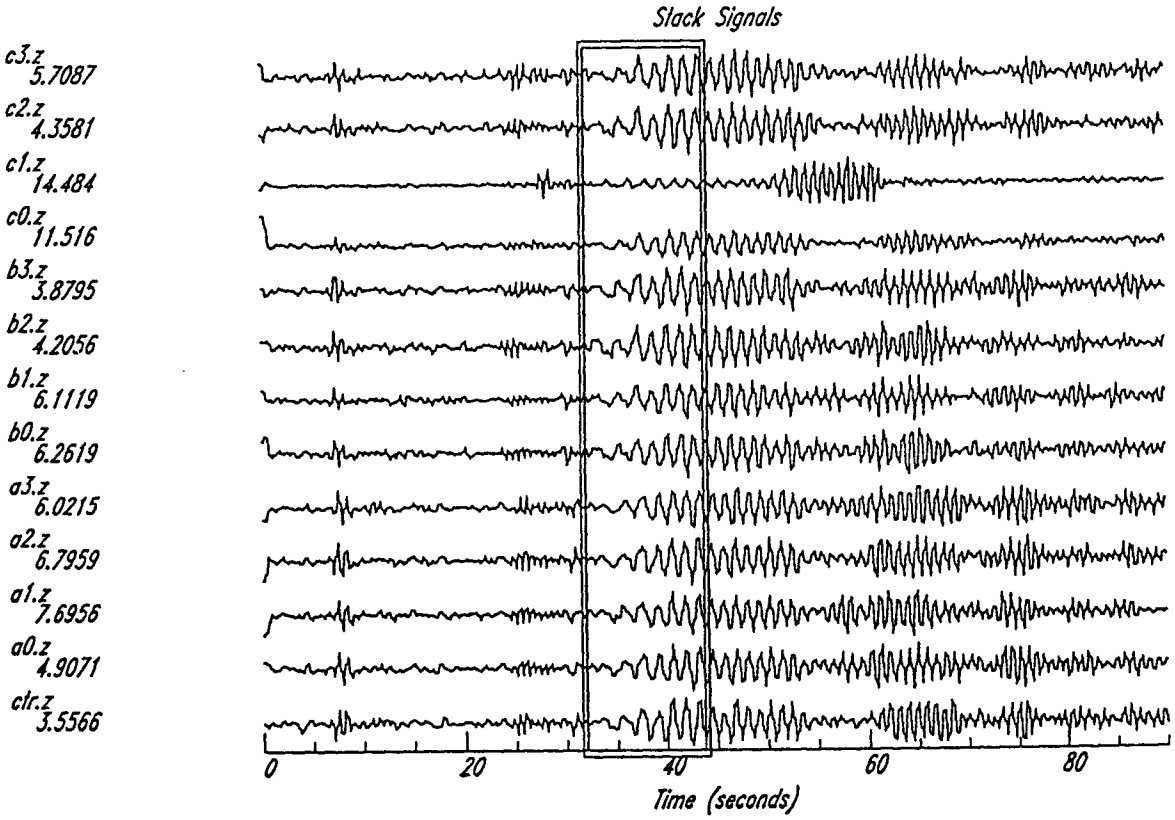

NBFK – single window

Estimated bearing: 151.11

Estimated velocity: 2.9117

Analysis frequency: 0.6932

Max. horiz. wavenumber: 1.0000

Scaling type: LINEAR

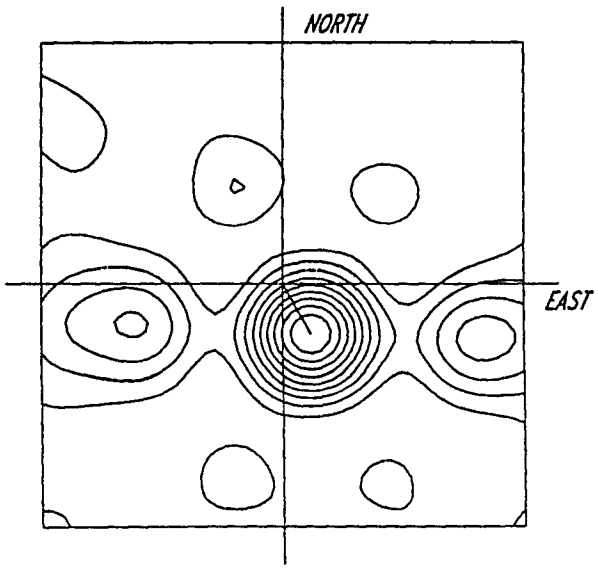

event 5
P-wave

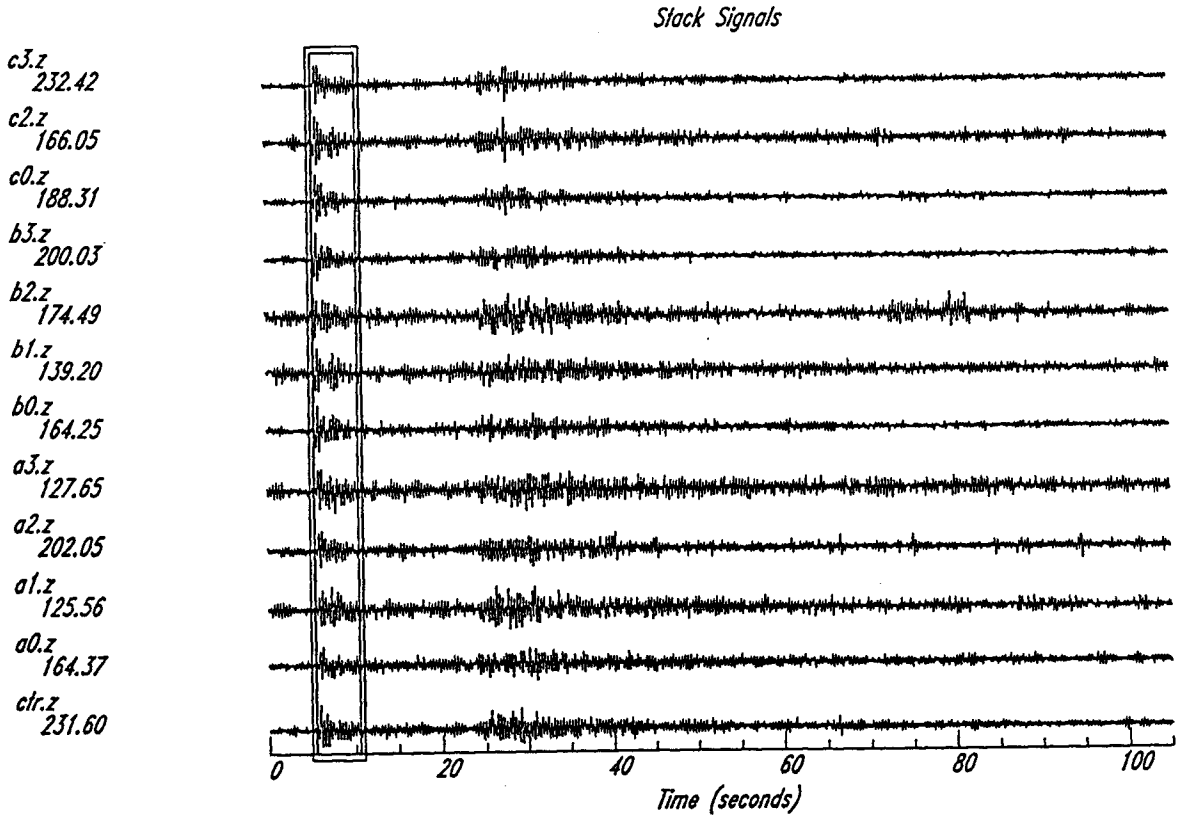

NBFK - single window

Estimated bearing: 170.91

Estimated velocity: 6.9101

Analysis frequency: 6.998

Max. horiz. wavenumber: 1.0000

Scaling type: LINEAR

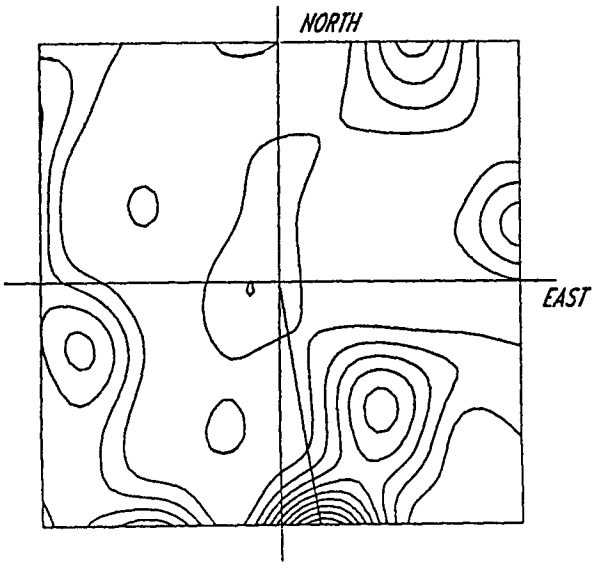

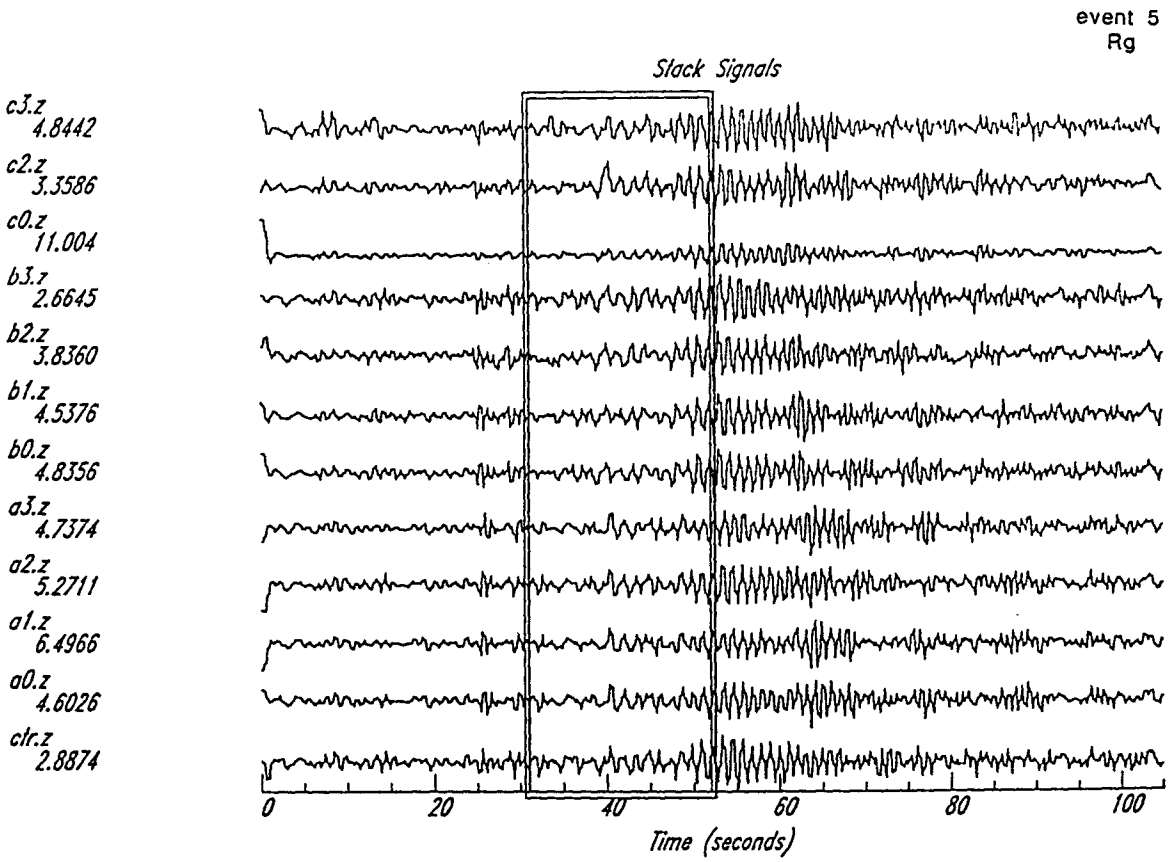

NDFK - single window

Estimated bearing: 171.33

Estimated velocity: 2.8403

Analysis frequency: 0.7921

Max. horiz. wavenumber: 1.0000

Scaling type: LINEAR